The Dissertation Committee for Sangjo Shim Certifies that this is the approved version of the following dissertation:

Antibody-Free Isolation of Circulating Tumor Cells by Dielectrophoretic Field-Flow Fractionation

Committee:

Peter Gascoyne, Supervisor

Mia Markey

Li Shi

James Bankson

James Reuben

Antibody-Free Isolation of Circulating Tumor Cells by Dielectrophoretic Field-Flow Fractionation

by

Sangjo Shim,B.S.;B.E.;M.S

Dissertation

Presented to the Faculty of the GraduateSchool of
The University of Texas at Austin
in Partial Fulfillment
of the Requirements
for the Degree of

Doctor of Philosophy

The University of Texas at Austin
August 2013

Dedication

This dissertation is dedicated to my dear wife Sunghee for her loving care and constant reassurance through both the happy and the challenging phases of this work, to my parents for their support, to my sister for her encouragement, and to my son whom I hope one day will think his father did a good job!

Acknowledgements

I greatly appreciate the many discussions with, and the valued advice of, Professor Peter Gascoyne. I am very grateful for the wonderful administrative and technical support from JamilehNoshari. Most of the designs and fabrication efforts in this study were aided by Tom Anderson and I am thankful for his help, practicality and wisdom in realizing assembly strategies that actually work. I am especially grateful to Katherine Stemke-Hale who introduced me to the NCI-60 panel of cell lines and arranged for these lines to be made available for my studies.

I am grateful to Ann T. James and Debra L Andrews, phlebotomists in the Department of Investigational Cancer Therapeutics, for her help in coordinating and collecting the clinical specimens. Parts of this work were supported by grant RP100934 from the Cancer Prevention and Research Institute of Texas (CPRIT), by the Kleberg Center for Molecular Markers, and by a sponsored research agreement from ApoCell, Inc. KSH is also supported by a Stand Up to Cancer Dream Team Translational Research Grant, a Program of the Entertainment Industry Foundation (SU2C-AACR-DT0209).

Antibody-Free Isolation of Circulating Tumor Cells by Dielectrophoretic Field-Flow Fractionation

Sangjo Shim, Ph.D.
The University of Texas at Austin, 2013

Supervisor: Peter R.C. Gascoyne

This work focuses on the integration of microfluidics and dielectrophoresis(DEP) with the principles of field flow fractionation (FFF) to create a continuous-flow isolator for rare and viable circulating tumor cells (CTCs) from peripheral blood mononuclear cells (PBMNs) drawn from cancer patients. The method exploits differences in the plasma membrane capacitances of tumor and blood cells, which correspond to differences in the membrane surface areas of these cell types. DEP-FFF was first adapted to measure cell membrane capacitance, cell density and deformability profiles of cell populations. These properties of the NCI-60 panel of cancer cell types, which represents the wide functional diversity of cancers from 9 organs and leukemia, were compared with the normal cell subpopulations of peripheral blood. In every case, the NCI-60 cells exhibited membrane capacitance characteristics that were distinct from blood and, as a result, they could be isolated from blood by DEP. The heightened cancer cell membrane capacitances correlated strongly with membrane-rich morphological characteristics at their growth sites, including cell flattening, dendritic projections, and surface wrinkling. Following harvest from culture and maintenance in suspension, cancer cells were found to shed cytoplasm and membrane area over time and the suspended cell populations developed considerable morphological diversity. The shedding changed the cancer cell DEP properties but they could still be isolated from blood cells. A similar shedding process in the peripheral blood could account for the surprisingly wide morphological diversity seen among circulating cells isolated from clinical specimens. A continuous flow DEP-FFF method was devised to exploit these findings by allowing CTCs to be isolated from the nucleated cells of 10 mL clinical blood specimens in 40 minutes, an extremely high throughput rate for a microfluidic-based method. Cultured cancer cells could be isolated at 70-80% efficiency using this approach and the isolation of CTCs from clinical specimens was demonstrated. The results showed that the continuous DEP-FFF method delivers unmodified, viable CTCs for analysis, is perhaps universally applicable to isolation of CTCs from different cancer types and is independent of surface antigens - making it suitable for cells lacking the epithelial markers used in currently accepted CTC isolation methods.

Table of Contents

List of Tables

List of Figures

CHAPTER 1 INTRODUCTION

1.1 OVERVIEW

Metastatic disease is an often fatal complication that results when cancer spreads from a primary tumor and forms one or more new tumors at distant sites in the body. The disease is able to migrate in this way when cancer cells become dissociated from the primary tumor and are transported through the cardiovascular system as circulating tumor cells (CTCs). If these cells are able to infiltrate surrounding tissues and proliferate, new tumors are formed. The consequent disease is termed metastasis of cancer or secondary cancer[1, 2]. The presence of CTCs in the peripheral blood of cancer patients has been shown to be a prognostic indicator for metastatic disease. Furthermore, the molecular profile of the CTCs is expected to be indicative of their invasiveness and capacity for uncontrolled proliferation at distal sites in the body[3, 4]. Therefore, the isolation, counting and characterization of CTCs are considered to be important capabilities for understanding metastatic disease from a research perspective and in prognosis and diagnosis in the clinic[2, 3]. However, currently it is a huge technological challenge to isolate CTCs because their concentration in the peripheral blood is very small. For example, even one CTC per milliliter of peripheral blood is considered to be indicative of a worsening outcome for breast and prostate cancer patients[2, 3].

A lot of research effort has been applied to developing novel technologies for improved CTC isolation. However, to date, only the CellSearch method, which is based on immunomagnetic isolation of EpCAM+ cells in the blood has received FDA approval for clinical tests for prognosis[5]. This test is far from ideal because it is only applicable to epithelially-derived tumors that express EpCAM and it cannot collect CTCs from tumors that fail to express EpCAM[6, 7]. These include EpCAM negative or hybrid cells that are undergoing the epithelial to mesenchymal transition and are considered to be the most likely cells to form metastases. Furthermore, the CellSearch method requires cells to be fixed, eliminating the possibilities of characterizing the isolated cells by gene expression profiling and conducting growth assays that would permit drug response testing for targeted therapies[5], for example. For these reasons, there is great interest in the development of technologies that can isolate unaltered, viable CTCs without depending on cell surface markers that may be expressed erratically[8].

Attempts to develop CTC isolation capabilities with these characteristics have included processing blood with microfabricated pore filter arrays and microfluidic hydrodynamic capture[9, 10]. The filtering approach assumes that CTCs are significantly larger than all of the other cell types present in peripheral blood, an assumption that a study of the CTCs collected by the CellSearch method shows to be incorrect. Furthermore, although larger CTCs can be captured on microfabricated filters without the need to use antibodies to identify them, these cells are damaged and lose viability because of the high fluid shear conditions present during filtering[9, 10].

Microfluidic hydrodynamic capture depends on differences between the inertial properties of CTCs and blood cell subpopulations. This method is still under development and it is not clear how efficient it will prove to be or whether the isolated CTCs will be viable.

Another method for isolating CTCs from blood without using antibodies is based on dielectrophoresis (DEP)[11]. It was shown many years ago that it was possible to trap cancer cells on a microelectrode array by applying attractive dielectric forces while blood cells were washed away[12, 13]. The cancer cells needed no labeling, remained viable during DEP trapping, and could be released afterwards by turning off the electrical signal[12, 14, 15]. A major challenge with that approach has been with scaling. The initial experiments on a microchip used only 2000 peripheral blood mononuclear cells (PBMNs) containing a few cancer cells[16]. That corresponds to the number of cells in only 0.5 μL of peripheral blood. If CTCs, which are clinically significant in concentrations as low as one per milliliter, are to be collected, counted and analyzed, the minimum clinical specimen size for processing needs to be around 10 milliliters, showing that the original DEP method needed to be scaled up by a factor of 20,000 to have clinical relevance. Subsequently, DEP was combined with the technique of field-flow fractionation (FFF) to create a chromatographic method called DEP-FFF[17, 18]. This method, which was shown to successfully isolate unlabeled, viable tumor cells from PBMNs even more efficiently than DEP trapping, allowed up to 2 million PBMNs to be analyzed in each batch. Notwithstanding this success, the throughput was still 20-fold too low for clinical applications[19].

My hypothesis was that the DEP-FFF principles could be adapted to a continuous-flow regime that would allow 10 mL clinical specimens to be processed in less than 60 minutes and thereby provide a universal and reliable detection method for CTCs that was independent of cancer type and surface markers.

This dissertation describes the work I undertook to prove this hypothesis, including obtaining a better understanding of the biological basis for DEP isolation of CTCs[20], demonstrating the broad applicability of DEP isolation methods to CTCs from almost any cancer (Included in the NCI 60 panel are 38 epithelial and 22 non-epithelial lines derived primarily from patients with advanced and/or metastatic disease)[21], and designing[22], building and testing a continuous flow DEP-FFF isolation system that had the required throughput to process clinical specimens[23]. In the remainder of this chapter, the principles of DEP and FFF as applied to manipulating mammalian cells will be reviewed[19, 24, 25]. In Chapter 2 these principles will be applied to the problem of profiling the biophysical properties of cells that pertain to cell separation by DEP-FFF and characterizing the differences between cancer cells and blood cells[24]. Chapters 3 and 4 detail my investigations into the biological basis for the differences observed between blood and cancer cells and shows that cell morphology and plasma membrane area at the growth site of the cells are the key defining parameters for these differences[20, 24]. In the course of these studies on tumor cells, I observed that they tended to undergo morphological remodeling when they were released from their growth site and were maintained in suspension for an extended time. The suspended cells shed cytoplasm and membrane in the form of giant vesicles in a process that left them smaller, but still viable, and that I showed was not related to apoptosis[26], anoikis or necrosis[25]. This cell structural remodeling process may account for the surprisingly wide range of morphologies that have been observed in CTCs isolated from clinical specimens. Significantly, even though this shedding process modified the cell dielectric properties, it did not compromise the ability of DEP to discriminate between blood and cancer cells[24].

An important requirement for any new method for isolating CTCs is that it should be applicable to all types of cancer. In Chapter 3, I applied the DEP-FFF method to characterize the NCI panel of 60 different cancer cell lines, which represents the wide range of tumor functional variants in nine different organs and leukemia[21, 22]. My data showed that all types of cancer had characteristics that allowed for their isolation from normal peripheral blood under appropriate DEP-FFF settings. Cells from solid tumors had large dielectric differences compared to the normal blood cell subpopulations suggesting that CTCs from these tumors can be isolated efficiently from blood. The leukemia lines from the NCI-60 panel, however, had much smaller differences compared to normal blood cell subpopulations, showing that leukemia cells could be concentrated, but not efficiently isolated, from normal blood. Nevertheless, from a clinical perspective, the inability to isolate pure leukemia cells from peripheral blood is not a problem.

Having understood the parameter requirements for efficiently isolating this wide range of cancer cell types from solid tumors in the NCI-60 panel, I designed and built a continuous-flow DEP-FFF isolator[23]. Chapter 5 describes the technical principles involved and shows my final working design, which incorporated a novel method of reducing the ionic conductivity of the specimen while simultaneously maintaining its osmolarity through a membraneless dialysis method[23]. This allowed the cells in the clinical specimens to be maintained under physiological conditions, rather than DEP buffer conditions, until they were processed, insuring that their properties did not alter during the 40 minutes required to process cells from a 10 mL blood specimen. After membraneless dialysis, the CTCs and blood cells were spatially separated by dielectrophoresis and the CTCs were skimmed off. Using this design, I demonstrate the isolation of tumor cell spiked into normal peripheral blood with an efficiency of 70-80% and its successful application to clinical specimens[23]. Finally, Chapter 6 draws conclusions from my findings and suggests future improvements and study directions.

1.2 DIELECTROPHORESIS

DEP is an electrokinetic phenomenon that has become increasingly popular for biological applications in microfluidic and lab-on-chip devices since its introduction by Pohl[11, 27]. Gascoyne's group was instrumental in applying this method for characterizing and manipulating cancer cells[19, 25]. His was also the first group to demonstrate and exploit negative (repulsive) DEP[19, 25, 28-30], to develop automated imaging systems to measure cellular DEP effects and cell dielectric properties, to analyze the accuracy of dielectric parameters derived from cell electrokinetic responses, and to develop a generalized dielectrophoresis (gDEP) theory that unified the theoretical treatments of DEP and traveling wave DEP (twDEP)[31]. In the study of cancer, his group was the first to employ AC electrokinetic effects for studying membrane changes accompanying differentiation of erythroleukemia, kidney and leukemia cells [32], for studying breast cancer and colon cancer; and for correlating changes in membrane dielectric properties with membrane structure, morphology and conductivity and with [13, 29, 33-35]. As a result, it was possible to separate human leukemic cells and human metastatic breast cancer cells from normal human leukocytes through DEP migration[12, 36, 37] and DEP retention[12, 29, 38, 39].

DEP occurs when an inhomogeneous electric field induces dielectric charge polarization in a particle and a net force on that polarization arises because the local fields acting on the equal and opposite charges on either side of the particle are different. The net force, which depends on the dielectric polarizability of the particle in its suspending medium, is called the dielectrophoretic force and it can be used to move particles in accordance with their dielectric properties even though the net charge on the particle is unaltered and may be zero. Dielectric polarization occurs in both DC and AC electric fields, however, DEP manipulations of cells are usually carried out using AC fields so that the frequency-dependent dielectric properties of cells and their suspending medium can be exploited[18, 19, 24, 25].

In a stationary inhomogeneous AC electric field $\vec{E}(f)$ [40, 41], the DEP force acting on a particle can be written as

$$F_{DEP} = 2\pi\varepsilon_s\ R^3\ \mathrm{Re}\left(f_{CM}^*(f)\right)\nabla E_{RMS}{}^2\ , \tag{1.1}$$

where $$f_{CM}^*\ (f) = \frac{\varepsilon_p^*(f) - \varepsilon_s^*(f)}{\varepsilon_p^*(f) + 2\varepsilon_s^*(f)} \tag{1.2}$$

is the Clausius-Mossotti factor that embodies the complex frequency-dependent dielectric properties $\varepsilon_p^*(f) = \varepsilon_p - i\sigma_p/(2\pi f)$ and $\varepsilon_s^*(f) = \varepsilon_s - i\sigma_s/(2\pi f)$ of the particle and its suspending medium, respectively[11, 40]. f is the frequency and E_{RMS} the RMS value of the applied electric field and $i=\sqrt{-1}$.

The DEP force pushes particles towards strong or weak field regions, depending upon whether $\mathrm{Re}(f_{CM})$ is positive or negative and thereby allows cells to be attracted or repelled from electrode edges. The electric field inhomogeneity is embodied in the $\nabla E_{RMS}{}^2$ term, which reflects the geometry and asymmetry of the electrode configuration and the applied AC voltage.

Note that there is a special value of the frequency f_o for which

$$f_{CM} = \mathrm{Re}\left(f_{CM}^{*}(f_o)\right) = \mathrm{Re}\left(\frac{\varepsilon_p^{*}(f_o) - \varepsilon_s^{*}(f_o)}{\varepsilon_p^{*}(f_o) + 2\varepsilon_s^{*}(f_o)}\right) = 0\,, \tag{1.3}$$

where the DEP force goes to zero and cells in the inhomogeneous electric field will experience no DEP movement. At applied AC electric field frequencies below f_o , the DEP force will be negative (repulsive from high electric field regions near electrode edges). At applied frequencies above f_o, the DEP force will be positive (attractive towards high field regions near electrode edges). Substituting for the dielectric and conductive components of the complex permittivities and rearranging expression (3) shows that this zero force condition occurs when

$$f_o = \frac{1}{2\pi}\left\{\frac{(\sigma_s - \sigma_p)(\sigma_p + 2\sigma_s)}{(\varepsilon_p - \varepsilon_s)(\varepsilon_p + 2\varepsilon_s)}\right\}^{1/2}. \tag{1.4}$$

Because the direction of the DEP force changes sign at f_o, this frequency is called *the DEP crossover frequency[40].*

1.3 CELL DIELECTRIC PROPERTIES

The Claussius-Mossotti factor depends on the shape and composition of the particle. The most effective dielectric representation for mammalian cells has been shown to be the dielectric shell model[41, 42], which approximates the cell as a set of concentric, homogeneous spherical shells, with the number of shells increasing as the structural complexity of the cell increases. The number of interfacial dielectric dispersions reflects the number of interfaces between shells.

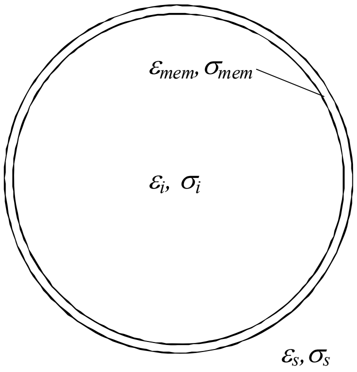

Figure 1.1 Single shell model

The dielectric properties of most mammalian cells are approximated very closely by the single shell model (shown above), where an inner sphere of radius r (representing the cytoplasm) is surrounded by a thin shell of thickness d (representing the membrane). If the membrane has a conductivity that is much lower than the surrounding medium and the cytoplasm (consistent with a lipid bilayer membrane having an intact barrier function), charges build up at the membrane-medium interface when the cell is placed in an electric field. The effective permittivity of the cell according to the single shell model may be written [41, 42]as

$$\varepsilon_p^* = \varepsilon_{mem}^* \frac{\left(\frac{R}{r}\right)^3 + 2\left(\frac{\varepsilon_i^* - \varepsilon_{mem}^*}{\varepsilon_i^* + 2\varepsilon_{mem}^*}\right)}{\left(\frac{R}{r}\right)^3 - \left(\frac{\varepsilon_i^* - \varepsilon_{mem}^*}{\varepsilon_i^* + 2\varepsilon_{mem}^*}\right)} \tag{1.5}$$

where $R = r+t$ and the subscripts i and mem refer to the cytoplasmic and membrane compartments, respectively, as shown in the diagram above. Because the cell membrane is very thin we can also write $R>>t$. Again, each complex permittivity term embodies both the real permittivity and real conductivity of each component, $\varepsilon_{mem}^*(f) = \varepsilon_{mem} - i\sigma_{mem}/(2\pi f)$ and $\varepsilon_i^*(f) = \varepsilon_i - i\sigma_i/(2\pi f)$.

For frequencies between approximately 10 kHz and 1 MHz and an internal conductivity >> suspending medium conductivity we can make the approximation that [41, 43]

$$\left(\frac{\varepsilon_i^* - \varepsilon_{mem}^*}{\varepsilon_i^* + 2\varepsilon_{mem}^*}\right) \sim 1 \quad \text{so that} \tag{1.6}$$

$$\varepsilon_p^* \sim \varepsilon_{mem}^* \left\{\frac{\left(\frac{1}{1-t/R}\right)^3 + 2}{\left(\frac{1}{1-t/R}\right)^3 - 1}\right\} \sim \quad \varepsilon_{mem}^*\left(\frac{R}{t}\right). \tag{1.7}$$

From this expression, we can express the specific capacitance of the plasma membrane[41, 43] as

$$C_{mem} = \mathrm{Re}\left(\varepsilon^{*}_{mem} / t\right) \text{ so that}$$

$$C_{mem} = \frac{\varepsilon_p}{R} \text{ F.m}^{-2} \tag{1.8}$$

and the specific conductance of the plasma membrane[41, 43] as

$$G_{mem} = \mathrm{Im}\left(\varepsilon^{*}_{mem} / t\right) \text{ so that}$$

$$G_{mem} = \frac{\sigma_p}{R} \text{ S.m}^{-2}. \tag{1.9}$$

This allows us to rewrite expression (1-4) for the cell crossover frequency in terms of the membrane specific capacitance and conductance as

$$f_o = \frac{1}{2\pi}\left\{\frac{\left(\sigma_s - R.G_{mem}\right)\left(2\sigma_s + R.G_{mem}\right)}{\left(R.C_{mem} - \varepsilon_s\right)\left(R.C_{mem} + 2\varepsilon_s\right)}\right\}^{1/2}. \tag{1.10}$$

The membrane conductivity for a viable cell having an intact membrane barrier function is exceedingly low so that $R.G_{mem} << \sigma_s$. Also, membrane capacitance is found to be large so that $R.C_{mem} >> \varepsilon_s$. Therefore, the crossover frequency for intact mammalian cells can be approximated as[41]

$$f_o = \frac{\sigma_s}{2^{\frac{1}{2}}\pi \, R.C_{mem}}, \tag{1.11}$$

which depends on the suspending medium conductivity σ_s. A cell characteristic that is independent of the suspending medium properties that embodies the same concept is

$$\Theta_0 = \frac{f_0}{\sigma_s}, \tag{1.12}$$

the cell crossover frequency per unit conductivity of the suspending medium. The specific membrane capacitance (the membrane capacitance per unit area) C_{mem} [41]and the cell total membrane capacitance C_{tot} may then be written, respectively, as

$$C_{mem} = \frac{1}{2^{0.5}\pi R \Theta_0} \quad \text{and} \tag{1.13}$$

$$C_{tot} = \frac{2^{3/2} R}{\Theta_0}. \tag{1.14}$$

For convenience, the real part of the Claussius-Mossotti factor can also be rewritten in terms of the applied AC field frequency f and the cell crossover frequency f_o [44, 45]as

$$f_{CM} = \frac{f^2 - f_o^2}{f^2 - 2f_o^2} \tag{1.15}$$

Expression (1.11) shows that there is a direct relationship between the specific membrane capacitance and DEP crossover frequency and measurements of DEP crossover frequencies may be used to infer cell membrane capacitance.

Throughout this dissertation, the DEP crossover frequency will be referred to many times because it is a useful descriptor of how particular cell types will behave when subjected to DEP manipulation. Considerable effort is focused in Chapter 2 on developing a method to derive distributions of DEP crossover frequencies for cell populations. The relationship between DEP crossover frequency and the more biologically-relevant cell plasma membrane structure forms the focus of Chapter 4. These concepts lead to the subsequent discussions of cancer cell properties and the design and implementation of CTC isolators in Chapter 5.

TheDEP principles shown above have been used in many labs to understand cell properties. Different cell types exhibit different DEP properties largely on the basis of dissimilarities in crossover frequencies and numerous researchers have demonstrated DEP-based isolation of biological cells: stem cells[46], platelets[47], white blood cells[48], pancreatic b-cells[49], osteoblasts[50], prostate tumor initiating cells[51], oral cancer cells[52, 53], melanoma[54], colorectal cancer cells[55] and circulating tumor cells(CTCs) from blood[12, 15, 29, 56, 57]. In many cases, DEP trapping is used as the basis for cell separation. In this case, the AC electric field is set to a frequency that is above the crossover frequency of a target cell type yet below that of unwanted cells. Although Gascoyne's lab[29, 58] was the first to advocate this approach, its resolution proved to be limited because the dielectric differences between the cells need to be large if one cell type is to be reliably trapped by positive DEP while the others are reliably excluded. More often, distributions of crossover frequencies for the different cell types result in there being a significant subpopulation of target cells that are not reliably trapped, resulting in loss of target cells. For this reason, Gascoyne's lab and Pethig's lab independently conceived of the method of dielectrophoretic field-flow fractionation (DEP-FFF), though the bulk of lab-on-chip work described in the literature today still uses DEP trapping and lacks the finer discrimination needed for clinical applications[19, 25, 59, 60].

1.4 DEP-FFF SEPARATION

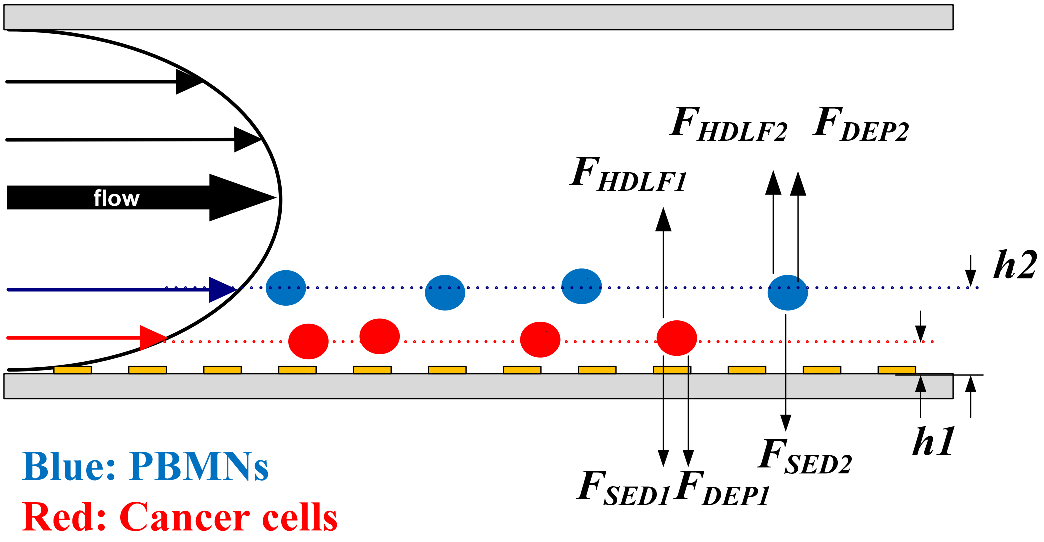

Figure 1.2 DEP-FFF showing cancer cells attracted and PBMNs levitated

To allow for higher discrimination in cell isolation applications, Gascoyne's laboratory first introduced a fractionation method termed DEP-FFF[17, 18, 25, 61-63]. This method uses a large array of thin, parallel interdigitated microelectrodes on the floor of the separation device. AC electric fields are applied to these microelectrodes and fringing fields are created in the space above them in the separation chamber. The resultant periodic, inhomogeneous electric field pattern is used to create DEP forces on cells in the chamber. Depending on the relationship between the applied electric field frequency and the DEP crossover frequency, the DEP force on a particular cell type may attract it towards the microelectrode array on the chamber floor or levitate the cell into the chamber away from the floor. The strength and inhomogeneity of the electrical field distribution decreases with increasing height above the electrode plane and the DEP force on cells falls exponentially with height[19, 25] If a frequency for which cells experience negative DEP is applied to the electrode array, cells will be levitated to a height at which the repulsive DEP force balances the sedimentation force. By equating the DEP force and sedimentation force equations and rearranging, the cell equilibrium height is found to be[62]

$$h = \frac{d}{2\pi} \ln \left\{ \frac{3\varepsilon_s V^2 A P(f)}{2(\rho_p - \rho_s) g} \mathrm{Re}(f_{CM}) \right\} \tag{1.16}$$

where V is the electrical potential applied to the electrode array, A is a geometrical term, $P(f)$ is the proportion of the applied field unscreened by electrode polarization, and $(\rho_p - \rho_s)g$ is the sedimentation force per unit volume of the cell[62]. Note that because DEP and sedimentation are both body forces, the cell volume cancels and the equilibrium height is independent of cell size. Cells having differences in density and/or dielectric properties will therefore be levitated to characteristic equilibrium heights as illustrated in Figure 1.2.

To exploit differences in equilibrium levitation height to bring about cell fractionation, fluid flow is initiated in the channel. Fluid flows through the channel in a parabolic profile ranging from zero velocity at the chamber floor and ceiling to maximum velocity in the middle (chamber half height). The velocity at height h of this so-called Poiseiulle flow profile is given by[18, 25]

$$v_p(h) = 6\langle v\rangle \frac{h}{H}\left(1-\frac{h}{H}\right), \tag{1.17}$$

where H is the chamber height and $<v>$ is the mean fluid velocity. The cells will be carried through the chamber at the flow velocity corresponding to their equilibrium levitation height[18, 25]. Mixed cell types starting together as a batch at one end of a long chamber will therefore be carried through at different velocities and will be separated according to their dielectric and density properties, which dictated their levitation heights in the DEP field. The family of techniques that exploits hydrodynamic flow profiles for separation in this manner is termed field-flow fractionation (FFF); hence Gascoyne termed this dielectric method DEP-FFF[18, 25].

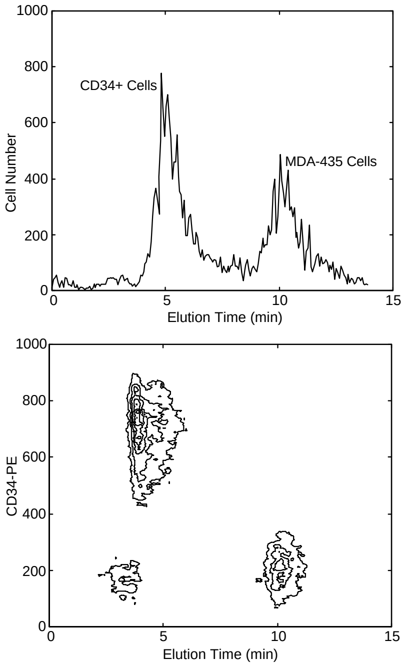

Figure 1.3 Separation of breast cancer cells from CD34+ stem cells by DEP-FFF. Cells emerging from DEP-FFF were passed directly through a flow cytometry for counting and fluorescence typing[63].

As an example of DEP-FFF in action, Figure 1.3 shows the isolation of CD34+ hemopoietic stem cells from MDA-MB-43 human breast cancer cells[63]. In this example, the CD34+ cells had a much higher crossover frequency (100 kHz) than the tumor cells (5 kHz) at the suspension conductivity employed. At the applied DEP frequency of 30 kHz, the CD34+ and cancer cells had Claussius-Mossotti factors of -0.439 and -0.097 , respectively. As a result, the CD34+ cells were levitated higher, and therefore into a faster flowing region of the flow profile, than the cancer cells and eluted much quicker.

Because the velocity gradient of the fluid flow profile (the shear rate) in Poisseiulle flow is largest close to the chamber floor, the discriminating power of DEP-FFF is higher when the cells are levitated less[25]. This occurs in the frequency range where the cell DEP force approaches zero[25] close to the crossover frequency. Small differences in cell dielectric properties or density then result in significantly different transport velocities by the fluid flow. However in this high shear flow region near the chamber floor, an additional force called hydrodynamic lift (HDLF) becomes significant and this limits how sensitively the levitation height and transport velocity depend on the DEP force. In general, the transit time for cells through a DEP-FFF chamber therefore depends on the balance of three, rather than two, force components, namely DEP, sedimentation and HDLF. The hydrodynamic lift force on a body depends strongly on how deformable the body is in the shear flow, therefore HDLF offers the opportunity to probe cell deformability in a contactless manner. Because the HDLF is small at low fluid flow rates and in low shear regions well away from the chamber floor or ceiling, and large at high flow rates and in high shear regions near the chamber floor, it is possible to alter the relative strengths of the DEP and HDLF components by adjusting the experimental conditions[25]. I will exploit this property in Chapter 2 in applying the DEP-FFF method to measure cell properties.

Note that most parameters used in this dissertation are listed in Table 1.

Table 1.1 Parameters used in Equations

* parameter value deduced from analysis of dFFF elution measurements
† The values given pertain to the eluate used in this study comprising an aqueous solution of 9.5% sucrose adjusted to a conductivity of 30 mS.m^{-1} (see Chapter 2)

Symbol	Parameter	Value	Units
F_{SED}	Sedimentation force on cell in eluate	*	N
F_{DEP}	Dielectrophoretic force on cell in eluate	*	N
F_{HDL}	Hydrodynamic lift force on cell in eluate	*	N
ρ_p	Cell Density	*	kg.m^{-3}
g	Acceleration due to gravity	9.81	m.s^{-2}
h	Equilibrium height of cell above DEP array	*	m
f_{CM}	Claussius-Mossotti factor	*	—
f_0	Cell crossover frequency	*	Hz
Θ_0	Cell crossover frequency per unit eluate conductivity $= f_0 / \sigma_s$	*	Hz.S^{-1}
$\Phi(\nu)$	Cell deformability factor	*	—
ε_{mem}	Dielectric permittivity of cell membrane	*	F.m^{-1}
C_{mem}	Cell specific membrane capacitance	*	F.m^{-2}
C_{tot}	Cell total membranecapacitance	*	F
σ_{mem}	Cell membrane conductivity	*	S.m^{-1}
G_{mem}	Cell specific membrane conductance	*	S.m^{-2}
ε_i	Dielectric permittivity of cytoplasm	*	F.m^{-1}
σ_i	Conductivity of cytoplasm	*	S.m^{-1}
R	Cell radius	measured	m
t	Thickness of cell plasma membrane	~4.5	nm

Table 1.1 (continued)

V	Applied DEP AC voltage	varies	Volts pk-pk
f	Applied DEP AC frequency	15 to 300	kHz
E_{RMS}	Root mean square AC field	varies	V.m^{-1}
ρ_s	Density of eluate	1.036 x 10^{3} †	kg.m^{-3}
σ_s	Conductivity of eluate	30 †	mS.m^{-1}
ε_s	Dielectric permittivity of eluate	6.90 x 10^{-10} †	F.m^{-1}
η	Kinematic viscosity of eluate	1.266 x 10^{-7} †	m^{2}.s^{-1}
B	Eluate flow rate	(3 – 15) x 10^{-8}	m^{3}.s^{-1}
s	Microelectrode width and spacing	5.0 x 10^{-5}	m
d	Microelectrode periodicity $= 4s$	2.0 x 10^{-4}	m
H	DEP chamber height	3.62 x 10^{-4}	m
W	DEP chamber width	2.4 x 10^{-2}	m
$<v>$	Mean fluid velocity in DEP-FFF chamber	6.9	mm.s^{-1}
$v_p(h)$	Cell velocity in DEP-FFF chamber at height *h*	Depends on	m.s^{-1}
L	DEP chamber Length	0.30	m
$P(f)$	Effective proportion of DEP voltage	0.7	—
$a = \frac{4}{3}\pi g$	$\frac{4}{3}\pi$ x acceleration due to gravity	41.08	m.s^{-2}
$b = 352\pi\varepsilon_s d^{-3}$	Constant for this study	9.54 x 10^{4}	F. m^{-4}
$c = \frac{6\eta}{H^2 W}$	Constant for this study	241.5	m^{-1}.s^{-1}
L_{mix}	Mixing length	Varies	m
D	Diffusion coefficient	2.5 x 10^{-9}	m^{2}.s^{-1}
Q_{in}	Main inlet flow rate	Varies	mL.min^{-1}
q_{in}	Injection flow rate	Varies	µL.min^{-1}
Q_{out}	Main outlet flow rate	Varies	mL.min^{-1}
q_{out}	Withdrawal flow rate	Varies	µL.min^{-1}
h_{in}	Thickness of specimen lamina	Varies	µm
h_s	Skim height	Varies	µm

Table 1.1 (continued)

d_{out}	Withdrawal slot width	127	µm
d_s	Depression distance	Varies	µm
W_v	Vortex diameter	Varies	µm
S	Mean cell spacing	Varies	-
N	Particle concentration	Varies	m^{-3}
d_c	Cell diameter	Varies	µm

CHAPTER 2 MEASUREMENT OF CELL PHYSICAL PROPERTIES BY DEP-FFF

2.1 INTRODUCTION

In order to understand the operational requirements for a DEP-activated instrument for isolating CTCs efficiently from blood, the first step was to be able to measure the properties of blood and tumor cells that would determine their behavior under DEP-FFF conditions. Earlier approaches for characterizing the DEP properties of cells by conventional DEP and electrorotation methods examined perhaps 20 or so cells in each experiment[12, 35, 38, 64-67] and, while this allowed authors to publish mean and standard deviations of cell dielectric parameters for a number of different cell types, the sampling numbers were too small to provide detailed statistical distributions of the cell parameters, especially with regard to cell subpopulations, for example. Furthermore, in most published reports, typically only one or two cell types were examined because the measurements by conventional methods are so tedious. In order to adequately address the design of an isolator that would be widely applicable to different cancer types and be able to capture cancer cell subpopulations, a far more detailed analysis, involving much larger numbers of cells, was considered to be necessary. Furthermore, this analysis needed to be achieved for many different cancer cell types as well as for all the normal blood cell subpopulations. To achieve this, a much more versatile and rapid measurement approach was required.

It was realized that the DEP-FFF method might be able to solve this measurement problem because the elution profiles from a DEP-FFF device arise from exactly the physical properties of the cells that we need to know to design an efficient isolator. It was reasoned that by better understanding the DEP-FFF process, it would be possible to derive explicit mappings between the DEP-FFF elution behavior of the cells and the required cell physical properties. In this chapter, the cell DEP-FFF elution behavior is analyzed theoretically and methods are developed by which such mappings can be obtained. Using these methods, I was able to study the distributions of cell parameters of 20,000 to 40,000 cells in each of more than 90 different cell types[24], paving the way for a better understanding of the biological basis for the differences between cancer cells and normal blood cells (Chapters 3 and 4)[20, 24] and for designing efficient DEP-FFF isolators (Chapter 5)[23].

2.2 METHOD AND MATERIALS

2.2.1 Biophysical parameter determinations by DEP-FFF

As shown in Chapter 1, DEP-FFF employs the principle of positioning cells in a hydrodynamic flow profile at equilibrium heights that are determined by a balance of DEP, sedimentation and hydrodynamic lift forces (HDLF)[17, 25, 60]. These three forces acting on the cells balance when

$$F_{SED} + F_{DEP} + F_{HDL} = 0. \qquad (2.1)$$

Note that this equation assumes that the cells are freely moving in the hydrodynamic flow profile, which carries them through the chamber. In other words, the cells do not come into contact with the chamber floor, an occurrence that would result not only in an additional reaction force from the floor but also create poorly-defined steric drag between the cells and the floor that would affect their elution times[68]. In order to allow the cell parameters to be measured quantitatively, the free suspension condition of equation (2.1) was always satisfied except when the DEP force was used to trap the cells on the chamber floor (see later). In addition, equation (2.1) assumes that cells do not exert forces on one another that perturb their height or motion. Disruptive cell-cell interaction forces can include cell dipole-dipole interactions caused by the DEP field and hydrodynamic entrainment effects between cells. These forces are negligible if the distance between cells is large. For example, Jones[40, 44] showed that dipole-dipole interactions are negligible if cells are at least 5 diameters apart. During my DEP-FFF experiments, the cell loading concentration easily satisfied these conditions because the cells were calculated to have a mean spacing of greater than 100 µm.

The sedimentation force[25] may be written as

$$F_{sed} = \tfrac{4}{3}\pi \cdot R^3\left(\rho_p - \rho_s\right)g \,. \tag{2.2}$$

For the parallel, interdigitated geometry of the microelectrode array used in my studies (having periodicity *d*), it has been shown that the DEP force at a height *h* in the chamber can be written [17]as

$$F_{DEP} = 352\,\pi\varepsilon_s d^{-3}\left(P(f)\cdot V\right)^2 \exp\left(-\frac{4\pi h}{d}\right)\cdot R^3 \cdot f_{CM}(f). \tag{2.3}$$

The factor $0 \le P(f) \le 1$ corrects for voltage drop at the electrode-eluate interface due to electrode polarization[61]. The complex polarization impedance at that interface can be approximated in terms of an effective polarization resistance R_{pol} and a polarization capacitance C_{pol} [61, 69-71] as

$$Z_{pol}(f) = \frac{R_{pol}}{f^{\frac{1}{2}}} + \frac{i}{2\pi C_{pol} f^{\frac{1}{2}}} \tag{2.4}$$

The impedance of the bulk suspending[61, 69-71] is

$$Z_{bulk}(f) = \frac{R_{bulk}}{1 + i \cdot 2\pi f \cdot R_{bulk} C_{bulk}} \tag{2.5}$$

where R_{bulk} and C_{bulk} result from the conductivity (σ_s) and permittivity (ε_s) of the eluate used to suspend cells in the DEP-FFF channel. For an electrode array comprised of plain, parallel, interdigitated electrode elements having equal width and spacing *d*, the "lumped" area of electrode connected to each pole of the signal generator is $\frac{1}{4}WL$ and the effective spacing of these lumped electrodes is 2*d* [25], giving

$$R_{bulk} = \frac{8d}{\sigma_s WL}, \quad \text{and} \tag{2.6}$$

$$C_{bulk} = \frac{\varepsilon_s WL}{8d}. \tag{2.7}$$

The interface and bulk eluate impedances form a voltage divider for the AC signal that is applied to the electrode array,   and the proportion of the voltage that acts across the bulk the eluate is[25, 61]

$$P(f) = \mathrm{Re}\left(\frac{Z_{bulk}(f)}{Z_{pol}(f)+Z_{bulk}(f)}\right). \qquad (2.8)$$

It follows that the voltage drop term $P(f)$ may be calculated based on the DEP-FFF design parameters. In practice, expression (2.4) for the interfacial impedance $Z_{pol}(f)$ is an approximation that has been shown to depend on the assumption that the electrode-solution interface has specific fractal characteristics. Because there was no way for me to guarantee that this would be the case for the electrode arrays used in my studies, I decided not to rely on this theory. For this reason, a method is developed below to measure $P(f)$ from the DEP-FFF elution behavior of standard particles[24]. Nevertheless, the polarization theory is presented here for the sake of completeness and it could prove useful if microelectrode characteristics can be better defined in the future.

The third force in expression (2.1) is the hydrodynamic lift force. Abkarian *et al.*,[72] through experiments on deformable lipid vesicles, have shown that the HDLF depends upon the deformability of a particle in shear flow according to

$$F_{HDL} = -\eta\,\dot{v}_0\frac{R^3}{h}\cdot\Phi\ . \qquad (2.9)$$

For the parabolic profile of characteristic of Poiseuille flow, which occurs under DEP-FFF conditions, the shear rate at the chamber floor is $\dot{v}_0 = \dfrac{6B}{H^2W}$ where B represents the flow rate through the chamber. The HDLF depends on the initial shape and deformability of a cell as expressed by the dimensionless geometry parameter Φ that has a value ranging between zero and 1. Φ indicates the deviation from sphericity of the cell under the given flow conditions. If a cell is spherical in the absence of flow, then Φ is a measure of how the cell deforms as the flow shear increases. Factors that increase the rigidity of a cell are expected to result in smaller values of Φ.

All of the forces that participate in the force balance of DEP-FFF include the term R^3 so expression (2.1) can be rearranged and simplified to give the volume-independent equation

$$a(\rho_p - \rho_s) \; + \; b \cdot P(f) \cdot V^2 \cdot \exp\left(-\frac{4\pi h}{d}\right) \cdot \left[\frac{f^2 - f_0^{\,2}}{f^2 + 2f_0^{\,2}}\right] \; - \; c \cdot \frac{B \cdot \Phi}{h} = 0 \qquad (2.10)$$

where

$a = \frac{4}{3}\pi g$

$b = 352\pi\varepsilon_s d^{-3}$ and

$c = \dfrac{6\eta}{H^2 W}$.

In accordance with its physical properties (ρ_p, f_0 and Φ), a cell reaches an equilibrium height h that satisfies equation (2.10). The cell will be carried through the DEP-FFF chamber by the fluid flow at a velocity $v_p(h)$ corresponding to its equilibrium height and it will elute from the chamber of length L in a time $T_{elution} = L / v_p(h)$. Therefore, $v_p(h)$ can be easily deduced from the elution properties of the cell.

The velocity at which particles are carried as a function of height in Poiseuille flow has been studied extensively and empirical equations[73] have been given as

$$\frac{v_p(h)}{R\dot{v}_0} = \frac{0.7431\left(1+h/R\right)}{0.6376\ -\ 0.2000\log\left(h/R\right)} \qquad \text{for } \ h \ll R\,;$$

$$\frac{v_p(h)}{R\dot{v}_0} = \left(1+h/R\right)\cdot\left[1-\frac{5}{16}\left(\frac{1}{\left(1+h/R\right)}\right)^3\right] \qquad \text{for } \ h \gg R\,.$$

For the purposes of computing h from $v_p(h)$, these two cases can be blended as

$$v_p(h) = \dot{v}_0\, R\left(1+h/R\right)\cdot\min\left(\frac{0.7431}{0.6376 - 0.2000\log\left(h/R\right)},\ 1-\frac{5}{16}\left(\frac{1}{\left(1+h/R\right)}\right)^3\right). \qquad (2.11)$$

The elution time profiles measured by DEP-FFF can in principle, then, be used to find the cell physical parameters, ρ_p, f_0, and Φ (and derived parameters) by solving expression (2.10) using the value of h derived from the elution time. However, it is not possible to solve for three variables using a single equation and to achieve the desired analysis, it was necessary to take advantage of the way in which the DEP and HDLF forces alter with height. To do this, I undertook three different measurements on the cell suspensions using three different experimental regimes, as follows:

2.2.2 Frequency regimes

2.2.2.1 Low frequency regime

Recalling that the real part of the Clausius-Mossotti factor [44, 45] can be written as

$$f_{CM} = \frac{f^2 - f_o^2}{f^2 + 2f_o^2},$$

then when f is much smaller than f_0, its value approaches $f_{CM} \rightarrow -\frac{1}{2}$. Interestingly, this is completely independent of cell properties indicating that all cells will behave similarly at low frequencies and will be repelled from strong electric field regions at the electrodes by negative DEP. The strong negative DEP force will levitate cells far from the floor (>25µm). At this height, and at the low flow rates used in my experiments (B= 4 mL min^{-1}), F_{HDL} is negligible and it is possible to approximate the force balance expression (2.1) as $F_{SED} + F_{DEP} = 0$, giving

$$\Delta\rho_p = (\rho_p - \rho_s) = \frac{b}{2a} \cdot P(f) \cdot V^2 \cdot \exp\left(-\frac{4\pi h}{d}\right) \qquad (2.12)$$

This maps cell elution times (correspondence to the h values via equation (2.11)) to cell densities for given design and operating conditions if $P(f)$ is known (see later). Transit times through the chamber for cell suspensions were measured at a DEP frequency of f =15 kHz.

2.2.2.2 No DEP regime

When no voltage is applied to the microelectrodes (V=0), the DEP force is zero and only sedimentation and HDLF forces occur as the cells flow through the DEP-FFF chamber[68, 74]. This regime corresponds to the physical chemistry method called sedimentation FFF for which theories have been presented in the literature (Cardot et al)[75]. When the flow rate is sufficient, HDLF lifts cells above the chamber floor so that they avoid contact with it and steric interactions between the cells and the floor are prevented. In this regime, only two forces act on the cells in expression (2.1), namely sedimentation and hydrodynamic lift force and $F_{SED} + F_{DEP} = 0$ [68, 74], giving

$$\Phi \; = \; \frac{ac \cdot h}{B}\left(\rho_p - \rho_s\right) \qquad (2.13)$$

The cell elution times measured in this mode therefore reflect the cell deformability, which controls F_{HDL}, and the cell density, which determines sedimentation. Strictly, then, the distribution of the deformability parameter Φ, cannot be obtained accurately because our knowledge of the cell density in a no-DEP experiment has to rely on a density estimate made from a separate low-frequency DEP-FFF experiment. Most fortunately, the cell density distributions found for each of the many cell types I examined were all extremely narrow (coefficient of variance <10%). In contrast, the deformability parameter Φ exhibited a wide range for each cell type (C.V.s were typically >50%). Because of this, the mean cell density value was used to calculate the mappings from elution times to Φ with the knowledge that the density distribution minimally distorted the Φ profile that was obtained. As a more formal illustration of this point, let us consider two parameters that independently contribute variances *v1* and *v2* to a measured data set. The overall variance will be $v_{effective} = \sqrt{v1^2 + v2^2}$, and for 10% and 50% independently contributing variances, the effective combined variance is only 51%.

In my experiments, I used flow rates *B* of 6 and 10 mL min^{-1} to carry out the elution time. Assuming cell density is independent of flow rate, this provided two separate estimates of the cell Φ profiles.

2.2.2.3 Swept frequency regime

When the applied AC DEP frequency is very high, so that , the Clausius-Mossotti factor approaches +1 and the resulting large positive DEP force strongly attracts cells to the microelectrode array on the chamber floor. Under these conditions, the cells experience very strong steric forces and may be trapped completely at the electrode edges. I found that cell elution times were several thousand seconds, showing that their mean velocity in the chamber was almost negligible compared to 100 to 600 second elution times under the 15 kHz and zero DEP regimes, respectively. This observation provided a method to investigate the cell crossover frequencies. Cells were loaded into the DEP-FFF chamber and subjected to a DEP signal that swept downwards in a logarithmic fashion from 300 kHz to 15 kHz over a 600 second period, spanning frequencies from well above to well below crossover frequencies for all cell types I examined. The DEP force experienced by the cells was initially very high (at 300 kHz) and essentially immobilized them but, as the frequency decreased, the positive DEP force attenuated and fell towards zero as the frequency approached . As the DEP force fell to zero and changed direction to become repulsive, the cells were released from the microelectrode array and started to move in the flow stream. Finally as the frequency sweep continued downwards below, the cells were repelled by negative DEP force which levitated them high above the electrodes into fast moving regions of the flow stream where they were transported quickly through the chamber. In this swept-frequency regime, the total time taken for cells to exit the chamber reflected how long they had to wait before the DEP frequency had swept down to their crossover frequencies, the attractive DEP force attenuated, and the cells were levitated. Thus cells having a high crossover frequency had to wait less time to be released into the flow stream and be eluted than cells having a lower crossover frequency. Thus, the cell elution time was indicative of crossover frequency.

In this case, the complete form of expression (2.10) was used and simulations were run using Matlab scripts to calculate elution mappings for cells having different crossover frequencies, densities and deformability values. As already indicated, cells were found to exhibit narrow distributions of densities but much wider distributions of deformability.

2.2.3 Iterative Corrections to Cell Parameters

The cell density derivation at low frequency assumes that the DEP frequency is much smaller than the cell crossover frequency, $f \ll f_0$, so that $f_{CM} \rightarrow -\frac{1}{2}$. While this condition was found to be easily satisfied for blood cell subpopulations (where, we shall see later, $f_0 > 100$ kHz), I found that some cancer cells had crossover frequencies as low as 25 kHz, which is not far above the DEP operating frequency of 15 kHz. One solution would be to lower the DEP frequency but doing so is far from ideal. At very low frequencies the electrode polarization factor $P(f)$ falls off rapidly, greatly reducing the DEP force and the generation of electrochemical species at the microelectrodes also increases significantly[17, 61]. For these reasons, when my experiments indicated that f_0 was low, I recalculated the cell density using the value $f_{CM} = \frac{f^2 - f_o^2}{f^2 + 2f_o^2}$ rather than $f_{CM} = -\frac{1}{2}$, where f_0 was taken to be the modal value for crossover frequency from the f_0 distribution. The recalculated density value, in turn, was used to obtain a revised value of the deformability factor Φ and together, these two revised values provided a revised f_0 distribution. This cycle was continued iteratively and, as long of the rate of change of parameters was kept below 5% per iteration, it was found to converge on self-consistent values of densities, Φ values and mean crossover frequencies. For consistency in comparing parameters between cell types, I eventually adopted this approach for analyzing all of the DEP-FFF data for different cells.

Having analyzed the theory of DEP-FFF and devised three operating regimes to allow the different cell parameters to be emphasized and estimated from the elution profiles, I next undertook experiments with hollow glass beads, polystyrene beads and cells. The cell experiments will be described in Chapters (3) and (4).

2.2.4 Batch-mode DEP-FFF apparatus and methods

To characterize the bead and cell parameters, I used a batch mode chamber for DEP-FFF experiments that had been developed prior to my studies. The DEP-FFF flow channel was 0.58 mm high x 25 mm wide x 300 mm long and had a floor covered with a flex-circuit patterned with interdigitated 50 μm wide gold-on-copper electrodes spaced 50 μm apart on a Kapton substrate as described in previous publications from the Gascoyne laboratory[19, 25, 76] (part of electrode is shown below in Figure 2.1). 3000 electrode elements ran widthwise across the chamber with alternate elements connected to 2 bus lines energized by a signal generator. This signal generator could deliver sinusoidal signals from 1 kHz to 2 MHz and up to 10 V peak to peak at a maximum current of 3 A RMS[19, 25, 76] to the microelectrode array. For most experiments, I used a 2.8 V peak to peak signal that I monitored with an HP 54601A oscilloscope.

The batch mode is a typical chromatographic approach in which, a volume of particle suspension that is much smaller than the volume of the separation chamber, is injected at one end of the chamber with the eluate flow and DEP field turned off. Cells or beads were allowed to settle onto the floor of the chamber, a process that was complete after 8 minutes of settling time[19, 25, 76].

To initiate DEP-FFF after settling, the DEP signal was turned on and eluate was delivered by a pulseless gear pump (Ismatec, Glattbrugg, Switzerland) via a 0.2 μm inline filter (MediaKap-2, Spectrum Laboratories, Rancho Dominguez, CA). This filter prevented particles from the eluate reservoir interfering with experiments and also allowed cells to be processed by DEP-FFF under sterile conditions[19, 25, 76].

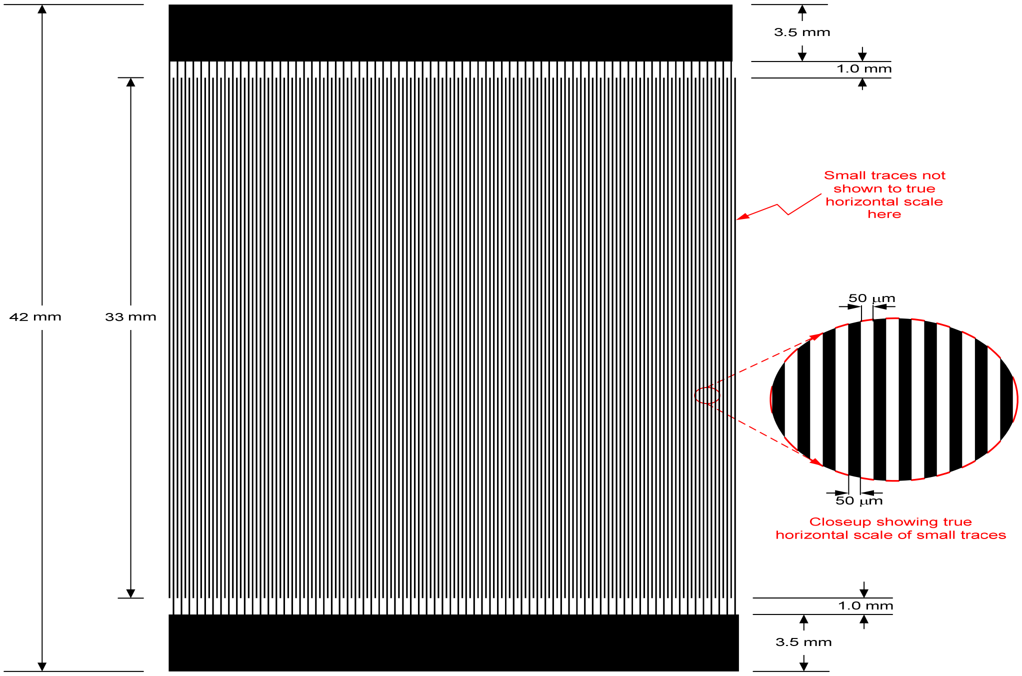

Figure 2.1 The electrode design for DEP-FFF

The eluate buffer[19, 25] used in for DEP-FFF experiments was an aqueous solution of 9.5% sucrose (S7903, Sigma-Aldich, St Louis, MO), 0.1 mg mL^{-1} dextrose (S73418-1, Fisher, Fair Lawn, NJ), 0.1% pluronic F68 (P1300, Sigma-Fisher, St Louis, MO), 0.1% bovine serum albumin (A7906, Sigma-Aldich, St Louis, MO), 1 mM phosphate buffer pH 7.0, 0.1 mM CaAcetate, 0.5 mM MgAcetate and 100 units mL^{-1} catalase (C30, Sigma-Aldich, St Louis, MO), followed by adjustment to conductivity of 30 mS m^{-1} with KCl. For different osmolarity eluate buffers, the sucrose concentration was adjusted in a range of 3.7% for 120 mOs and 9.5% for 320 mOs. Pluronic F68 has been found to protect cell membranes from flow shear-induced damage in bioreactors and is included to help protect cells during injection to the chamber and flowing out through fine PEEK tubing. Dextrose acts as a metabolic source for cells, and catalase has been found to protect cells from low levels of electrochemical species, especially reactive oxygen intermediates, that can be generated at small concentrations by the microelectrodes at low AC field frequencies[19, 22, 25].

The choice of this buffer was based on many years of DEP studies in the Gascoyne laboratory[19, 22, 25]. As indicated earlier, in order to exploit positive as well as negative DEP forces, the suspending medium conductivity needs to be much lower than the cytoplasmic conductivity. The value of 30 mS was chosen because it is far lower than the conductivity of the cytoplasm (~1.2 $S.m^{-1}$), even if the cells undergo some ionic leakage during the experiments, and requires an AC current in my 300 mm long chamber of ~2 A RMS. This is not only within the capabilities of the DEP signal amplifier employed but also results in only about a 2°C temperature rise as the DEP eluate buffer passes through the DEP-FFF chamber. The role of the sucrose is to compensate for osmolarity so that cells are not osmotically stressed when they are suspended in the low ionic strength eluate. Bovine serum albumin ensures that potentially adhesive surfaces in the tubing and separation chamber remain coated with protein and are rendered less adhesive for cells.

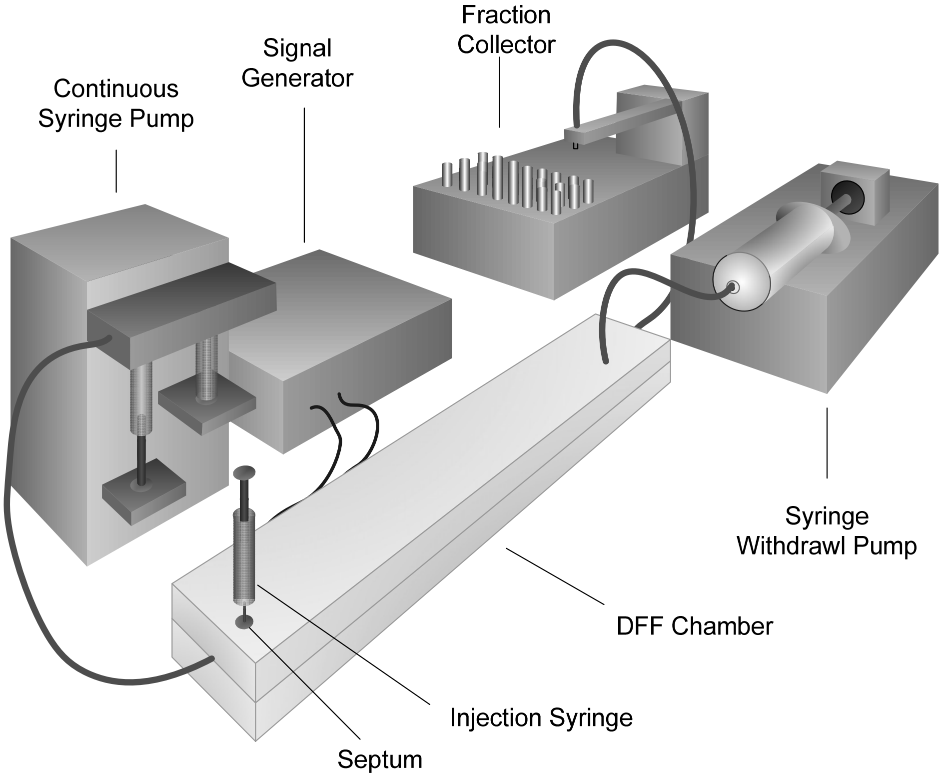

Figure 2.2 Batch-mode DEP-FFF system[19, 25]

Two different methods were used to analyze cells that eluted from the chamber. In one method, the majority of the eluate flow from the upper part of the chamber, which did not contains cells or beads, was withdrawn by a syringe pump. The remaining flow from the chamber, which contained the cells or beads, flowed out from a port at the bottom of the chamber and was collected in timed aliquots by a fraction collector. This method is shown in Figure 2.2 above. In the other method, no withdrawal syringe pump was used and all of the flow from the chamber passed through a particle counter. This counter (PC2400D, ChemTrac Systems, Norcross, GA) employed light scattering to detect particles in eight size interval ranges that could be programmed. In this way, real-time count and size data could be obtained as the cells or beads eluted. The counter was interfaced to a computer with custom software, which plotted individual, size resolved elution profiles for the DEP-FFF experiments. The computer also controlled the DEP signal generator signals and the pumps and allowed DEP frequency sweeps to be conducted automatically, for example. The custom software also recorded the elution data and allowed it to be exported for later analysis by MATLAB scripts or other software.

2.2.5 Hollow glass beads

Unfortunately, as explained earlier, one parameter of the DEP-FFF system could not be explicitly controlled by design or experimental conditions, namely the electrode polarization parameter $P(f)$. To take account of this, I conducted DEP-FFF experiments using hollow glass beads as density standards that I prepared by isopycnic centrifugation separation on a sucrose density gradient[24]. Hollow glass beads (HGB) (Cat. 19823-5, Polysciences, Warrington, PA) of heterogeneous densities and in the size range of 3 to 20 microns were carefully layered onto a stack of 12 glucose concentrations ranging from 50% sucrose at the bottom to 0% sucrose at the top. This stack provided density steps in 5% increments from ρ_s=1230 kg m^{-3} at the bottom to ρ_s=1000 kg m^{-3} on top. The beads and stack were then subjected to centrifugation at 900 g x 45 min. The bead fractions that had sedimented into the sucrose layers of different densities were very carefully pipetted off layer by layer from top to bottom. The isolated bead fractions were washed, suspended in PBS, and used as density standards in low frequency DEP-FFF experiments.

2.3 RESULTS AND DISCUSSIONS

2.3.1 Density Measurement Results

HGBs exhibit stable and uniform dielectric properties because they have a very low dielectric polarizability over an extremely wide range of frequencies. As a result, their crossover frequency f_0 is effectively infinite and $f_{CM} = -0.5$. Therefore, they always experience maximum negative DEP force under DEP-FFF conditions. As shown earlier, the particle volume cancels from the DEP-FFF force balance equation. Therefore, despite their size heterogeneity, HGBs are excellent calibration particles for DEP-FFF purposes.

The different HGB density fractions were subjected to DEP-FFF, allowing $P(f)$ to be estimated and the mapping from elution time to cell density to be determined for the low-frequency DEP regime. The eluting HGBs were measured by the light scatter particle counter. Figure 2.3 (A) shows the transfer function to map elution times to densities that was derived from the HGB experiments at a DEP operating frequency of 15 kHz. The shape of the transfer function agrees well with that expected from DEP-FFF theory at a value of $P(f)$=0.60. Interestingly, though of no bearing to my study, no correlation was observed between HGB size and density.

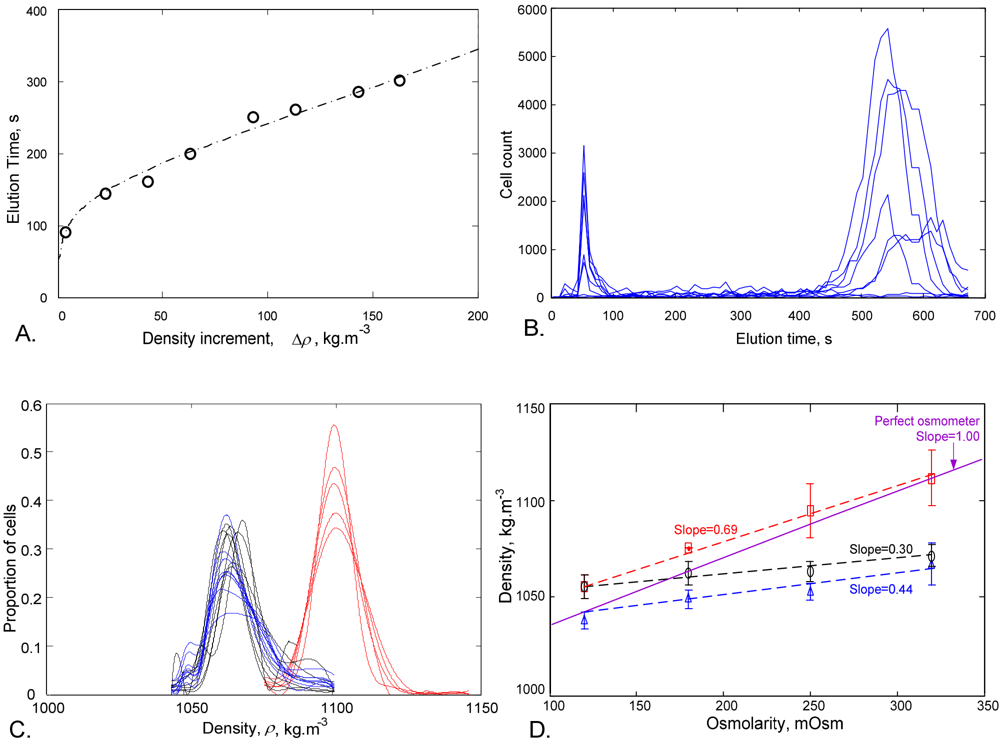

Figure 2.3 (A) Dependency of the dFFF elution time for hollow glass beads as a function of their density difference compared to the eluate buffer. theoretical relationship based on eqn (2) and (3) scaled by the best fit of the voltage loss parameter (see text). (B) Elution profile for MDA-MB-435 cells in an eluate of 250 mOsm at a DEP frequency of 15 kHz (C) Cell density distribution profiles for an eluate of 250 mOsm derived by using the dependency in A as a mapping for elution profiles like those shown in B. (D) Variation of cell density, derived from dFFF, as a function of eluate osmolarity. (Red: erythrocytes; Black: PBMNs; blue: MDA-MB-435 for all panels)

Once $P(f)$ had been determined, it was possible to rapidly profile the density of cells and particles. It turned out that DEP-FFF was a very quick method for obtaining cell density profiles, requiring less than 5 minutes to profile a specimen. While the methods for obtaining, growing and handling cells will be described in detail in Chapter 3, some basic ideas of the DEP-FFF transfer function characteristics will be introduced now using some results for normal blood cells (erythrocytes and PBMNs) and cultured MDA-MB-231 and MDA-MB-435 human breast cancer cells.

The transfer function in Figure 2.3 (A) was used to map elution profiles like that shown in Figure 2.3 (B) to the density distributions for erythrocytes, PBMNs and MDA-MB-435 cells shown in Figure 2.3 (C). The peak density ρ_p = 1100 kg m^{-3} for erythrocytes and the peak density with shoulders from ρ_p = 1055 to 1075 kg m^{-3} for PBMNs agree very well with results reported in the literatures. Densities have not been reported before for MDA-MB-231 and MDA-MB-435 cells but the profile found, ρ_p = 1060 kg m^{-3} for both MDA-MB-231 and 435 cells, overlaps with the density distribution of PBMNs and is consistent with the fact that both PBMNs and those breast cancer lines can be collected over a Histopaque 1077 density gradient.

One way to test DEP-FFF to see if it detects small changes in cell density is to use osmotic effects to manipulate cell volume. As the osmolarity is altered, cells are expected to adjust their cell volumes dynamically by balancing their ion concentrations between inside and outside[77]. DEP-FFF allows this dependency of cell densities on osmolarity to be investigated. Cells were suspended in eluates of different osmolarities ranging from 120 to 320 mOsm. The cell density was then mapped from DEP-FFF elution times and the cell density variance was plotted against osmolarity (Figure 2.3 (D)). A perfect osmometer will follow the Van't Hoff equation and show a linear dependency of density on osmolarity with a slope of unity. In Figure 2.3 (D), erythrocytes showed a slope of 0.69[78], MDA-MB-435 a slope of 0.44, and PBMNs a slope of 0.30. These data are consistent with prior measurements in the literature and show that erythrocytes are reasonably good osmometers but that PBMNs are not. This is because PBMNs have a cell machinery involving ion pumps and chloride channels that allows them to adjust to osmotic processes through a mechanism called dynamic volume regulation. These results show that DEP-FFF can be used to rapidly observe cell osmotic responses and dynamic volume regulation.

2.3.2 Hydrodynamic lift

Cells circulating through blood vessels and small capillaries undergo complex interactions that determine their transport characteristics that depend on flow rate, vessel size and deformation of cell shape[72, 79, 80]. When cells are in vessels that exceed their diameter, flow profile and cell deformation provide hydrodynamic lift that determines how far they are carried from the vessel walls. When the cells enter microcapillaries having a diameter comparable to or smaller than their own then deformability that allows them to squeeze through the vessels plays a key role in their migration. The elution times measured in the no DEP regime allowed the dimensionless geometry deformability parameter Φ to be determined using the mapping shown in Figure 2.4. I found modal values for erythrocytes, PBMNs and MDA-MB-435 cells of $\Phi=0.04$, $\Phi=0.08$ and $\Phi=0.12$, respectively, in suspending medium of physiological osmolarity. The geometric lift factor increases with deviation from sphericity and greater deformability if they are exposed to shear stress, so these results reveal that MDA-MB-435 tumor cells are significantly more deformable than PBMNs and especially erythrocytes. Φ is expected to be less when cells have greater membrane rigidity, such as through the membrane cytoskeleton of spectrin and actin in erythrocytes or have a well developed bulk cytoskeleton of actin filaments and microtubules as in many differentiated cells. It is generally considered that the cytoskeleton is poorly developed and organized in many cancers, suggesting that Φ may be higher in tumor cells.

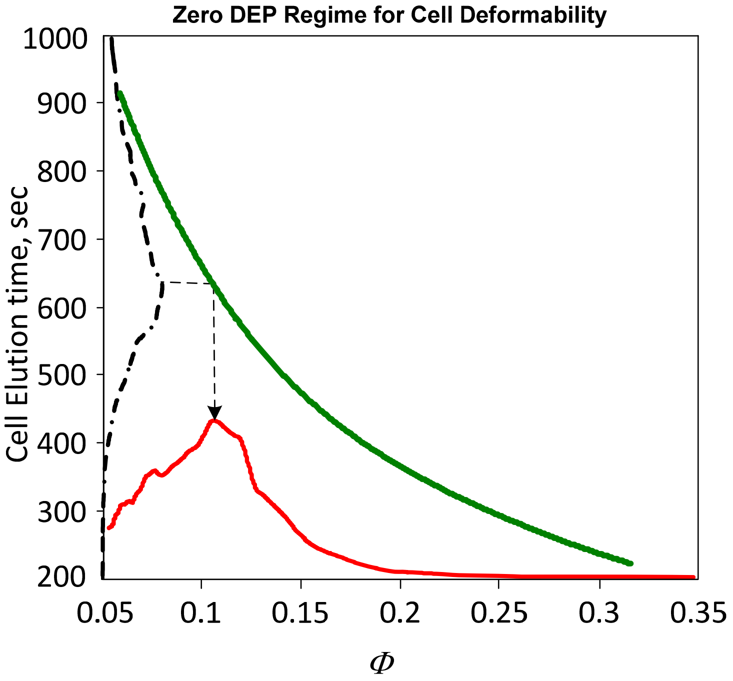

Figure 2.4 Mapping plot between cell elution time and cell deformability[25].

2.3.3 Total capacitance and cell surface area

The crossover frequency is the most difficult parameter to extract from the force balance equation because the DEP force is zero at the crossover frequency and therefore the sedimentation and HDLF forces are always in play when it is being measured.

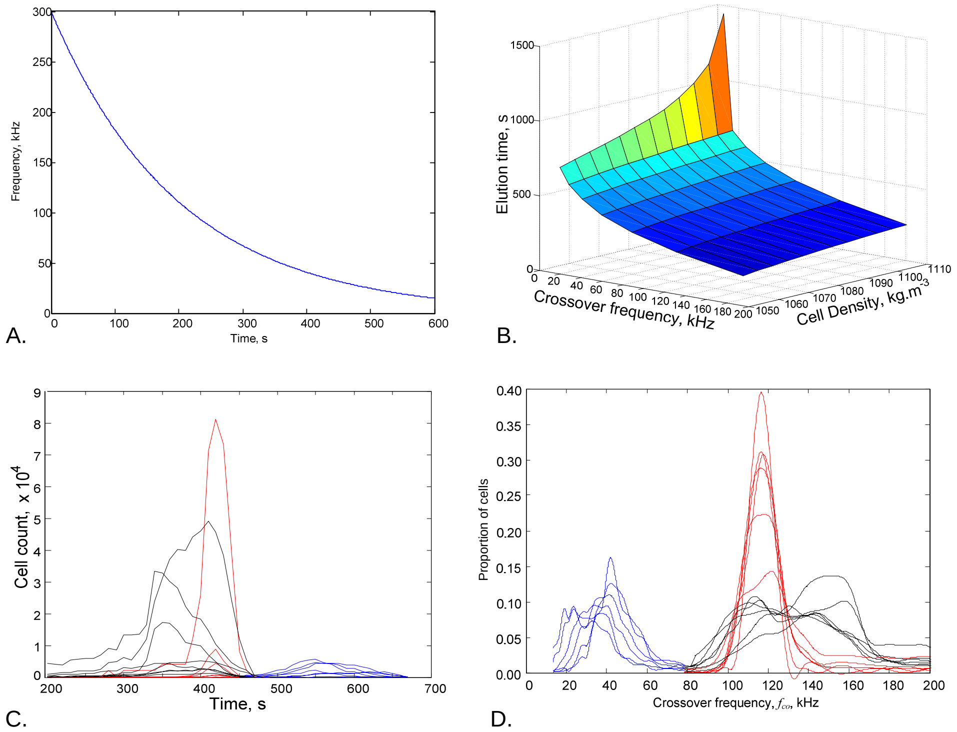

Figure 2.5 (A) Time dependency of the applied DEP field frequency used in the swept frequency DEP-FFF regime. (B) Theoretically derived mapping between cell elution times in swept regime DEP-FFF and the cell DEP crossover frequency for an assumed hydrodynamic lift geometry factor of 0.1 (C) Swept frequency regime DEP-FFF elution profiles for erythrocytes (red), PBMNs (black) and MDA-MB-435 (blue) at 250 mOsm. (D) The distributions of the cell DEP crossover frequencies derived from the elution profiles in C using a polynomial fit to the mapping shown in B.

Therefore, the density ρ_p and the hydrodynamic lift deformability parameter Φ must be considered when mapping cell elution profiles to DEP crossover frequencies. To derive DEP crossover frequencies, the DEP field frequency was swept downwards in a logarithmic pattern as shown in Figure 2.5 (A). Matlab simulations based on the force balance equation 2.10 and eluate flow properties in equation 2.11, a mapping surface for crossover frequencies versus elution time and density is shown in Figure 2.5 (B) with the assumption that the hydrodynamic lift parameter $\Phi = 0.100$. The elution profiles in Figure 2.5 (C) then map to the crossover frequency distributions in Figure 2.4 (D). The mean and standard deviations of the crossover frequencies obtained from these profiles agree well with the DEP crossover frequency and electrorotation data presented in the literature.

No precedent exists for determining DEP crossover frequency profiles, so there is no basis upon which to validate the distributions obtained. Nevertheless, given the requirement to use a single value for Φ in deriving the transfer function, it is clear that the inferred DEP crossover frequency distribution will include broadening caused not only by variances in crossover frequency but also by the coefficient of variance of around 50% in Φ. From a statistical perspective, it is tempting to argue that because the observed coefficient of variance in the crossover frequency, including the contribution from Φ, is around 50%, the coefficient of variance of the DEP crossover frequencies must be much less. Yet the published data that show standard deviations for DEP crossover frequencies that are similar to the standard deviations calculated from my inferred crossover frequency distributions argues against this. The only certainty, is that the true distributions of crossover frequencies can be no broader than those derived by my mapping approach. On that basis, it is possible to assert that a DEP-FFF isolator design for cancer cells that can cope with the inferred distribution of crossover frequencies will definitely be able to cope with the true distribution of crossover frequencies, no matter how narrow it may turn out to be. For this reason, the distributions found for cell crossover frequencies in later chapters are taken to be those inferred from the mappings.

CHAPTER 3 PHYSICAL PROPERTIES OF CANCER CELLS VERSUS NORMAL BLOOD CELL SUBPOPULATIONS

3.1 INTRODUCTION

In this chapter, the methods developed in Chapter 2 are applied to examine the physical properties of different cell types. The overall goal of my research was to develop a method to isolate CTCs from clinical specimens using DEP and, if possible, to design a DEP-FFF isolator that would be broadly applicable to all types of cancer. In order to develop such a broadly applicable design and to predict the optimal cell isolation conditions, I therefore examined the cell properties of a wide range of cancer cell types. To accomplish this, I selected the NCI-60 panel of cancer cell lines. This panel is made up of 60 cell lines recommended for study by the National Cancer Institute that span much of the functional diversity for cancers of 9 organ types and of leukemias that are seen in clinical practice. I applied the DEP-FFF methods of Chapter 2 to characterize these cell lines in order to understand the range of cell properties a cell isolator for CTCs is likely to encounter in practice[22]. Because CTC isolation requires exploitation of differences between cancer cells and blood cells, I also examined the properties of the subpopulations of cells present in normal blood for comparison.

3.2 METHOD AND MATERIALS

3.2.1 Cells

The NCI-60 panel of cancer cell lines was generously made available to me by Dr. Gordon Mills, Director of the Kleberg Center for Molecular Pathways, via the M.D. Anderson Cell Line Core Facility. Over a period of approximately six months, up to three cell lines each week were revived from cryogenic storage by the staff of the Core facility. Each line was grown according to the conditions specified by the American Type Tissue Collection (ATTC) guidelines. The cells were maintained in culture for at least two weeks until they reached a stable growth pattern in which they could be passaged with a seeding density (depending on doubling time) that led the cultures to reach 50-70% confluence every 2 to 3 days and provide cell harvests of high viability. This care was taken to ensure that the cells were healthy and grown under comparable conditions. Cell physical properties are extremely sensitive to stress from overcrowding or media exhaustion and it was considered to be important to avoid such problems so that comparable DEP data would be obtained for the different cell types. In every case, the cell line identity was confirmed by short tandem repeat DNA fingerprinting in the Cell Line Core Facility. I am extremely grateful to the staff of the Cell Line Core Facility and to Ms. Jamileh Noshrari in our own laboratory for their experience and dedicated work in growing these many different cell lines for me.

Typical culture conditions were as follows: cells were seeded into RPMI (Sigma-Aldrich) supplemented with 10% fetal bovine serum (FBS) (GIBCO, Grand Island, NY).

Once they had reached 50-70% confluence after 2 to 3 days of growth, adherent cell lines were harvested by rinsing with calcium- and magnesium-free Hank's buffered saline solution, incubating at 37°C for 5 minutes with Trypsin/EDTA followed by sharp tapping, and neutralization with RPMI+10% FBS. Non-adherent cell cultures were spun down from culture and suspended directly in RPMI + 10% FBS. Following harvest, the cells were counted to ensure >98% viability by trypan blue dye exclusion and they were suspended at ~10^6 cell mL^{-1} in RPMI + 10% FBS in conical tubes ready for DEP analysis.

Blood was drawn from normal volunteers using 10mL EDTA K2/K3 vacutainers (BD, Franklin Lakes, NJ). It was layered onto Histopaque 1077 density medium (Sigma-Aldrich) and centrifuged at 600g x 30 min. The thin layer of PBMNs were pipette off, washed two times, and resuspended in FBS free RPMI.

3.2.2 Dielectrophoretic field-flow fractionation (DEP-FFF)

The DEP-FFF device used in this chapter was the same as that described in chapter 2. The microelectrode array was energized with an AC voltage of 2.8 $V_{p\text{-}p}$ in the frequency range 15 kHz to 300 kHz at currents up to 2.5 A RMS, according to the DEP-FFF regime.

The DEP-FFF buffer consisted of an aqueous solution of 9.5% sucrose (S7903, Sigma-Aldich, St Louis, MO), 0.1 mg mL^{-1} dextrose (S73418-1, Fisher, Fair Lawn, NJ), 0.1% pluronic F68 (P1300, Sigma-Aldich), 0.1% bovine serum albumin (A7906, Sigma-Aldich), 1 mM phosphate buffer pH 7.0, 0.1 mM Ca acetate, 0.5 mM Mg acetate and 100 units mL^{-1} catalase (C30, Sigma-Aldich). The conductivity was adjusted to 30 mS m^{-1} by adding KCl. This deviated from the DEP buffer used in Chapter 2 by the addition of calcium and magnesium, divalent cations that have been shown to stabilize membrane integrity[19, 22, 25].

As before, the sucrose compensated for the low ionic concentration of the eluate buffer, adjusting the osmolarity to the normal physiological of 315 mOs kg^{-1}. Dextrose acted as a metabolic energy source to help maintain cell viability, pluronic played a role on an anti-damage surfactant for cells as they flowed near the surfaces of tubing and the DEP chamber, bovine serum albumin provided a protective coating on chamber and tube surfaces that prevented cell adhesion. Calcium and magnesium stabilized cell membrane structure and integrity and catalase provided protection from cell damage by low-level H_2O_2, a byproduct of electrochemical processes when the DEP electrodes were energized especially at frequencies below 25 kHz[19, 22, 25].

For each DEP-FFF run, a 30µL aliquot of cell suspension (10^6 cell mL^{-1}) was diluted with 300 µL of DEP buffer, and this mixture was injected into the front end of the DEP chamber with the eluate flow and DEP field turned off. Cells were allowed to settle for 8 minutes. Then, flow of elute buffer was initiated at 4 mL/min and one of three DEP signals (see below) was applied to the microelectrode array in order to investigate the elution profiles. For the NCI-60 studies, the cells were counted and sized by laser light scatter (PC2400D, ChemTrac Systems, Norcross, GA) as they emerged from the DEP-FFF chamber.

To determine the biophysical properties of the various cell types in the NCI-60 panel, elution profiles were measured for three DEP-FFF conditions to derive the parameters contributing to F_{SED}, F_{DEP} and F_{HDL} as explained in Chapter 2, with:

(i) A constant DEP field frequency of 15 kHz;

(ii) No DEP field;

(iii) A logarithmically-swept DEP frequency from 300 kHz to 15 KHz over 600 seconds.

To derive the cell biophysical parameters from the three cell elution profiles, a MATLAB script was used. The script algorithm first assumed that the mean cell crossover frequency was $f_o = 50$ kHz and that the mean cell deformability factor was $\Phi = 0.1$. The following steps were then iterated until the cell parameters converged on self-consistent values:

(a) The cell elution profile at the fixed frequency of 15 kHz run was mapped to differential cell densities $\Delta\rho$ for the estimated values of f_o and Φ;

(b) Based on the mean value of $\Delta\rho$ derived from (a), cell elution times for the "no DEP" run were mapped to derive the distribution for the cell mechanical deformability factor Φ ;

(c) Based on the present values of mean $\Delta\rho$ and mean Φ derived from (a) and (b), cell elution times for the "swept-frequency" run were mapped to derive the cell crossover frequency, f_o, profile.

(d) Steps (a), (b) and (c) were iterated until $\Delta\rho$, Φ and f_o converged to solutions that were consistent with the cell elution profiles observed under all three DEP-FFF conditions.

3.3 RESULTS AND DISCUSSION

3.3.1 Density and DEP crossover frequency distributions

Figure 3.1 shows typical elution profiles under the three different DEP-FFF regimes, designated DEP 15 kHz, sedFFF (no DEP signal) and DEP swept, respectively. Panels A and B show the differences of these three profiles for SF295 glioblastoma and MOLT4 leukemia cell lines, respectively. The profiles clearly show that these cell lines have different physical properties.

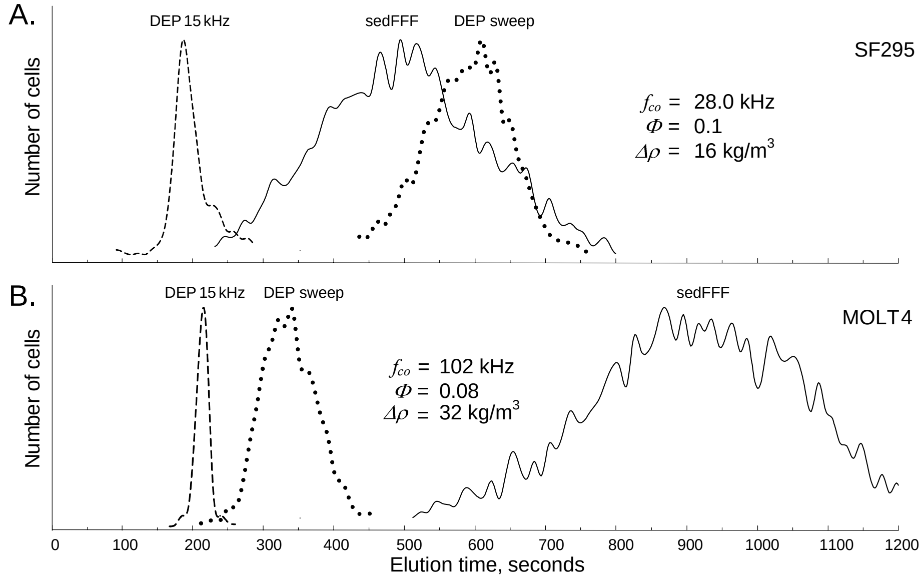

Figure 3.1 DEP-FFF elution profiles for (A) SF295 human glioblastoma cells and (B) MOLT4 human acute lymphoblastic leukemia cells demonstrating the behavior of NCI-60 cells having differences in their density, dielectric and hydrodynamic lift properties. The elution profiles for 15 kHz DEP reflect predominantly cell density differences; those for no DEP (sedFFF) reflect cell density and hydrodynamic lift effects; and those using a DEP frequency sweep reflect the combination of sedimentation, hydrodynamic lift and DEP crossover frequency effects.

At 15 kHz the MOLT 4 cells eluted more slowly than SF 295 showing that the DEP force did not levitate the MOLT 4 cells as high as SF 295. This shows that MOLT 4 cells are denser than SF 295 cells.

The profiles for the no DEP signal regime show that SF 295 cells elute much faster than MOLT 4 cells. Analysis shows that this can mostly be understood just in terms of the density difference although SF 295 cells are also slightly more deformable than MOLT 4 cells. Finally, the much slower elution profile of SF295 cells than MOLT 4 cells under swept frequency DEP-FFF conditions shows that the SF295 cells had to wait much longer in the downward sweeping DEP frequency signal before they were released than the MOLT4 cells. This reveals that SF 295 cells had a much lower crossover frequency than the MOLT 4 cells.

Three elution profiles, like those shown in each panel of Figure 3.1, were obtained for each of the cell lines in the NCI-60 panel and for several blood cell subpopulations, providing the density ρ_p, crossover frequency f_o, and cell mechanical deformability Φ parameters for each cell type. In general, the statistical distributions of the parameters, found by mapping the elution profiles into parameter space, were asymmetrical and could be approximated by skew-normal statistical distributions. Therefore, the cell data for the NCI-60 panel were summarized giving the mean, standard deviation, and skew for each derived parameter from the DEP-FFF measurements. To represent these data graphically while allowing the extent of overlap of the distributions of different cell types to be visualized, Dr. Gascoyne proposed making plots in which the symbols took the forms of their skew-normal probability distributions. Data for the cell density distributions for the NCI-60 panel of cell lines are shown in Figure 3.2 using this representation. The densities for tumor cell types in the NCI-60 panel ranged from 1048 to 1068 kg m^{-3}, except for BT-549 (one of five breast cancers) and HOP-62 (one of nine non-small cell lung cancers).

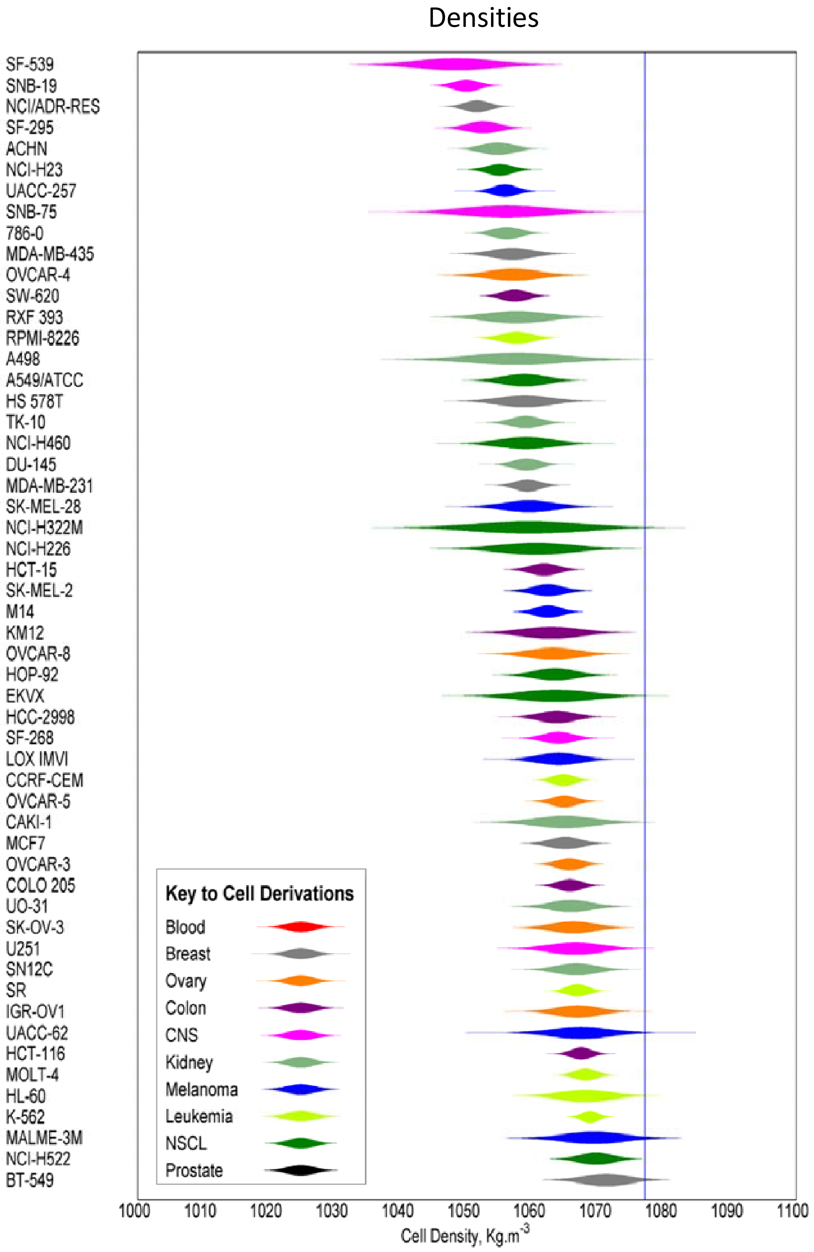

Figure 3.2 Densities of the NCI-60 cell types deduced from DEP-FFF analysis of the cells and shown in ascending order. The thickness of each scale bar represents the number of cells at a given density relative to the mode, which has maximum thickness, based on skew-normal distributions. The blue line shows the density of Histopaque 1077 and Lymphocyte Separation Medium (LSM) of 1077 kg/m3

Jones has shown that cells experience dipole-dipole interactions in an AC electric field if they are less than 5 diameters[16, 19] apart and this represents a difficulty for CTC isolation because the concentration of erythrocytes in the blood (~4 x 10^9 mL^{-1}) is so high that they are spaced far closer together than 5 diameters. As a result, CTC isolation from blood cells by DEP must be preceded by a debulking step in which the erythrocytes (approximately 40% of the volume of whole blood) are removed. Once the erythrocytes are removed, the cell concentration is dilute enough for DEP isolation to proceed without cell-cell interactions. To remove the erythrocytes, either targeted lysis of erythrocytes or centrifugation of the specimen over a density gradient medium (histopaque or lymphocyte separation medium (LSM or Ficoll-Hypaque with a density of 1077 kg m^{-3}) can be used. The lysis buffer could result in damage to tumor cells if those do not possess an adequate dynamic volume response to compensate for osmotic stress. This damage might confound proteomic or gene expression analysis of viable tumor cells. On the other hand, while centrifugation can eliminate erythrocytes without damaging the cancer cells, it is only applicable if the cancer cells exhibit a low enough density to be retained on a density gradient while erythrocytes are not. There have been arguments in the literature as to whether cancer cells have a density that allows them to be retained on Histopaque yet there appear to be no reports of cancer cell density distribution measurements. Figure 3.1 resolves this issue entirely by providing, for the first time, the cell density distributions for all cancer types in the NCI-60 panel and shows that these are all distributed below 1077 kg m^{-3}. This demonstrates that cancer cells will be retained without significant loss along with PBMNs through density gradient separation of whole blood specimens over standard Histopaque 1077 kg m^{-3} density gradient medium. Therefore, standard density gradient separation is applicable to the debulking of erythrocytes without significant loss of tumor cells, assuming that the cell density distributions I observed for the NCI-60 lines are similar to those of CTCs in cancer patient blood. Interestingly, a commercial system is available that purports to enable highly efficient isolation of CTCs from PBMNs through centrifugation over a density gradient of only 1060 kg m^{-3}[81, 82]. My work does not validate that approach, notwithstanding that it is commercially available. Figure 3.2 clearly shows that while a 1060 kg m^{-3} density gradient medium will retain the majority of cells in many types of cancers, there are also may types of cancer cells having densities greater than monocytes (ρ_p=1063 kg m^{-3}) and lymphocytes (ρ_p=1071 kg m^{-3})[81]. These would be lost by centrifugation over a density gradient medium below 1077 kg m^{-3}.

The DEP crossover frequency data, including that for peripheral blood cell populations, derived from my DEP-FFF analysis is shown in Figure 3.3 at an eluate conductivity of 30 mS m^{-1}. Significantly, the values of DEP crossover frequencies derived for cell types in the NCI-60 panel for which DEP properties are reported in the literature agreed well with my findings, showing that the DEP-FFF method provides results that are consistent with the established, though painfully tedious, single-cell DEP-crossover and electrorotation methodologies. The shapes of the symbols used to represent the cells in Figure 3.3 again show the skew-normal distributions in the data to facilitate simple visualization and comparison among cell types. Figure 3.3 shows that all of the peripheral blood cell subpopulations had much higher crossover frequencies than the cancer cell types that grew in adherent cultures in the NCI-60 panel. Only three of the leukemia cell types in the NCI-60 panel, namely SR, MOLT-4, and CCRF-CEM exhibited crossover frequencies that were close to those of any blood cell types (monocytes and CD34+ hemopoietic cells).

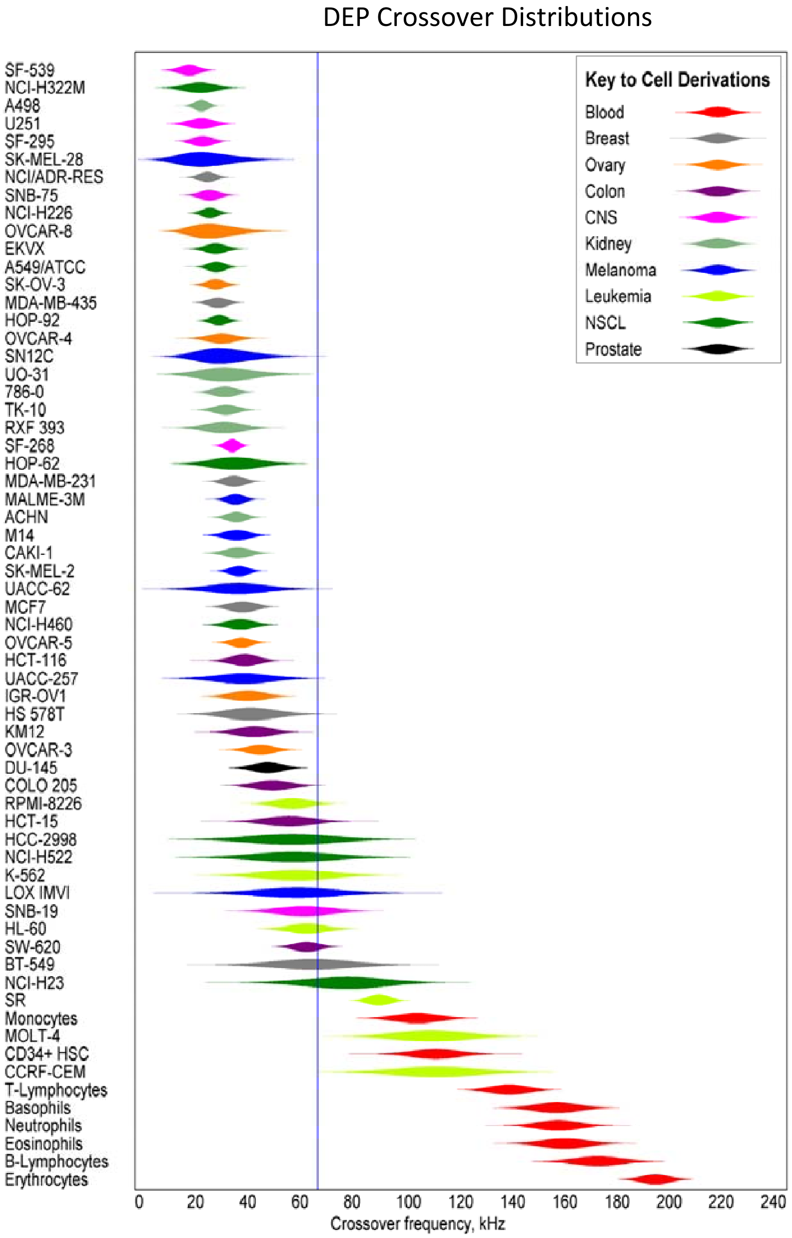

Figure 3.3 DEP crossover frequencies of the NCI-60 cell types and normal peripheral blood cells deduced from DEP-FFF analysis shown in ascending order at a suspension conductivity of 30 mS/m. The thickness of each scale bar represents the number of cells at a given crossover frequency relative to the mode, which has maximum thickness, based on skew-normal distributions. The blue line at 65 kHz shows a possible choice for a DEP-FFF operating frequency that should be able to isolate NCI-60 cell types, except leukemia lines, from normal blood cells.

In principle, the DEP force can be used to manipulate, enrich or even isolate cells according to the dielectric properties of the cells. As shown in Chapter 1, mammalian cell dielectric properties may be expressed in terms of the cell crossover frequency, which indicates the characteristic DEP frequency at which the DEP force is zero as it changes direction as the frequency is altered. The fact that different cell lines exhibit different crossover frequencies indicates that the cells embody differences in cell structure. All tumor types of the NCI-60 panel except for the leukemia-derived lines exhibited significantly smaller crossover frequencies than the normal peripheral blood cell subpopulations. However, large differences in crossover frequencies are not apparent when comparing cell lines grouped by different organ types. Thus Figure 3.4, which illustrates the crossover frequencies with means and standard deviations for the cell lines grouped by organ of origin, reveals differences only between solid organ-derived, leukemia-derived, and peripheral blood derived cells. It follows that DEP is unlikely to be useful for discriminating between solid cancers from different organs.

Nevertheless, this finding is not disappointing for CTC isolation. On the contrary, it means that CTCs from essentially every type of solid tumor will respond to DEP similarly. At a DEP frequency of 65 kHz, shown by the blue line in Figures 3.3 and 3.4, ALL cancer cells from solid tumors exhibit positive DEP and ALL peripheral blood cell subpopulations exhibit negative DEP. This result is quite remarkable, because it suggests that a single set of operating conditions can be applied in a DEP-FFF device to isolate cancer cells derived from all kinds of solid tumors. If CTCs in clinical specimens have dielectric properties that are broadly similar to those of the cell types in the NCI-60 panel, it implies that prior knowledge of the cancer type is not required to enable the isolation of CTCs; a single set of DEP operating parameters apply to all types of solid tumor CTCs.

Clearly, this universality has important implications for the design and application of DEP-FFF isolators.

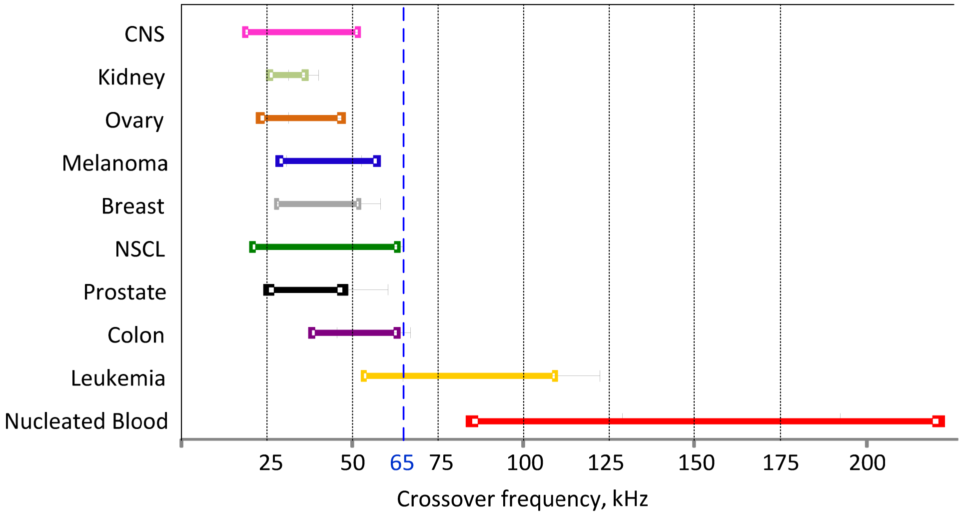

Figure 3.4 Range of DEP crossover frequencies ± 1 standard deviation of the NCI-60 cell types and normal peripheral blood cells deduced from DEP-FFF analysis at a suspension conductivity of 30 mS/m by tissue origin. The blue line at 65 kHz shows a possible choice for a DEP-FFF operating frequency that would isolate essentially all NCI-60 cell types except leukemia lines from blood.

It is also significant that the blood cell subpopulations exhibited small standard deviations in crossover frequencies, ensuring that the crossover frequency distributions of the cancer cells are well separated from those of the blood cells. In practice the population of PBMNs is much higher than the number of CTCs (10 mL patient blood contains ~ 4 x 10^7 PBMNs having a density below 1077 kg.m^{-3} and perhaps 0 ~ 200 CTCs). Only a very tiny overlap in statistical distributions would result in the collection of a large number of blood cells and, therefore, very impure CTC isolates. The large gap between the distributions shows that it should be possible to isolate CTCs with high purity.

The leukemia-derived lines in the NCI-60 panel have crossover frequencies that are less clearly distinct than the solid tumor lines from the peripheral blood cell subpopulations. At the operating frequency of 65 kHz shown by the blue line in Figures 3.3 and 3.4, the leukemic cells cannot be isolated as efficiently from the peripheral blood cell subpopulations. Nevertheless, DEP may still be used to concentrate the leukemia cells from blood. This agrees with previously published work that showed the enrichment of HL-60 leukemia cells from blood cells[38].

3.3.2 Demonstration of the separation of tumor cells from PBMNs

The separation of tumor cells from PBMNs by batch mode DEP-FFF was demonstrated in this laboratory before I started my project[19, 25]. However, having analyzed the DEP theory in more detail and derived the above findings about differences between cancer cells derived from solid tumors and leukemias, it was useful to revisit those earlier findings[38]. To do this I chose to spike MDA-MB-231 (breast cancer) and HL-60 (promyelocytic leukemia) cells into normal PBMNs in different experiments and then to subject these cell mixtures to DEP-FFF separations by batch mode DEP-FFF.

PBMNs were obtained from normal blood by centrifugation over Histopaque 1077. MDA-MB-435 and HL-60 cells were cultured as described earlier. After harvest, the cells were incubated for 15 minutes with 5 $\mu g.mL^{-1}$ calcein-AM viable cell stain (L-3224, Molecular Probes, Life Technologies, Eugene, OR) to make them green-fluorescent for later tracking. Cells were counted and their viability was shown to be above 98% by trypan blue dye exclusion. Approximately 100,000 cancer cells were spiked into 10^6 PBMNs in 1 mL RPMI in each specimen.

DEP-FFF was conducted under the same conditions as for the characterization of the NCI-60 cells in the previous experiments except that the applied frequency was maintained at 65 kHz for the MDA-MB-231/PBMN cell mixture and at 80 kHz for the HL-60/PBMN mixture during the runs. The elution profiles obtained for the two suspensions are shown in Figure 3.5.

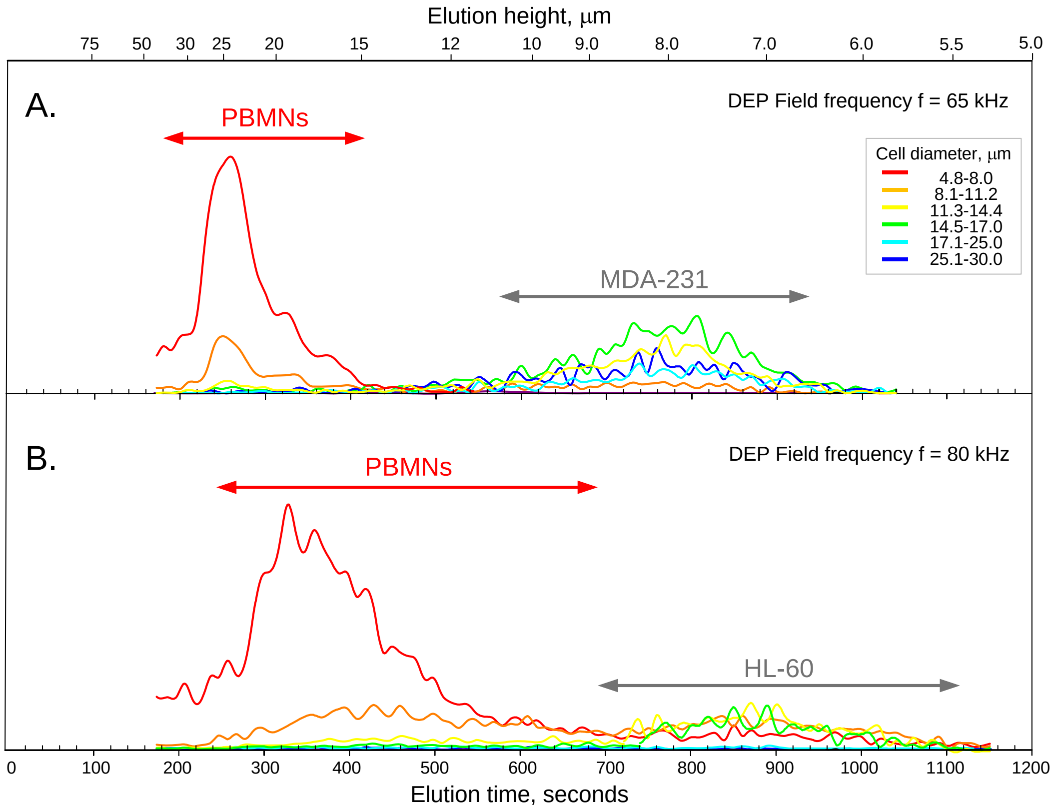

Figure 3.5 Batch-mode DEP-FFF elution profiles for two mixtures of cancer cells with normal peripheral blood mononuclear cells: (A) Normal PBMNs + MDA-MB-231 breast tumor cells run at a DEP operating frequency of 65 kHz; (B) Normal PBMNs + HL-60 promyelocytic leukemia cells run at 80kHz. The different colors denote cells of differing size ranges detected by the PC2400 particle counter used to measure cell elution.

To allow interpretation of the results, the height at which the different cell types traversed the DEP-FFF chamber was calculated from the elution times and is shown plotted at the top. Figure 3.5(A) shows the elution profile for the mixture of PBMNs and MDA-MB-231 cells at a DEP frequency of 65 kHz. At this frequency, the negative DEP force repelled PBMNs between 15 and 30 um above the chamber floor into the fast flowing eluate, resulting is a single elution peak that emerged between 180 and 400 seconds after the run was initiated. MDA-MB-231 cells were eluted much more slowly, being pulled by positive DEP towards the microelectrode array on the chamber floor. These cancer cells traversed the chamber at equilibrium heights between 6 and 11 um above the chamber floor (approximately the cell radius) and eluted between 520 and 1000 seconds after the run was commenced. These results meet all expectations of the DEP-FFF theory based on the observed cell properties.

Of great significance from the perspective of CTC isolation is that the cell line I chose in this experiment, MDA-MB-231 is a so-called triple-negative breast cancer, meaning that it does not express estrogen, progesterone or HER-2 receptors. This makes it a very difficult cancer to treat from a clinical perspective. Furthermore, this cell line does not express the epithelial cell marker EpCAM either. This means that it could not be detected by the currently accepted clinical method for CTC analysis, which depends on EpCAM for antigen-targeted isolation[83, 84]. DEP-FFF depends on cell structural properties and is independent of cell surface antigens. Figure 3.5, then, depicts a successful cancer cell isolation from blood cells by DEP-FFF that is not achievable by current clinical methods.

In Figure 3.5 (B), the elution profile is shown for HL-60 cells (promyelocytic leukemia cancer) co-suspended with PBMNs at an applied 80 kHz DEP field. This frequency was chosen to be midway between the crossover frequencies of HL-60 and

PBMNs. This frequency levitated lymphocytes to heights between 12 and 25 μm above the floor with an elution peak from 250 to 500 seconds after the run started. Other mononuclear were eluted even slower, emerging in a broad peak between 300 and 750 seconds that reflects equilibrium heights of 9 to 20 μm above the floor. The HL-60 cells eluated between 730 and 1100 seconds, reflecting equilibrium heights in the DEP-FFF chamber of 5.5 to 9 μm above the chamber floor.

This comparison between elution profiles of cells from a solid cancer and a leukemia confirms that the cells from the solid tumor, MDA-MB-231, can be efficiently isolated from PBMNs because of the low crossover frequency of the cancer cells. The leukemia, HL-60, however, cannot be isolated so efficiently because it has a higher crossover frequency.

3.3.3 Cell dielectric differences

In order to understand why cells from solid tumors exhibit consistently lower crossover frequencies compared to blood cells, it is crucial to understand the origin of the differences in their dielectric properties in biological terms. As already discussed in Chapter 1[41], a mammalian cell that has relaxed to a spherical shape when it is suspended in an eluate buffer exhibits a DEP crossover frequency $f_o \approx \sigma_s \cdot \left(\sqrt{2}\pi \cdot R \cdot C_{mem}\right)^{-1}$, where C_{mem} is the membrane capacitance per unit area of the cell plasma membrane. Clearly, crossover frequency differences might be related to differences in either R or C_{mem}. Previous studies revealed that C_{mem} plays the major role and, from a physics standpoint, differences in membrane composition, thickness or area are all possible explanations for these differences in C_{mem}. Electron microscopy and biochemistry, however, show that composition and thickness play only a minor role in determining C_{mem} [35, 85]. Indeed, this lab showed some time ago that it is cell plasma membrane area associated with cell surface features including ruffles, folds and microvilli that has the most important role in determining cell crossover frequencies[24, 41]. To formalize this, we can use the knowledge that the capacitance of smooth plasma membrane has a uniform value of $C_0 \approx 9$ mF m^{-2}[86]. Surface morphology involves folds or crinkles of the membrane of a cell and this increases its effective area so that it is larger than it would be for a perfectly smooth membrane by a folding factor ϕ. In general, $\phi \geq 1$, so that the specific capacitance of cells can be expressed as $C_{mem} = \phi C_0$. Consequently, the cell crossover frequency can be written $f_o \approx \sigma_s \cdot \left(\sqrt{2}\ \pi.R.\phi \cdot C_0\right)^{-1}$. The relationship between cell surface capacitance and morphology is now well established and this expression, derived by Gascoyne's laboratory some years ago, has become standard in the field. It follow that the crossover frequencies for the NCI-60 and blood cells can be described in terms of their membrane folding factors ϕ. The low crossover frequencies of cancer cells means that they have larger folding factors (as well as larger sizes) than blood cells. Understanding the biological reasons for these differences in folding factors will form the the subject for Chapter 4.

CHAPTER 4 RELATIONSHIP BETWEEN CELL MORPHOLOGY AND CELL DIELECTRIC PROPERTIES

4.1 INTRODUCTION

The data for the NCI-60 cells obtained in Chapter 3 demonstrated that cancer cell lines derived from solid tumors had DEP crossover frequencies that were substantially lower than those found for normal subpopulations of peripheral blood cells. Leukemia cell lines exhibited crossover frequencies that were intermediate. Based on the findings from earlier studies, it was possible to interpret these results in terms of differences in cell surface morphology that led cells to have surface areas that were larger than would be expected for perfectly smooth spheres. While it is interesting that the NCI-60 cancer cells apparently had consistently greater surface areas than blood cells, it is unreasonable to suppose that this would be the case for all types of cancer without discovering a biological basis for the finding that could reasonably be extrapolated to other cancer types.

The NCI-60 cell panel includes cell lines that present a wide variety of external morphologies in culture and in this chapter, I examine the relationships between the morphologies of the different cell types during growth and the subsequent DEP crossover frequency properties they exhibited when suspended in eluate buffer after harvest.

4.2 METHODS AND MATERIALS

4.2.1 Cell specimens

The NCI-60 cells were grown, and the blood cells were obtained, as described in Chapter 3 except that some supplementary experiments were conducted to investigate whether trypsinization during harvest affected the subsequent cell dielectric suspensions of the cells. To accomplish this, pairs of flasks containing the same cell types were grown. One flask of each pair was harvested by trypsinization at 37°C for 5 minutes while the second was harvested by rinsing twice in calcium-magnesium-free RPMI and incubation with 5 mM EGTA for 5 to 10 minutes. This latter procedure released the cells from the culture flasks in large sheets and the cell suspension had to be tapped sharply to create a suspension of single cells. While this process was not very efficient, it provided enough single cells to compare with the parallel, trypsinized specimen. Remarkably, no difference was seen in the DEP-FFF properties of the parallel cultures harvested in these two ways. One by-product of the experiment, however, was the opportunity to observe the DEP-FFF behavior of clumps of cells in the un-trypsinized specimens. Small clumps of up to 5 cells showed DEP-FFF properties that were consistent with cancer cells, showing that DEP-FFF isolation of clumps of CTCs should be as effective as the isolation of individual CTCs.

One additional cell type was used in the morphological studies, namely primary human ovarian tumor cells that were collected from ascitic fluid that had been withdrawn during routine treatment of a patient with stage 3c serous ovarian cancer. This specimen was obtained under an IRB approval protocol (number: LAB07-0108, explained later) and with patient consent. The tumor cells were recovered by gently centrifuging the ascitic fluid at 600g for 15 min and then resuspending the cell pellet in RPMI medium.

4.2.2 Morphological studies

The morphologies of forty of the NCI-60 cell lines were examined while they were growing in culture just prior to being harvested for DEP-FFF experiments. To allow comparisons to be made between the cell lines, which were examined in batches of 2 or 3 per week over a 6 month period, the cultures were photographed under phase contrast microscopy. An example of the variety of cell morphologies observed for the NCI-60 cell lines is shown in Figure 4.1

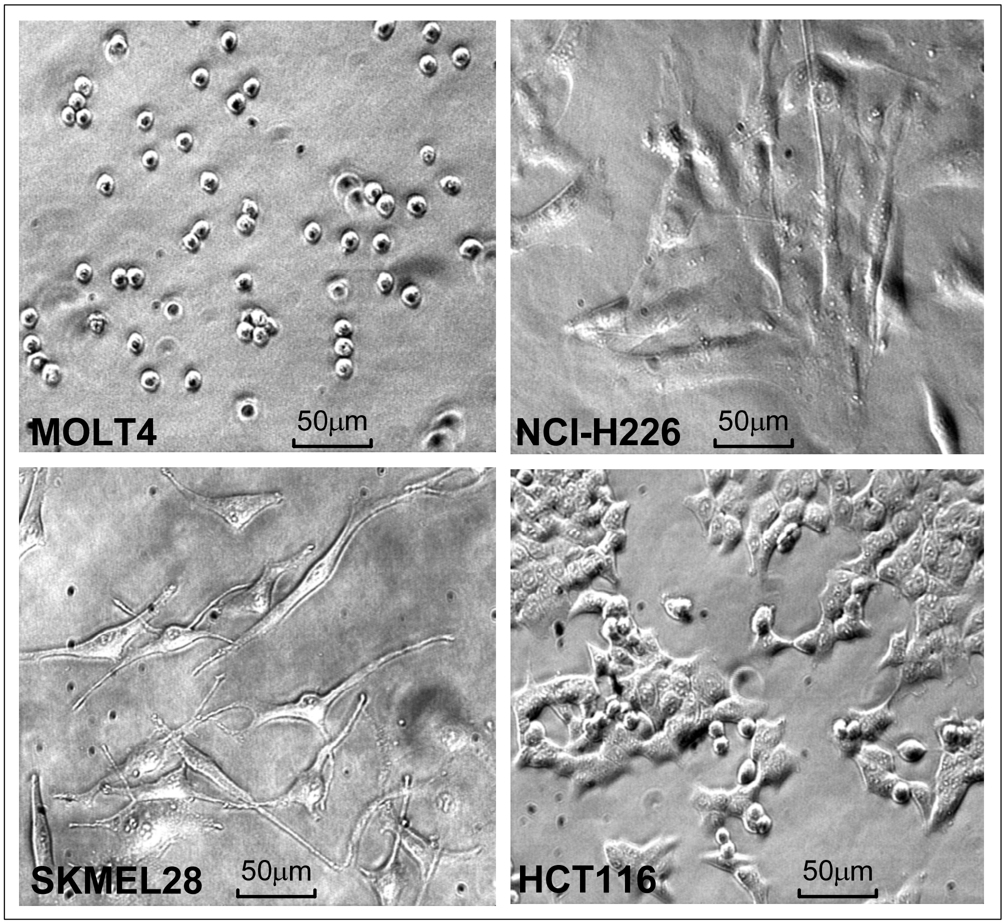

Figure 4.1 Micrographs showing morphological variations amongst the NCI-60 panel of cultured cell lines and illustrating the surface spreading, projections and roughness features used as indicators of increased cell surface area compared with a perfectly smooth, spherical cell (see later). MOLT4 (an acute lymphoblastic leukemia) shows a spherical exterior morphology with little cell flattening, no projections and relatively smooth cell surface appearance. This is as close to a smooth, spherical reference cell type of minimal surface area as was found in the NCI-60 panel. NCI-H226 (a non-small cell lung cancer) exhibits cell flattening resulting from cell spreading on the surface of the culture flask with projections and membrane surface roughness also apparent in some cells. SKMEL28 (a melanoma) demonstrates marked dendritic projections with minor flattening and occasional cell surface roughness. HCT116 (a colon cancer) shows marked surface roughness, with minor flattening and projections. In general, cell lines in the NCI-60 panel showed combinations of these gross morphological traits that were expected to contribute to increased cell surface areas compared with smooth, spherical spheres.

My first thought for analyzing the physical appearance of the cells was to apply image analysis in order to quantify morphological differences between the cells in the photographs of the cultures. However, in consultation with two M.D. Anderson professors of pathology (Dr. Frederick Becker and Dr. Savitri Krishnamurthy), two cytologists (Ms. Jamileh Noshari and Dr. Katherine Stemke-Hale) and my adviser Dr. Peter Gascoyne, it became clear that quantifying not only the diversity of morphological complexities of the cells but also taking into account the random degrees of connectivity between neighboring cells within each photograph would be far too complex a task for available image analysis algorithms. Instead, these advisers suggested using their experience and agreed to independently review the 40 photographs and apply a visual scoring system to quantify, by eye, the overall morphological characteristics of each cell line. The scoring system devised for this purpose defined three primary morphological characteristics of the cells that were expected to make significant contributions to enlarging their cell membrane surface area compared with smooth spherical cells of corresponding volume. These attributes were cell flattening and spreading on the bottom of the culture flask (designated by a parameter F), cell elongation and dendritic projections (designated by a parameter P), and cell membrane surface and peripheral roughness associated with small-scale ruffles, folds and microvilli (designated by a parameter R). A scoring guide was developed to help quantify the extent to which each of these morphological attributes contributed to enhancing total cell membrane area in comparison to smooth, spherical cells having the same volume. This guide was constructed with the help of MATLAB scripts that generated pictures of “cells” having identical volumes but surface areas enhanced by factors of 1.5, 2.0, and 3.0 compared with smooth spheres (see Figure 4.2). Four of the NCI-60 cell lines manifesting these features are compared in the photomicrographs in Figure 4.1.

The five volunteers judged the cell morphologies of the 40 cell photographs independently and gave each scores between 1 and 3 for each of the parameters *F*, *P* and *R*. I tabulated these scores and combined them to create an overall membrane area morphological factor

$$M = \left(F + P + R\right)/3\,. \tag{4.1}$$

Means and standard deviations for the scores of the five volunteers were computed. Using this scoring principle, a cell line morphological factor $M = 1$ indicates a smooth, round cell with no spreading or projections while a factor $M = 3$ defines a highly flattened cell with extensive projections and striking surface roughness.

To examine the human primary ovarian cancer cells obtained from ascitic fluid , these cells were spun down onto a slide using a CytoSpin centrifuge and stained with Wright-Giemsa stain prior to being photographed.

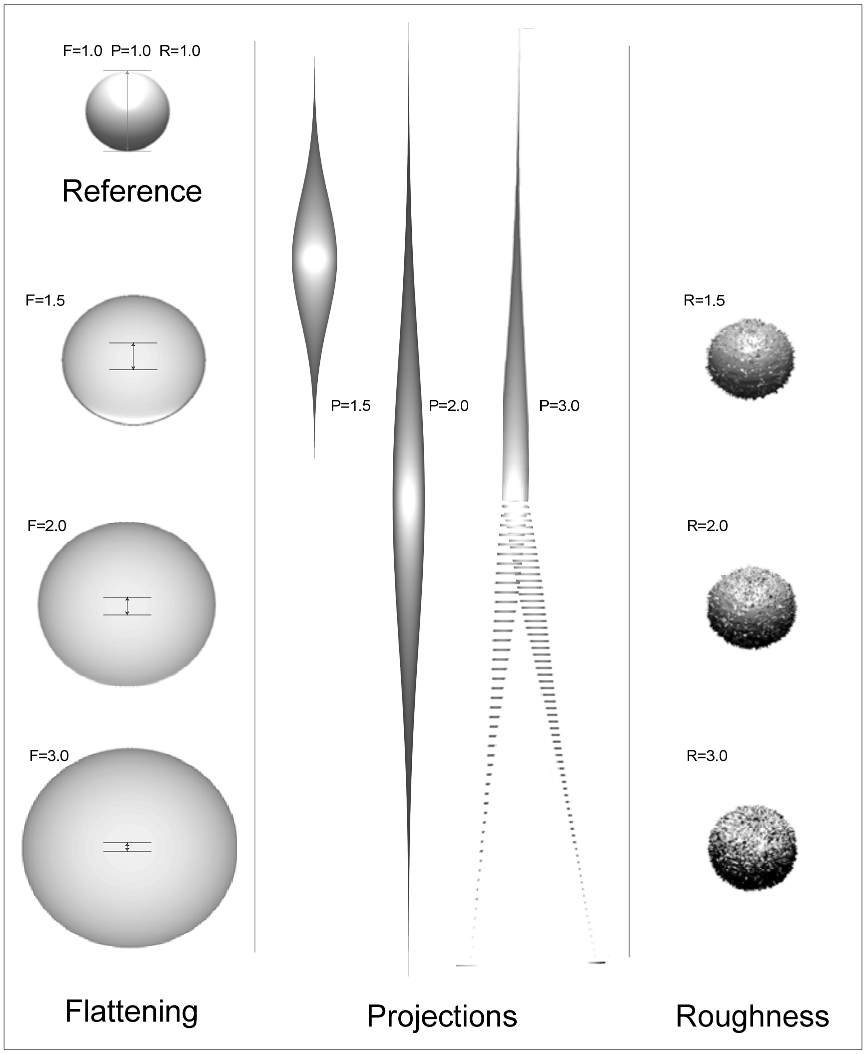

Figure 4.2 Simulated cell surfaces showing how exterior morphological differences can contribute to an increased cell membrane area compared with the smooth reference sphere having identical volume shown at top left. Cells having surface areas 1.5, 2.0 and 3.0 times that of the reference sphere are shown. In the left hand panel, the effect of cell flattening is illustrated using oblate spheroids as models. The circular bodies simulate the appearance of cells viewed from above while the gauge lines show how thick the model cells would be if viewed from the side. In the center panel, cells having dendritic projections are modeled as Gaussian probability curves that have been rotated in space to create solid bodies. Surface areas and volumes can be easily solved explicitly for these shapes. In the right hand panel, cell surface roughness is simulated by adding noise at three scale lengths (0.1 x radius, 0.4 x radius and 1.6 x radius) to represent microvilli, ruffles and folds on the cell surface. These simulations were made in MATLAB using distortions of the sphere function and the surface areas were computed by summing the areas of all facets on the resulting bodies.

4.3 RESULTS AND DISCUSSIONS

The cell density ρ, hydrodynamic deformability parameters Φ and crossover frequency f_o inferred from the elution times measured by DEP-FFF for cancer cell lines in the NCI-60 panel (described in Chapters 2 and 3) are shown in Table 4.1[24, 25, 87] together with the morphological scores for these cells obtained as described above. Although it would have been possible also to prepare slides of each blood cell subpopulation and score those for morphology also, this seemed redundant in view of the beautifully detailed pictures of blood cell subpopulations that are available in the literature (a comprehensive atlas of hematology is available online at http://www.hematologyatlas.com/principalpage.htm). Therefore, blood cell morphological data were scored from those photographs and the blood cell dielectric data were referred to earlier publications from this laboratory showing dielectric data measured by either electrorotation or by DEP crossover frequency methods (DCO).

As concluded in Chapter 3, the DEP crossover frequency is related to the cell membrane folding factor by the expression

$$f_o \approx \sigma_s \cdot \left(\sqrt{2}\ \pi.R.\phi \cdot C_0\right)^{-1}, \tag{4.2}$$

where $C_0 \approx 9$ mF m^{-2} is the capacitance per unit area of smooth lipid bilayer membrane[86] and the folding factor ϕ takes into account cell surface morphology. Given that Chapter 2 shows that DEP-FFF can be used to measure cell crossover frequencies, we can use this expression to deduce the membrane folding factor, cell specific capacitance, and cell total cell membrane capacitance as

$$\phi \approx \sigma_s \left(2^{\frac{1}{2}} \pi R f_o C_0\right)^{-1}, \tag{4.3}$$

$$C_{mem} = \phi C_0 \quad \text{and} \tag{4.4}$$

$$C_{tot} \approx 2^{\frac{3}{2}} \sigma_s R f_o^{-1}. \tag{4.5}$$

The values of C_{mem}, C_{tot}, and ϕ derived using these expressions together with cell radius, R, are also presented in Table 4.1 for the NCI-60 panel and the subpopulations of blood cells. These parameters may be used in conjunction with the morphological data to investigate the relationships between cell dielectric and morphological characteristics. For example, the total cell capacitance is shown plotted against cell radius in Figure 4.3 in the form of a log-log relationship.

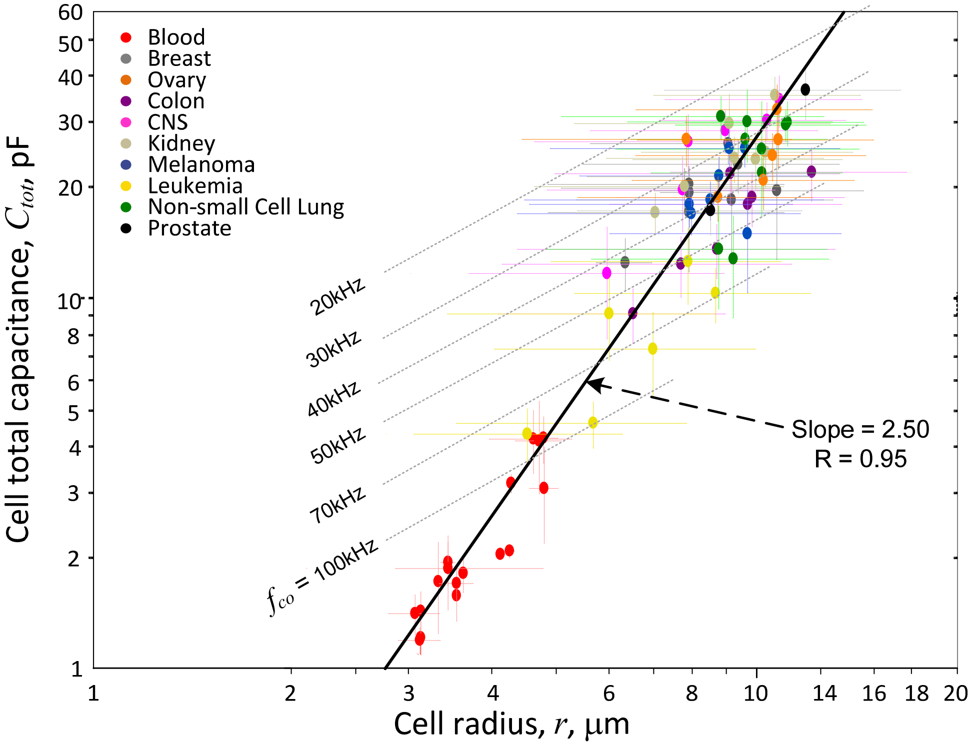

Figure 4.3 Dependency of cell total capacitance on cell radius, R for the NCI-60 and blood cell types.

Three broad clusters comprising the blood cell types (red), the leukemia cell types (yellow), and all other cell types are apparent in Figure 4.3. Furthermore, although considerable scatter is apparent, it is clear from the regression line shown that cell capacitance tends to vary with $R^{2.5}$. This non-integer power is indicative of a fractal relationship[24] between cell surface area (proportional to total capacitance) and cell volume and stands in contrast to the simple R^2 relationship that applies to the surface area of smooth spheres of different radius. The existence of fractal relationships between biological surfaces and volumes is well known because biological processes occurring within the volume of a living body are often dependent on physical phenomena that occur at surfaces. For example, the aveoli in the respiratory system, which are responsible for gas exchange across membrane surfaces into the volume of the body, consist of highly folded surfaces that fill space and exhibit a fractal relationship between area and volume[88]. The inference from Figure 4.3 that the surface area of a cell exceeds that expected from the simple square law relationship with radius has biological significance because it reveals that a long-held paradigm stated in many biological textbooks, which states that cell size is capped by limitations to nutritional and metabolite transport imposed by a membrane area that can only increase as R^2, is incorrect. Rather, it would appear that, mediated by surface folding, cell membrane surface area is a biologically-adjustable parameter. This is further emphasized by the wide range of cell surface areas that are observed for a given cell radius. For example, Figure 4.3 shows that cells having a radius of ~9 μm exhibit capacitances between 10 and 33pF, representing a 3.3-fold range of cell membrane area for a single cell size.

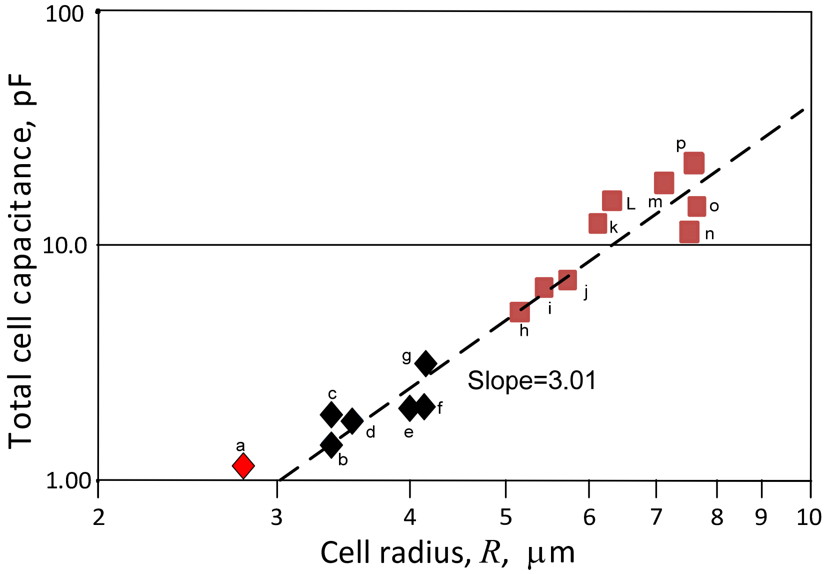

Figure 4.4 Cell membrane total capacitance versus cell radius for cell types previously reported in this laboratory. The cells symbols are keyed to Table 4.2.

As indicated in Chapter 3, DEP crossover frequency values have been reported in the literature for some cell lines that now form part of the NCI-60 panel for which data was obtained by single cell crossover and electrorotation measurements(see Table 4.1). While the DEP crossover frequency results obtained in my DEP-FFF studies were consistent with those prior published crossover frequency results, I felt it was worthwhile to collect together all of the earlier DEP data and test whether non square-law behavior was also apparent. These data are shown plotted in Figure 4.4 and once again, the cell capacitance values follow a power law trend, this time with a slope of 3.01. For those measurements, then, the cell surface area is found to be essentially proportional to volume, again supporting the conclusion that cell size should not be restricted by limitations imposed by cell membrane area.

The data in Figures 4.3 and 4.4 both clearly imply that the cell membrane folding factor increases with cell radius, allowing cell membrane area to increase more rapidly than a square law relationship. Figure 4.5 shows the folding factor, calculated from Equation 4.3, plotted as a function of cell radius.

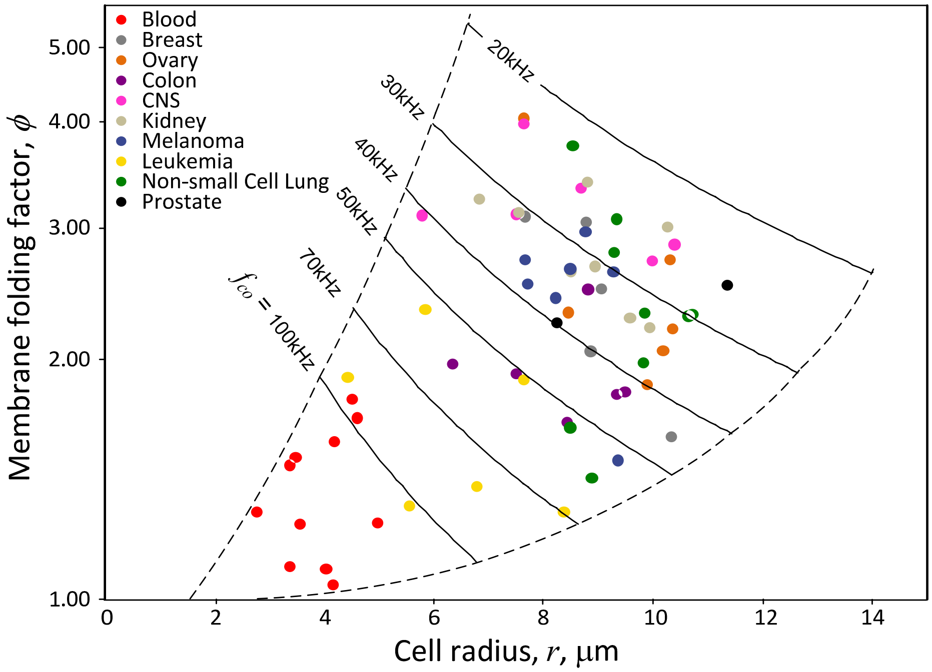

Figure 4.5 Cell capacitance data for the NCI-60 and blood cell types expressed as the dependency of the plasma membrane folding factor on cell radius R. Loci corresponding to constant DEP crossover frequencies based on Equation 4.3 are shown.

This clearly illustrates that membrane folding does tend to increase with cell radius, and demonstrates that the DEP crossover frequency, which determines the behavior of cells in DEP-FFF separation, is determined not by cell radius alone but by an inherent cell membrane-folding phenomenon. Figure 4.5 also provides another visualization of how membrane area has a broad range for a given cell size (see dashed upper and lower bounds), emphasizing that cell radius is not the sole determinant of cell membrane surface area. The figure also shows that blood cells tend to cluster in a region of small folding factors while tissues that are associated with solid organs have much larger folding factors. This suggests that cell structure-function relationships underlie the observed differences in folding factors, giving rise to the idea that the morphology of the cell at its site of origin might underlie the DEP crossover frequency phenomenon observed once the cells are suspended.

We can gain insights into such a relationship by considering a cell that is embedded at its growth site and has a morphology that is compatible with its local environment. In general, a cell that is part of a tissue will have a complicated shape that conforms to the cells to which it is attached, and have some membrane area A and some volume V that are consistent with that disposition rather than with the properties of a sphere.

If that cell is released from its tissue of origin either by harvest or by detachment during migration, it will lose the anchorages that helped maintain its local conformation with other cells at the growth site and the resiliency of its internal cytoskeleton will then tend to pull inwards and cause the cell to round up into a sphere as it enters free suspension. Assuming the cell remains intact during this release process, the membrane and the interior volume of the cell will be conserved. Therefore, we can calculate the radius the cell will assume as it rounds up into a spherical form as

$$R = \left(\frac{3V}{4\pi} \right)^{\frac{1}{3}}. \tag{4.6}$$

The membrane area A that previously conformed to neighboring cells will have to be accommodated on the surface of the newly rounded cell and, consequently, it will need to wrinkle and assume a membrane folding factor given by

$$\phi = A/\left(4\pi \cdot R^2\right). \tag{4.7}$$

Combining these expressions, we obtain an expression for the folding factor in suspension that arises from the area and volume of the cell at its site of origin

$$\phi = \left(3 \cdot \sqrt{4\pi} \cdot V\right)^{-\frac{2}{3}} \cdot A. \tag{4.8}$$

By combining this with expression 4.2 for crossover frequency, we can then write

$$f_o \approx \left(\frac{12\sqrt{2}}{\pi}\right)^{\frac{1}{3}} \frac{\sigma_s}{C_0} \cdot \frac{V^{\frac{1}{3}}}{A} \quad . \tag{4.9}$$

This provides a completely new perspective on the DEP crossover frequency behavior of cells in suspension. While previous studies had revealed that the crossover frequency for suspended cells is inversely proportional to their total cell surface area, which could be correlated with membrane-rich features on the cell surface such as microvilli, ruffles and folds, that earlier work gave no clues as to the origin of that morphology. Equations 4.8 and 4.9, on the other hand, relate these surface features of the cells in suspension to their prior history before they entered suspension. The primary assumption of this relationship is that cell volume and plasma membrane area are conserved during cell release.

Equation 4.9 shows also that the crossover frequency of a cell can be expressed in terms of a single morphological length $R_M = \frac{A}{V^{\frac{1}{3}}}$ parameter, . This is the radius of a perfectly smooth hypothetical cell that would have the same crossover frequency as the "wrinkled" cell under consideration.

The morphological analysis and DEP crossover frequency data for the NCI-60 panel of cell types and blood cell subpopulations gives us the opportunity to test these relationships. First, to confirm that cell plasma membrane and the cytoplasmic content was indeed conserved during harvest, MDA-MB-231 cells in culture were stained with CellMask orange fluorescent plasma membrane stain (C10045, Molecular Probes, Life Technologies) and green-fluorescent calcein-AM viable cell stain (L-3224, Molecular Probes, Life Technologies). These stains allowed both the cell membrane and the cytoplasm to be observed under fluorescent microscopy. When trypsin was added, the cell margins of cells in contact retracted from one another and the cells rounded up as they then detached from the culture flask. Nevertheless, their plasma membranes relaxed onto the rounding cell bodies without fragmentation or loss and the cytoplasmic fluorescence was maintained without any apparent leakage from the cell bodies. These observations suggested that cell membrane area and cell volume were conserved during the release of MDA-MB-231 cells from contact with their neighbors to which they had conformed during growth.

It follows that, for each cell type, the cell membrane folding factor ϕ after harvest should exhibit a correlation with the M score that quantified its membrane-impacting morphology prior to harvest. Figure 4.6 reveals that these parameters do indeed correlate. Considering the dependency that had to be placed on human perception for obtaining these morphological data and also the assignment of a single value of M to each of the cell lines despite the heterogeneity in morphology exhibited by some of them, this correlation is very strong. It shows clearly that the DEP properties of cells in suspension depend on not only the radius of the cells but also their exterior morphology at their growth site of origin.

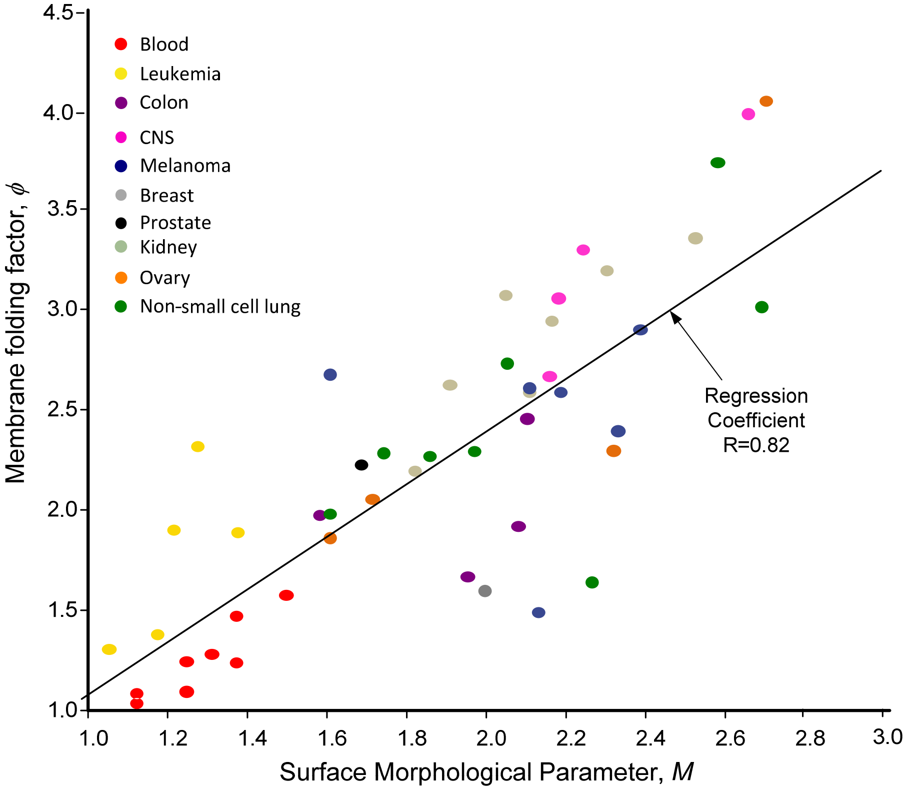

Figure 4.6 Cell plasma membrane folding factor ϕ for the NCI-60 and blood cell types plotted as a function of the corresponding membrane morphology factor M.

Figures 4.5 and 4.6 reveal differences between cell types of different origins. First, the subpopulations of peripheral blood cells are in the G0 resting phase of the growth cycle and are adapted for transportation in free suspension through the circulatory system in nutrient-rich plasma through capillary vessels of small size. Morphological characteristics including small size and relatively small membrane folding factors are compatible with these functions. Consequently, the peripheral blood cell subpopulations (red circles) are grouped closest to the origins of Figures 4.5 and 4.6 and the corresponding DEP crossover frequencies are over 100 kHz at the suspending conductivity of 30 m S m^{-1}.

Second, leukemia cells (yellow circles) are also adapted to travelling through small capillaries in suspension in the high-nutrient plasma. However, leukemia cells are likely not to be in G0 of the cell division cycle and instead exhibit less compact nuclear and internal structures. This gives rise to larger cell size and slightly more complex surface morphologies than normal blood cells. These features cause them to exhibit slightly lower crossover frequencies compared with the normal peripheral blood cells in Figures 4.5 and 4.6.

Finally, solid cancer cell types interact with their neighboring cells and have a surface morphology that is adapted to spreading and contact. The membrane areas for these cell types reflects the variety of cell morphologies in their native tissues and tumor types, ranging from highly transformed to almost normally differentiated tissues. Accordingly, Figures 4.5 and 4.6 show that the cell lines from solid cancers exhibit a much wider range of morphological complexities than is apparent for the normal blood cell subpopulations and leukemia cell types. The larger size and greater membrane folding factor of the solid cancer cell types lead them to exhibit cell crossover frequencies that are much lower than those of the blood cell subpopulations and leukemias.

These results are also significant because it has been suggested by Terstappen (the inventor of the CellSearch method for CTC isolation by antibodies[6, 8, 89]) that DEP approaches are of little value because they merely reflect cell size. My results clearly show that while cell size is one parameter that contributes to cell crossover frequency, exterior morphology of the cell membrane is highly important. For instances, leukemia exhibits a cell total capacitance of 11.7 pF, prostate, ovary and kidney lines near 20 pF, and non-small cell lung, breast and central nervous system cancers near 30 pF in spite of their similar size of 8.7 μm. These dielectric differences are sufficient to isolate these cell types from one another by DEP-FFF despite their similar sizes. This is fundamental for understanding the power of DEP-FFF that can be expected for CTC isolation in comparison to size- and hydrodynamic inertial-filtering of cells[9, 10].

4.3.1 Stability of DEP properties of cancer cells in suspension: Cell cytoplasmic shedding

As shown above, the DEP crossover properties of cells in suspension reflect their characteristics prior to release from their site of origin. A fundamental requirement for this relationship to hold, however, is that the cell membrane area and cell volume are retained during and after the cell release process. My experiments using membrane and cytoplasmic stains showed that this assumption is valid shortly after harvest but it is important to remember that cells that are normally attached enter alien conditions when they remain in suspension. Indeed, normal cell types typically become so stressed when they are removed from their native site that they undergo anoikis[25], programmed cell death analogous to apoptosis[26], triggered by loss of signals from their accustomed environment. Therefore, the study of CTC isolation would be incomplete without some consideration of the how cells from solid tissue behave after they are released from their native growth site and are maintained in free suspension for an extended period.

To examine the behavior of cells that had been grown under adherent conditions and were then placed into suspension for an extended period, I harvested MDA-MB-435 human breast cancer cells by trypsinization and maintained them in a 50 mL centrifuge tube in 10 mL complete media of RPMI+10% FBS for several hours. The tube was kept in the incubator at 37℃ under a 95% air/5% CO_2 atmosphere. Approximately once every 10 minutes, the tube was gently inverted to ensure that the cancer cells remained suspended and gas exchange occurred. This procedure contrasts with those of normal cell passage, where the cells are harvested, collected in a tube, counted and viability tested, and then quickly seeded into a culture flask in a thin layer of medium. In this way, the passaged cells normally settle into contact with a new growth surface within about 15 minutes.

To examine the cells in longer-term suspension, aliquots were withdrawn at times from 15 minutes up to 6 hours following initial harvest. The cells in each aliquot were counted, viability was checked, and they were subjected to cell sizing using a Casey cell counter/sizer. Then a cytospin slide was made and this was Wright-Giemsa stained to allow microscopic examination of the cell properties. DEP-FFF runs were also conducted for cells that had been in suspension for different lengths of time. The appearance of the slides for cells immediately after harvest and two hours later are shown in Figure 4.7.

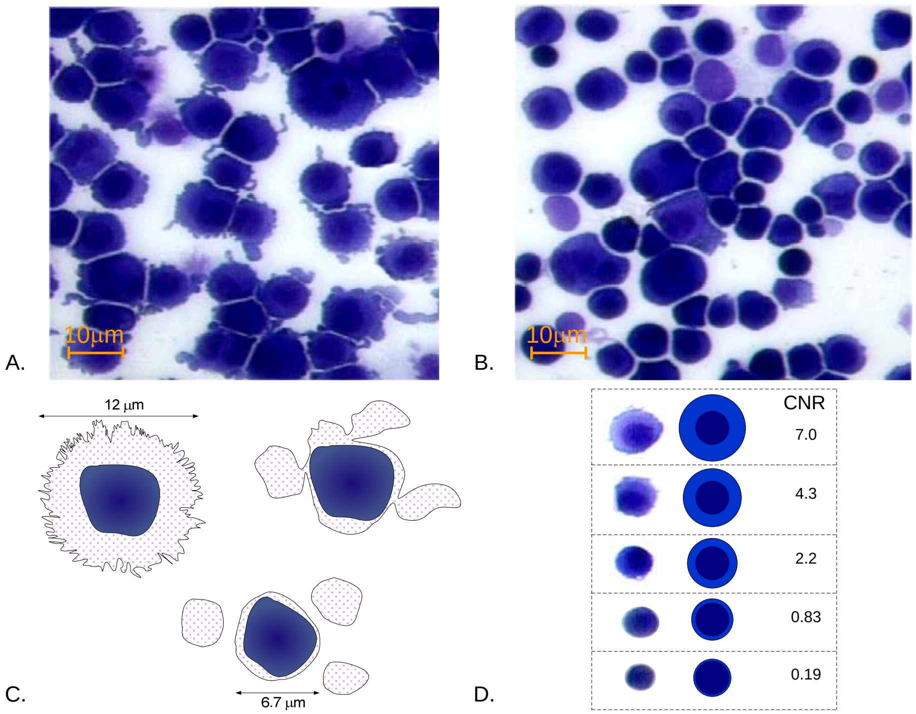

Figure 4.7 (A) Wright-Giemsa stained slide showing the morphology of MDA-MB-435 cells immediately after harvest. Cell peripheries are rich in lamellipodia and blebs and several protrusions of the cytoplasm may be seen detaching. (B) After remaining in a suspension in complete tissue culture medium for 2 h, the morphology of MDA-MB-435 cells shows the effects of continued shedding of cytoplasm. Although most microvesicles are lost during the cytocentrifuge slides-making process, a few may be observed between the cells in this field. (C) The cytoplasmic shedding results in loss of cytoplasm and membrane from the cells. (D) Images of cells illustrating the range of cell morphologies found in MDA-MB-435 suspensions following two hours in suspension. The cytoplasmic to nuclear ratio (CNR) cover wide ranges as they do for circulating tumor cells found in clinical specimens[90].

Lamellipodia and blebs were clearly apparent on the cells stained immediately after harvest but these were seen to reduce in number substantially as time progressed. Only two hours after harvest, the cell surfaces were largely devoid of such features. Remarkably, the diameter of the cells decreased significantly over the same time. Cell nuclei did not alter in size or appearance. From these observations, it was immediately apparent that the cells were undergoing structural modifications as the result of the shedding of cell cytoplasm. The ragged periphery including lamellopodia and blebs of the cells gradually encapsulated cytoplasm into extrusions that closed up and detached from the cell into the suspending medium in the form of vesicles[91] ranging in size from < 1μm to 3 μm in diameter. This process resulted in loss of membrane and cytoplasm from the cells, which become steadily smaller with time as is apparent in Figures 4.7(B) and (C). A few of the forming and of the newly shed cytoplasmic vesicles are visible in the photomicrographs Figure 4.7(A) and (B).

Immediately after harvest, cells exhibited a large cytoplasmic to nuclear ratio (CNR) and good viability (judged by trypan blue dye exclusion). As the shedding process evolved, cells exhibited wider ranges of morphologies and CNRs, as shown in Figure 4.7(D). Significantly, when seeded into new cultures, these cells still showed good regrowth ability despite having shed cytoplasm. Beyond 4 to 6 hours after harvest, however, the continuing progress of cytoplasmic loss and resultant reduction in cell size (see Figure 4.8) led to some cells with such low CNRs that they exhibited very little cytoplasm around their nuclei. These cells were no longer able to grow in culture.

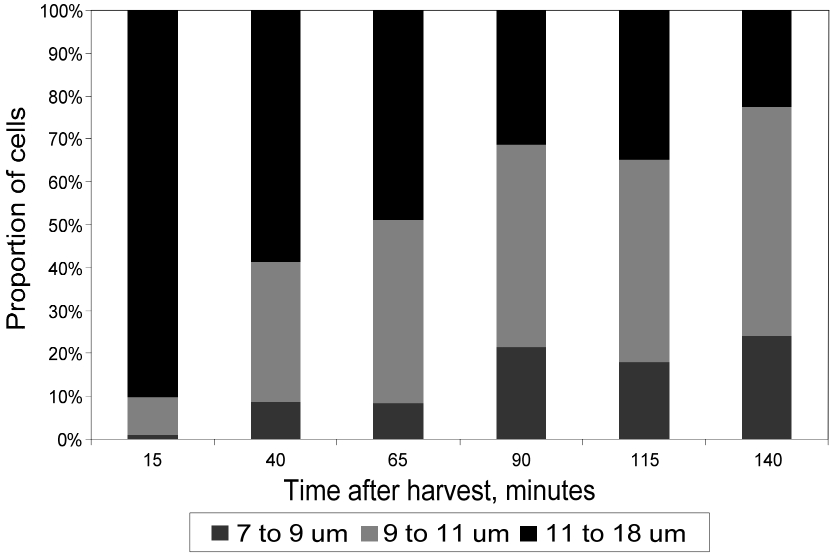

Figure 4.8 Changing distribution of cell radii as a function of time for MDA-MB-435 cells kept in suspension.

During the cytoplasmic shedding process, some cells showed visible characteristics of apoptosis including an ill-defined, blebbing membrane and a diffuse nucleus but most cells did not. Indeed, the fact that most cells could still be cultured even after two hours and a significant loss of membrane and cytoplasm was inconsistent with either apoptosis or anoikis being responsible for the remodeling; neither apoptosis nor anoikis halt once they have been initiated. Therefore, it appeared that I was observing a type of cell remodeling behavior during the first few hours in which the cells were adapting to the stresses of detachment by shedding membrane and cytoplasm without triggering death mechanisms.

To confirm that this cell remodeling was distinct from the death mechanisms I conducted experiments with 10 mM Blebbistatin, which was added to the cell suspension just prior to harvest. This agent acts as an inhibitor of non-muscle myosin (NMM) (which is involved in several membrane biomechanical activities, including the formation of blebs and lamellipodia)[92]. Cytoplasmic loss was almost completely inhibited when Blebbistatin was present. This showed that the cytoplasmic extrusion and pinch off of vesicles that was occurring during cytoplasmic shedding was an active cellular physiological process and that contractile forces mediated by NMM were involved.

Cell suspensions were heterogeneous with respect to cell morphology during the shedding process so that a simple time course experiment by DEP-FFF could not be used to track cell responses as a function of cell size. Fortunately, the PC2400 particle counter used to detect cell elution from the batch mode DEP-FFF instrument allowed cells to be resolved by size. Therefore, it was possible to examine the cell suspensions by DEP-FFF and obtain elution profiles for the MDA-MB-435 cells that were resolved by cell radius. Figure 4.9 shows a log-log plot of cell total capacitance versus cell radius derived in this way for six separate DEP-FFF experiments (blue circles). For comparison, the plot also shows results for other cell lines from Figure 4.4. The particle counter detected MDA-MB-435 cells ranging in radius from 10 to 3 μm radius in the shedding mixture, smaller than most blood cell subpopulations. Of significance is the dependency observed between cell total capacitance and radius. Unlike independent cell types exhibiting a dependency between $R^{2.5}$ and $R^{3.1}$ for different cell types,

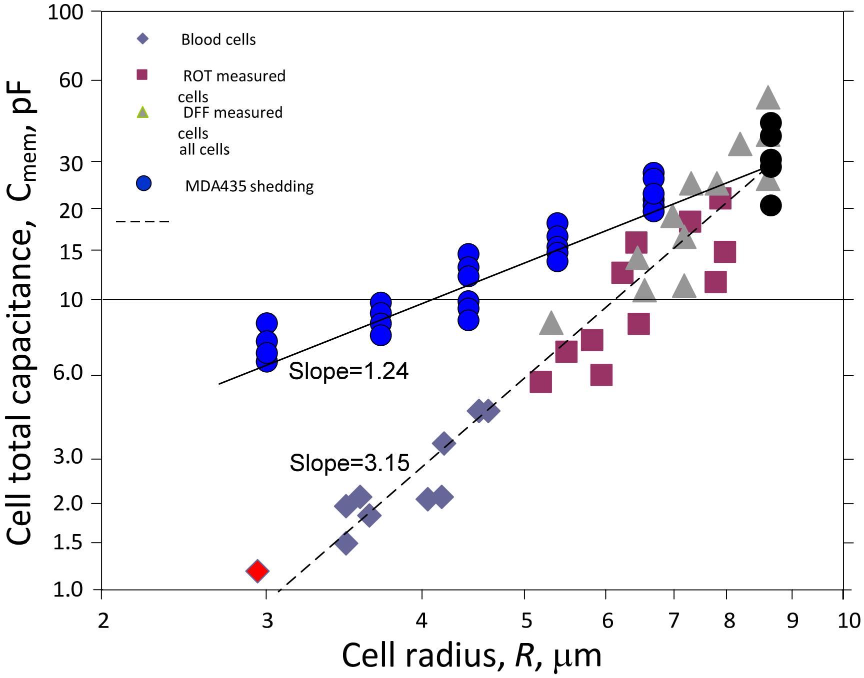

Figure 4.9 Dependency of cell total capacitance on cell radius in a heterogeneous population of shedding MDA-MB-435 cells (blue circles). Other cell types are shown for comparison.

the shedding cells exhibit the dependency $C_{tot} \propto R^{1.24}$. This has profound implications for CTC isolation applications because it means that even if a cancer cell has shed so much membrane and cytoplasm that it has become as small as a blood cell, its membrane capacitance is still so large that it can be easily separated from the normal blood cell subpopulations by DEP-FFF. I repeated these experiments (over 20 times) with MDA-MB-231 and found almost identical results, showing that this behavior was not unique to one type of cancer.

At first, it seemed odd that the cell membrane total capacitance would show such a strikingly different dependency on cell radius than the independent cell types. However, the reason for this difference can again be traced to the prior history of the cell. My results with Blebbistatin showed that the shedding of vesicles was caused by NMM-induced tension in the membrane. Using the same concepts as LaPlace's principle of surface tension in droplets, the tension needed to bring about the formation of a vesicle from the surface of a cell will be proportional to the cell radius and will increase as the cell becomes smaller. This means that the residual membrane area surrounding the cell will tend to be proportional to the cell radius. This relationship will manifest itself in terms of cell dielectric properties as a relationship between total capacitance and cell size of $C_{tot} \propto R^1$. This is very close to the observed dependency upon $R^{1.24}$, lending support to membrane tension-dependent cell cytoplasmic shedding.

4.3.2 Implications for circulating tumor cells

The cell shedding process observed here follows as a cell response to detachment and subsequent maintenance in an environment devoid of surface contact. The resulting heterogeneity in morphologies that arises is termed pleomorphism and it seems highly likely that cancer cells that are shed from tumors and enter suspension in the bloodstream will be prone to a similar process of shedding. Indeed, a remarkable pleomorphism is found by every method that has been used for CTC isolation including CellSearch, microfiltration, flow cytometry, and in my own CTC isolation experiments (see Chapter 5). One example of pleomorphism in a clinical specimen that may be evidence for cancer cell cytoplasmic shedding by cells that have passed from a tumor into free suspension is shown in Figure 4.10 for human serous ovarian cancer (the human specimens used in this experiment were collected under IRB approved protocols and provided to me without patient information or identities. IRB approval protocol number: LAB07-0108, full Title:

To characterize a protein expression and activation signature of human ovarian tumors using reverse phase protein microarray (RPPA) and to correlate this signature with genomic and transcriptional data and patient outcomes, study Chair: Gordon Mills, M.D, University of Texas M.D Anderson Cancer Center). The cancer cells collected from ascitic fluid appear to exhibit analogous pleomorphism to the MDA-MB-435 and -231 lines.

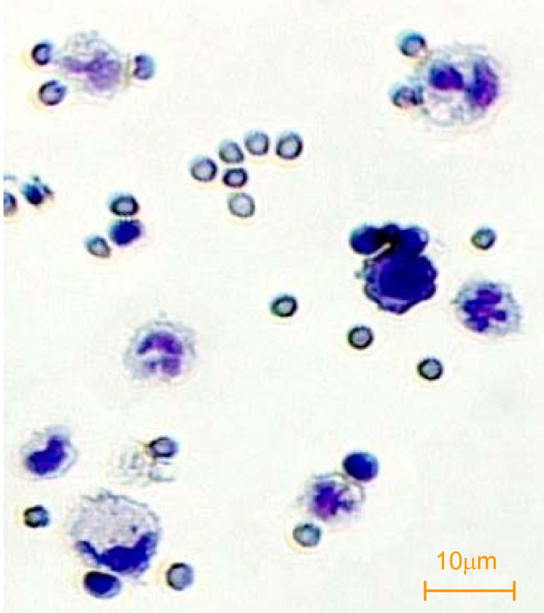

Figure 4.10 Wright-Giemsa stained slide showing human ovarian cancer cells (larger with complex nuclei) obtained from ascitic fluid. The cell peripheries show signs of blebbing and protrusions and a range of morphologies having widely different cytoplasmic to nuclear ratios is evident just as in the case of cultured cells that have stood in suspension for several hours. This suggests that an analogous cytoplasmic shedding process may be occurring in these cells as a result of their entry into free suspension.

The great significance of my finding that cancer cell capacitance remains high even when cancer cells transform into cells having the same size as blood cell subpopulations is that it shows that DEP-FFF should be able to capture even the smallest CTCs similar to PBMNs in size. This is certainly not the case for size-based filtering.

My observations of shedding may also cast light on a puzzling aspect of CTCs, namely how such large cancer cells are able to pass into and through microcapillary beds and also how they are able to embed and form metastases there. The fact that cancer cells can apparently remodel into blood-sized cells without necessarily triggering anoikis or apoptosis is highly significant in this regard. This capability may be a cancer-specific trait because normal cells tend to be prone to anoikis and apoptosis while cancer cells often have defects in the machinery that triggers these responses. Such defects are often cited as mechanisms by which cancer cells resist a variety of environmental challenges, including chemotherapy. My results may suggest that these defects may also play a significant role in permitting the distant dissemination of tumor cells to form metastases.

Finally, my results also suggest that caution is needed in drawing inferences about native tumor cells from circulating tumor cells. Given that CTCs may have undergone the same kind of remodeling observed here for suspended MDA-MB-435 and -231 cells, it is important to recognize that the morphological properties of the CTCs, including their size, membrane area, and also their total cytoplasmic biomolecular content including protein, RNA and μRNAs may be significantly different from their tumor of origin. Nevertheless, with this caution in mind, it is clear that important molecular traits indicative of mutations and genetic tendencies will remain identifiable in the CTCs.

Table 4.1 Dielectric and exterior morphological parameters for the NCI-60 panel and blood cells.

Cell Type	Method	Tissue Type	r, μm			f_{co}, kHz			C_{mem}, mF.m^{-2}			C_{tot}, pF			Folding, ϕ			$M=(F+P+R)/3$
Basophils	*DCO* [31]	Blood	3.58	±	0.03	169	±	18.8	11.2	±	1.3	1.8	±	0.2	1.24	±	0.14	1.38
B-Lymphocytes	*ROT* [49]	Blood	3.29	±	0.03	163	±	45.3	12.6	±	3.5	1.7	±	0.5	1.40	±	0.39	1.25
	DCO [31]		3.09	±	0.22	221	±	17.8	9.9	±	0.8	1.2	±	0.1	1.10	±	0.09	
CD34+ HSC	*ROT* [50]	Blood	3.50	±	0.05	189	±	27.8	10.2	±	1.5	1.6	±	0.2	1.13	±	0.17	1.25
Eosinophils	*DCO* [31]	Blood	4.19	±	0.07	172	±	7.3	9.4	±	0.4	2.1	±	0.1	1.04	±	0.04	1.13
Erythrocytes	*ROT* [51]	Blood	3.10	±	0.02	218	±	21.8	10	±	1.0	1.2	±	0.1	1.11	±	0.11	1.31
	DCO [51]		3.10	±	0.02	185	±	23.5	11.8	±	1.5	1.4	±	0.2	1.31	±	0.17	
	ROT [14]		2.8	±	0.1	268	±	23.8	9	±	0.8	0.9	±	0.1	1.00	±	0.09	
Granulocytes (mixed)	*ROT* [49]	Blood	4.71	±	0.23	130	±	37.9	11	±	3.2	3.1	±	0.9	1.22	±	0.36	
	DFF		4.70	±	0.23	95	±	13.9	15.1	±	2.2	4.2	±	0.6	1.68	±	0.24	
Lymphocytes-mitototic	*ROT*	Blood	4.54	±	0.63	92	±	17.8	16.1	±	3.1	4.2	±	0.8	1.79	±	0.34	1.80
Monocytes	*ROT* [49]	Blood	4.63	±	0.36	95	±	26.8	15.3	±	4.3	4.1	±	1.2	1.70	±	0.48	1.50
	DCO [31]		4.21	±	0.05	113	±	6.4	14.2	±	0.8	3.2	±	0.2	1.58	±	0.09	
Neutrophils	*DCO* [31]	Blood	4.06	±	0.06	170	±	1.2	9.8	±	0.1	2.0	±	0.0	1.09	±	0.01	1.13
T-Lymphocytes	*ROT* [14]	Blood	3.5	±	0.2	176	±	17.6	11	±	1.1	1.7	±	0.2	1.22	±	0.12	1.38
	DCO [31]		3.40	±	0.08	149	±	20.2	13.3	±	1.8	1.9	±	0.3	1.48	±	0.20	
	ROT [33]		3.04	±	0.26	184	±	22.8	12.1	±	1.5	1.4	±	0.2	1.34	±	0.17	
	DFF		3.40	±	1.29	155	±	35.2	12.8	±	2.9	1.9	±	0.4	1.42	±	0.32	
BT-549	*DFF*	Breast	10.36	±	3.53	45	±	15.7	14.4	±	5.0	20	±	6.8	1.6	±	0.56	2.00

Table 4.1 (continued)

HS 578T	*DFF*	Breast	8.88	±	3.63	40.9	±	12.4	18.5	±	5.6	19	±	5.6	2.05	±	0.62	
MCF7	*DFF*	Breast	9.08	±	3.71	33.4	±	5.4	22.2	±	3.6	23	±	3.8	2.46	±	0.40	
MDA-MB-231/ATTC	*ROT* [14]	Breast	6.20	±	0.58	42	±	6.8	25.9	±	4.2	12.5	±	2.0	2.88	±	0.47	
	DFF		7.57	±	2.58	32.3	±	4.4	27.5	±	3.7	20	±	2.7	3.06	±	0.41	
MDA-MB-435	*ROT* [50]	Breast	7.69	±	2.92	38	±	11.8	23	±	7.1	17.1	±	5.3	2.56	±	0.79	
	ROT [14]		7.70	±	0.72	34	±	5.5	26	±	4.2	19.4	±	3.1	2.89	±	0.47	
	DFF		7.69	±	2.92	32	±	3.7	27.3	±	3.2	20	±	2.4	3.03	±	0.35	
NCI/ADR-RES	*DFF*	Breast	8.78	±	3.28	28.4	±	3.4	26.9	±	3.2	26	±	3.1	2.99	±	0.36	
SF-268	*DFF*	CNS	7.53	±	2.77	32.4	±	7.4	27.5	±	6.3	20	±	4.5	3.06	±	0.70	2.18
SF-295	*DFF*	CNS	10.02	±	3.05	28	±	3.2	24	±	2.8	30	±	3.5	2.67	±	0.31	2.16
SF-539	*DFF*	CNS	10.45	±	3.35	25.6	±	4.1	25.2	±	4.0	35	±	5.5	2.8	±	0.44	
SNB-19	*DFF*	CNS	5.83	±	2.83	42.2	±	14.2	27.4	±	9.2	12	±	3.9	3.05	±	1.02	
SNB-75	*DFF*	CNS	8.70	±	3.20	26	±	3.4	29.7	±	3.9	29	±	3.7	3.3	±	0.43	2.24
U251	*DFF*	CNS	7.67	±	3.12	24.5	±	4.5	35.8	±	6.5	27	±	4.9	3.97	±	0.73	2.66
COLO 205	*DFF*	Colon	9.39	±	3.51	44.1	±	7.2	16.3	±	2.7	18	±	3.0	1.81	±	0.30	
HCC-2998	*DFF*	Colon	8.45	±	4.15	52.9	±	8.8	15.1	±	2.5	14	±	2.3	1.67	±	0.28	1.96
HCT-116	*DFF*	Colon	8.84	±	3.97	34.4	±	6.1	22.1	±	3.9	22	±	3.9	2.46	±	0.44	2.11
HCT-15	*DFF*	Colon	7.49	±	3.40	51.6	±	9.7	17.3	±	3.2	12	±	2.3	1.92	±	0.36	2.08
HT-29	*DFF*	Colon	11.66	±	4.43	45	±	7.5	12.9	±	2.2	22	±	3.7	1.43	±	0.24	
KM12	*DFF*	Colon	9.52	±	3.50	43	±	7.1	16.4	±	2.7	19	±	3.1	1.83	±	0.30	
SW-620	*DFF*	Colon	6.36	±	2.33	59.4	±	10.0	17.8	±	3.0	9.1	±	1.5	1.98	±	0.33	1.58
786-0	*DFF*	Kidney	8.97	±	3.16	31.7	±	4.5	23.6	±	3.3	24	±	3.4	2.63	±	0.37	1.91
A498	*DFF*	Kidney	10.29	±	3.46	24.6	±	3.0	26.5	±	3.2	36	±	4.3	2.94	±	0.35	2.17

Table 4.1 (continued)

ACHN	*DFF*	Kidney	7.58	±	3.03	32.1	±	3.8	27.7	±	3.3	20	±	2.4	3.07	±	0.36	2.05
CAKI-1	*DFF*	Kidney	8.82	±	3.60	25.2	±	5.0	30.2	±	6.0	30	±	5.9	3.36	±	0.67	2.53
RXF 393	*DFF*	Kidney	9.97	±	3.43	34.1	±	6.6	19.8	±	3.8	25	±	4.8	2.2	±	0.43	1.82
SN-12C	*DFF*	Kidney	9.64	±	3.28	34	±	5.7	20.4	±	3.4	24	±	4.0	2.26	±	0.38	
TK-10	*DFF*	Kidney	8.51	±	3.06	33.8	±	3.8	23.3	±	2.6	21	±	2.4	2.59	±	0.29	2.11
UO-31	*DFF*	Kidney	6.86	±	1.62	34.1	±	4.4	28.7	±	3.7	17	±	2.2	3.19	±	0.42	2.31
CCRF-CEM	*DFF*	Leukemia	4.45	±	1.69	88.2	±	15.1	17.1	±	2.9	4.3	±	0.7	1.9	±	0.33	1.22
HL-60	*DFF*	Leukemia	8.42	±	3.20	69	±	11.5	11.6	±	1.9	10.3	±	1.7	1.29	±	0.21	
K-562	*DFF*	Leukemia	5.87	±	2.48	54.9	±	13.8	20.9	±	5.2	9.1	±	2.3	2.32	±	0.58	1.28
MOLT-4	*DFF*	Leukemia	5.56	±	2.07	102	±	14.7	11.8	±	1.7	4.6	±	0.7	1.31	±	0.19	1.06
RPMI-8226	*DFF*	Leukemia	7.67	±	2.85	51.5	±	12.0	17	±	4.0	13	±	2.9	1.89	±	0.44	1.38
SR	*DFF*	Leukemia	6.81	±	2.83	79.2	±	20.5	12.5	±	3.2	7.3	±	1.9	1.39	±	0.36	1.18
LOX IMVI	*DFF*	Melanoma	9.38	±	3.49	53.2	±	16.4	13.5	±	4.2	15	±	4.6	1.5	±	0.46	2.13
M14	*DFF*	Melanoma	7.70	±	3.22	36.3	±	4.8	24.1	±	3.2	18	±	2.4	2.68	±	0.35	1.61
MALME-3M	*DFF*	Melanoma	9.29	±	3.39	31	±	3.4	23.3	±	2.5	26	±	2.8	2.59	±	0.28	2.19
SK-MEL-2	*DFF*	Melanoma	8.52	±	3.20	33.6	±	4.2	23.5	±	2.9	22	±	2.7	2.61	±	0.32	2.11
SK-MEL-28	*DFF*	Melanoma	8.82	±	4.01	29.3	±	3.5	26.1	±	3.1	26	±	3.1	2.9	±	0.35	2.39
UACC-257	*DFF*	Melanoma	7.76	±	3.46	38.7	±	4.9	22.5	±	2.8	17	±	2.1	2.5	±	0.31	
UACC-62	*DFF*	Melanoma	8.27	±	3.86	37.8	±	4.5	21.6	±	2.6	19	±	2.2	2.4	±	0.28	2.33
A549/ATCC	*DFF*	NSCL	9.31	±	2.99	29.4	±	3.3	24.6	±	2.7	27	±	3.0	2.73	±	0.30	2.06
EKVX	*DFF*	NSCL	10.74	±	3.15	30.4	±	4.2	20.6	±	2.8	30	±	4.1	2.29	±	0.31	1.74
HOP-62	*DFF*	NSCL	9.84	±	3.84	33	±	11.3	20.7	±	7.1	25	±	8.7	2.29	±	0.78	1.97
HOP-92	*DFF*	NSCL	10.68	±	3.33	30.8	±	3.0	20.5	±	2.0	30	±	2.9	2.27	±	0.22	1.86
NCI-H226	*DFF*	NSCL	8.57	±	3.58	23.4	±	3.1	33.6	±	4.4	31	±	4.1	3.73	±	0.49	2.58

Table 4.1 (continued)

NCI-H23	*DFF*	NSCL	8.94	±	3.41	59.1	±	18.2	12.8	±	3.9	13	±	3.9	1.42	±	0.44	
NCI-H322M	*DFF*	NSCL	9.37	±	3.12	26.5	±	5.9	27.1	±	6.1	30	±	6.7	3.01	±	0.67	2.69
NCI-H460	*DFF*	NSCL	9.85	±	3.08	38.2	±	5.4	17.9	±	2.5	22	±	3.1	1.99	±	0.28	1.61
NCI-H522	*DFF*	NSCL	8.51	±	3.76	53.4	±	16.5	14.8	±	4.6	14	±	4.2	1.64	±	0.51	2.27
IGR-OV1	*DFF*	Ovarian	9.90	±	3.56	40.4	±	6.7	16.8	±	2.8	21	±	3.5	1.86	±	0.31	1.61
OVCAR-3	*DFF*	Ovarian	10.37	±	3.94	27	±	4.5	24.1	±	4.0	33	±	5.4	2.68	±	0.45	
OVCAR-4	*DFF*	Ovarian	10.21	±	3.79	35.6	±	5.2	18.5	±	2.7	24	±	3.6	2.06	±	0.30	1.72
OVCAR-5	*DFF*	Ovarian	8.49	±	3.21	38.3	±	5.3	20.7	±	2.8	19	±	2.6	2.3	±	0.32	2.32
OVCAR-8	*DFF*	Ovarian	7.63	±	3.26	24.1	±	3.7	36.3	±	5.6	27	±	4.2	4.04	±	0.63	2.71
SKOV-3	*DFF*	Ovarian	10.41	±	3.96	33	±	5.5	19.7	±	3.3	27	±	4.5	2.19	±	0.37	
DU-145	*DFF*	Prostate	8.28	±	3.01	40.5	±	5.7	20.1	±	2.8	17	±	2.4	2.23	±	0.31	1.69
PC-3	*DFF*	Prostate	11.42	±	4.34	26	±	4.4	22.4	±	3.7	37	±	6.1	2.49	±	0.42	

Table 4.2 Total capacitance data for cell types plotted in Figure 4.4

†Cell total capacitance values were calculated from literature values of cell crossover frequencies, f_0, or of cited membrane specific capacitances, C_{mem}.

Cell type	**Index in Fig 4.4**	**Radius, R, µm**	$C_{tot}^{\dagger}$, pF	**Reference**
Erythrocytes	a	2.8	1.14	32
B-Lymphocytes	b	3.4	1.44	33,34
T-Lymphocytes	c	3.4	1.93	33,34
Basophils	d	3.58	1.80	33
Neutrophils	e	4.06	2.04	33
Eosinophils	f	4.19	2.07	33
Monocytes	g	4.21	3.17	33,34
DS19 HMBA	h	5.2	5.20	35
DS19 unTX	i	5.5	6.61	35
HL-60	j	5.8	7.17	36
MDA- 231	k	6.2	12.4	14
6M2 non-perm	L	6.4	15. 6	37
MDA- 468	m	7.2	18.5	Unpub
HT-29AS15	n	7.62	11.5	Unpub
HT-29	o	7.75	14.6	Unpub
MDA-435	p	7.7	22.3	This work

CHAPTER 5 CONTINUOUS-FLOW DEP-FFF

5.1 INTRODUCTION

In the previous chapters, it was shown that discrimination between cells by DEP depends on cell dielectric properties that reflect their morphology and membrane surface area[35]. Earlier studies have revealed that unmodified, viable tumor cells can be separated from erythrocytes and peripheral blood mononuclear cells (PBMNs) by DEP[12, 13, 29], and the method has also been shown to have potential for identifying and isolating prostate tumor initiating cells[51], oral cancer cells[52, 53], melanoma[54], and colorectal cancer cells[55]. In Chapter 3, these possibilities were taken still further by showing DEP is applicable to many types of cancers as evidenced by its ability to discriminate between PBMNs and all of the tumor cell types of the NCI-60 panel[93]. In Chapter 4, the biological basis for this surprising broad capacity to discriminate between cancer cells and blood cells was shown to be linked with differences in the morphologies of cancer cells in solid tissues in comparison to the blood cells that normally reside in suspension in the circulatory system. These morphological differences apparently derive from the conformational characteristics of cells at their sites of origin. Taken together, these results suggest that DEP should be widely applicable to isolating CTCs from blood, regardless of the tissue of origin of the tumor cells. Even more surprisingly, the results show that a single set of DEP operating conditions may be applied universally for this purpose of isolating CTCs from blood cells, indicating that neither knowledge of tumor cell type, nor even the knowledge that a specimen comes from someone with cancer, is a prerequisite for CTC isolation by DEP. Finally, even though I found that cancer cells that were released into suspension appear to undergo significant changes in their morphology over a period of a few hours through a process of cytoplasmic shedding, these changes do not compromise the ability of DEP to isolate those cells from blood.

To put these findings into practical use in DEP-FFF isolation, it is worthy of note that this laboratory laid the groundwork for DEP-based isolation of cancer cells from blood in early experiments that showed the differential trapping of tumor versus normal cells on small microelectrode arrays[12, 13]. Nevertheless, that approach offered limited cell discrimination and very low throughput capacity. To overcome those drawbacks, the method of DEP-FFF[94-97] was developed to allow larger batches of cells to be processed with higher discrimination. Batch-mode DEP-FFF was shown to achieve 90% efficient isolation of cultured breast cancer cells spiked into PBMNs[95] and was also able to remove breast tumor cells from $CD34^+$ hemopoietic stem cells with high efficiency[98]. While batch mode DEP-FFF is able to achieve good cell discrimination and proved to be ideal for characterizing cells in Chapters 3 using the analytical approaches developed in Chapter 2, the size of the cell batches that can be processed by this method is still limited to around 2×10^6 cells[95]. Because CTCs are present at concentrations as low as 1 $cell.mL^{-1}$ in the peripheral blood, the minimum specimen volume considered acceptable for CTC analysis is 7 to 10 mL, a volume that contains ~ $4x10^7$ PBMNs. To process this many cells for CTC isolation would require 20 batch-mode DEP-FFF runs, each taking about 15 minutes, and this limitation makes the batch mode DEP-FFF technique impractical for use in routine clinical applications. In this chapter, I show how this throughput limitation may be removed through the development of continuous flow DEP-FFF technology that is capable of processing ~6x10^7 PBMNs per hour.

5.2 CONTINUOUS-FLOW DEP-FFF CELL ISOLATION STRATEGY

As shown in Chapter 1, to achieve discrimination between different cell types by DEP-FFF, cells must be suspended in a low conductivity medium of physiological osmolarity. This low conductivity suspending medium allows both positive and negative DEP forces to be exploited. In addition, the electric current needed to energize the large microelectrode array that provides DEP forces is proportional to the conductivity of the suspending medium in the DEP-FFF chamber. Use of a low conductivity medium reduces the current requirement and lowers the Joule heating in the cell suspension medium, which depends on the square of the DEP microelectrode current. For these reasons, it is desirable to lower the ionic conductivity of cell specimens prior to DEP analysis. Reduction of the ionic concentration, however, leads to a concomitant reduction in the osmotic strength of the cell suspending medium and this needs to be compensated by the addition of a non-ionic osmolyte so that the cells do not become osmotically stressed. In batch-mode DEP-FFF, ion depletion and osmotic compensation are accomplished by mixing a small volume of cells at high concentration with a larger volume of sucrose buffer immediately prior to injecting the cells into the chamber and then allowing them time to settle to the chamber floor before DEP-FFF analysis begins.

Unfortunately, the approach of pre-suspending the specimen in a low ionic strength buffer with compensated osmolarity is not suitable for continuous flow DEP-FFF operations. Mammalian cells exhibit changes in their dielectric properties as a result of ionic leakage from the cytoplasm when they are suspended in low conductivity medium for more than 10^3 seconds[95]. This is not a problem in batch-mode DEP-FFF where the cells are suspended in the eluate immediately before DEP processing begins and the whole process is completed in less than 10^3 seconds. In continuous flow DEP-FFF, however, the goal is to process a large specimen gradually using a continuous injection approach that takes up to an hour. Suspension of the whole specimen in low conductivity medium prior to starting this slow injection process is not feasible if the dielectric properties of the cells are to remain unchanged and cell discrimination is to remain consistent throughout the process. Furthermore, to achieve the target throughput in the continuous-flow regime, it is not feasible to allow the cells to settle for 8 minutes after they have been injected into the separation chamber before instigating the DEP-FFF isolation procedure.

To solve these problems, I developed the continuous flow DEP-FFF approach shown in Figure 5.1. In this scheme, a low conductivity, aqueous sucrose solution having physiological osmolarity acts as the eluate in a continuous flow from an inlet port (a) to an outlet port (f), establishing a Poisseuille flow profile in the separation channel of 200 mm length, 25 mm width and 314 μm height. In the Injection Zone (b), the specimen, comprising a cell suspension in physiological medium, is fed through a slot in the bottom of the chamber at a continuous flow rate q_{in}, which is much lower than the eluate flow rate Q_{in}. Because $Q_{in} >> q_{in,}$ the specimen forms a very thin flow lamina (only about 25 μm thick) that travels along the chamber floor under the 290 μm thick flow lamina of the eluate. As the thin specimen lamina travels in the Ion-diffusion Region, the cells are subjected to sedimentation and weak hydrodynamic lift forces and settle at equilibrium heights close to the chamber floor (see Figure 5.1(c)). The sedimentation rate of cells in the DEP eluate buffer is between 3 and 15 $\mu m.s^{-1}$, depending on cell size and density, so that the maximum time taken for cells to settle down in the 25 µm specimen lamina is about 8 seconds, solving the cell settling problem.

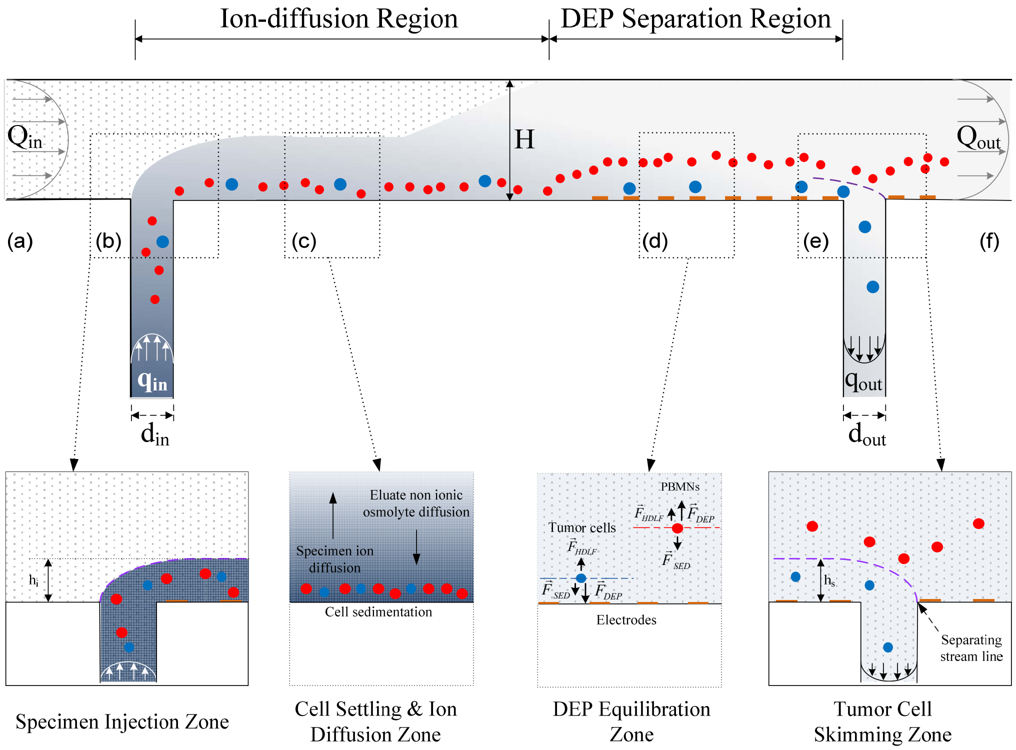

Figure 5.1 DEP-FFF isolation of tumor cells from PBMNs in a continuous-flow chamber viewed from the side. The principles of specimen injection, cell settling and specimen deionization, height equilibration by force balance and isolation of the tumor cells from PBMNs by skimming are described in the text. The relative vertical scale of the extremely thin chamber is exaggerated by ~120-fold compared to the horizontal scale to clarity the operational characteristics.

Meanwhile, ions will diffuse from the thin specimen lamina into the eluate flow stream above it and, simultaneously, the sucrose will counter-diffuse from the eluate flow stream into the thin specimen lamina. As a result, the high conductivity of the specimen lamina is reduced by ion depletion while the osmolarity in the vicinity of the cells is maintained at a physiological level by the compensating influx of sucrose. After flowing a sufficient distance L_{mix} along the chamber for these diffusion effects to reach equilibrium (see calculations later), the ion and sucrose concentrations, and the resultant electrical conductivity and osmolarity, become independent of height in the chamber and the specimen conditions become suitable for DEP separation to be undertaken.

The flow then enters the DEP Separation Region, where microelectrodes on the chamber floor are energized by an appropriate AC voltage to impose DEP forces on the cells. The DEP frequency is chosen so that tumor cells are pulled towards the chamber floor by positive DEP forces as they flow over the microelectrodes while PBMNs are repelled and levitated by negative DEP forces. Cells will move to equilibrium heights at which the DEP, sedimentation and hydrodynamic lift forces balance just as in the batch-mode DEP-FFF process detailed in Chapters 1 and 2 (see Figure 5.1(d)). Finally, as the flow enters the Tumor Cell Skimming Zone (e), fluid is withdrawn through a slot in the chamber floor at a rate q_{out}, skimming off a thin lamina of fluid from the bottom of the chamber up to a height h_s. Tumor cells, which have reached equilibrium heights close to the chamber floor, are thereby captured through the withdrawal slot while PBMNs, which reached equilibrium heights above the skim height h_s, are carried over the slot and exit to waste along with the main eluate Q_{out} at (f). The detailed design and operation of these stages will be described in more detail in the sections that follow.

5.2.1 Continuous injection and skimming

As indicated in the strategy, the aim in the continuous flow DEP-FFF method is to transport the specimen along the floor of the separation chamber in a thin lamina that flows beneath the main eluate stream. For the parabolic Poiseuille flow velocity profile, the thickness of this specimen lamina, h_{in}, above the chamber floor is related to the injection flow rate, q_{in}, and the eluate inlet rate Q_{in} according to the expression

$$Q_{in} / (Q_{in} + q_{in}) = 3(h_{in} / H)^2 - 2(h_{in} / H)^3 , \qquad (5.1)$$

where H is the height of the chamber. For a very thin specimen lamina, $q_{in} << Q_{in}$, and

$$h_{in} \approx H(q_{in} / 3Q_{in})^{1/2} . \qquad (5.2)$$

Analogously, at the withdrawal port, a thin lamina of fluid may be skimmed from the chamber floor up to a height h_s by withdrawing fluid at a rate q_{out}, where

$$h_s \approx H(q_{out} / 3Q_{out})^{1/2} . \qquad (5.3)$$

In practice, q_{in} and q_{out} are very small and cell sedimentation can result in imperfect injection and skimming behavior if there are either vortices or positions of low flow rate at the injection or withdrawal slots. In order to optimize the slot design, I simulated flow profiles for various chamber heights, slot widths and flow rates using

COMSOL Multiphysics software (Stockholm, Sweden) assuming that the fluid was incompressible and had a density of 1036 kg.m^{-3} and a dynamic viscosity of 1.31 x 10^{-3} Pa.s, reflecting the properties of the eluate medium used for my cell isolation experiments. The results for the withdrawal slot simulations are shown in Figure 5.2. The behavior at the inlet slot region is a mirror image of that at the withdrawal slot.

Desirable skimming behavior was observed when the slot width d_{out} was small compared with the chamber height H (Figure 5.2 (a)). In this case, a well defined separation region at the slot opening cleanly split the thin lamina of height h_s at the chamber bottom from the main chamber flow. Streamlines above the skim height h_s travelled essentially horizontally across the slot and no regions of low flow rate or significant vortices were generated in the separation region. In this case, tumor cells close to the chamber floor would be skimmed cleanly into the withdrawal slot, while PBMNs in the fluid above the skim height would be rapidly carried over the slot without being thrown into the slot by inertial forces or having the opportunity to sediment into the slot from regions of low flow rate.

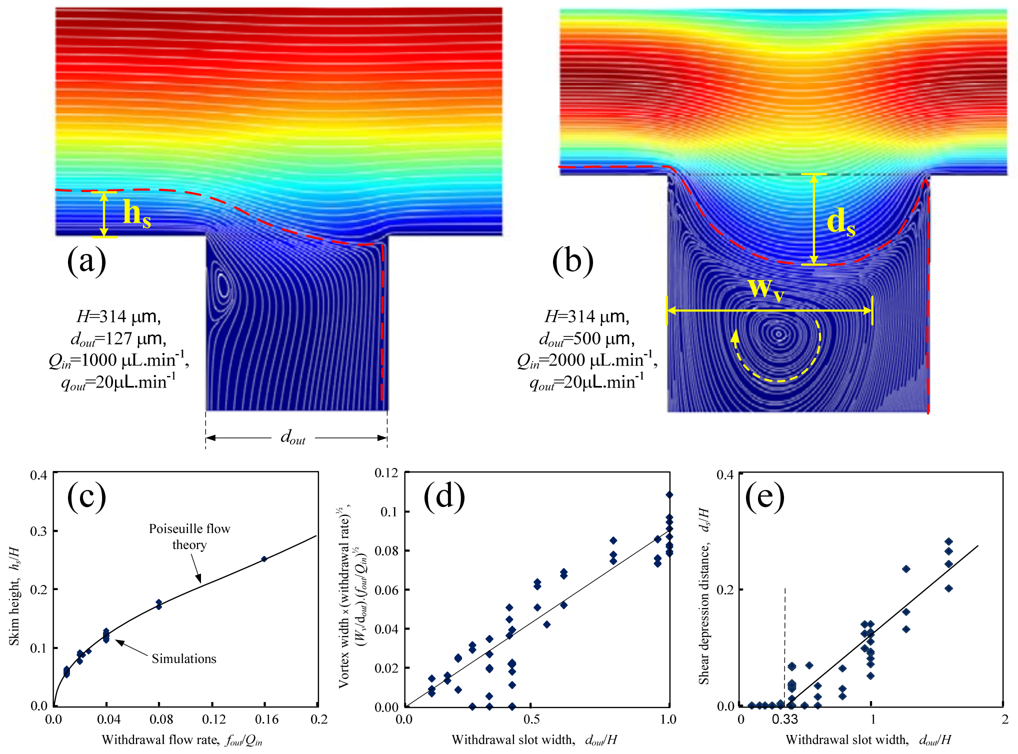

Figure 5.2 COMSOL Multiphysics simulations of the fluid flow behavior at the DEP-FFF chamber withdrawal slot for different geometries and flow rates. (a) When the withdrawal slot width dout is small compared with the chamber height H, optimum skimming behavior is observed with negligible vortices or regions of low flow rate; (b) as the relative withdrawal slot width is increased, a vortex forms within the slot, streamlines from the main channel are depressed into the slot region, and zones of low flow rate appear; (c) the skimming height hs accurately follows that predicted by simple Poiseuille flow theory (see text). Vorticity (d) and depression of the streamlines from the main channel (e) increase with increasing slot width.

As the withdrawal slot width d_{out} was increased, the separation behavior became less ideal (Figure 5. 2 (b)). Although the skim height h_s still followed the Poiseuille model (equations above), the flow in the slot opening became more complex. Streamlines above the skim height h_s travelled downwards into the mouth of the slot causing a depression by a distance d_s of the region where the withdrawal and main chamber flow streams split. Furthermore, a vortex of diameter W_v formed in the withdrawal tube and significant regions of low flow rate were generated in the separation region. In this case, tumor cells close to the chamber floor would be skimmed into the withdrawal slot but then potentially recirculated in the vortex. Because of the curvature of the streamlines, some may be thrown by inertial forces into the depressed streamlines of the main chamber flow, carried back into the main chamber, and lost to waste. Meanwhile, PBMNs traveling above the skim height that followed the depressed streamlines from the main channel into the chamber mouth would not only have a tendency to be thrown into the withdrawal flow by the curvature of the streamlines but also would need to be carried uphill from their depressed locations well down inside the mouth of the withdrawal slot back into the main chamber against the sedimentation forces acting on them. As a result of these effects, some PBMNs would enter the withdrawal stream and contaminate the tumor cell fraction.

My simulations established criteria for designing efficient withdrawal slots and they showed, in particular, that a withdrawal slot of width $d_{out} < H/3$, regardless of the flow rate, exhibits negligible depression of the main chamber streamlines into the mouth of the withdrawal port (Figure 5.2 (e)) as well as providing low vorticity (Figure 5.2 (d)). Exactly analogous principles apply to the injection slot design if the potential for cell accumulation in the mouth of the injection slot is to be reduced. In my experiments, I used a chamber height of 314 μm and injection and withdrawal slot widths of 127 μm, corresponding to the flow conditions shown in Figue 5.2 (a). At the inlet, the specimen was injected at a rate of q_{in}=25 μL.min^{-1} with a main eluate flow rate Q_{in}=1000 μL.min^{-1}, leading to a specimen lamina thickness h_{in}=29.3 μm at the inlet. At the outlet, the withdrawal rate was q_{out}=20 μL.min^{-1} leading to a skimming height of h_s=26.4 μm. In my experiments, the injection and withdrawal flows were provided by 1 mL syringes driven by digital syringe pumps (KDS210, KD Scientific, Holliston, Massachusetts) and the eluate flow was provided by a precision gear pump (Ismatec, Glattbrugg, Switzerland).

The concept of combining and splitting lamina flow streams in a microfluidic channel is the basis of the so-called H filter design in which two inlet ports enter from opposite sides at one end of the chamber to combine lamina flows and two withdrawal ports exit from opposite sides at the other end of the chamber to split lamina flows[99]. In cell separation applications, sedimentation of cells is a significant problem at low flow rates and the channels and tubing that carry the cells into and out of the separation chamber should be oriented vertically to avoid cell loss resulting from settling and adherence to tubing surfaces. In the H-filter design[99], regions of stagnant flow can occur at both ends of the chamber at the interfaces of the flow streams. At the low flow velocities required for isolation of tumor cells, sedimentation of PBMNs would occur in the slow-moving region of fluid heading towards the top withdrawal port in the H-filter configuration and some PBMNs would inevitably fall into the lower withdrawal port and contaminate the tumor cell isolate. For these reasons, I adopted the π configuration for my continuous flow DEP-FFF chamber, thereby eliminating stagnant flow in the fluid interface regions and greatly reducing the possibility of contamination. In my design, tumor cells flow directly downward through the withdrawal slot in the chamber floor while PBMNs travel horizontally. Furthermore, microelectrodes are positioned on the chamber floor on both the upstream the downstream sides of the withdrawal slot in my design. These electrodes continue to levitate PBMNs by DEP forces in the slot region and on the far side of the slot. This helps reduce still further the likelihood PBMNs will fall into the withdrawal slot and contaminate the tumor cell isolate. In these ways, my chosen π configuration improves significantly upon the H-filter design concept for applications involving sedimentary particles such as cells.

5.2.3 Deionization and osmotic compensation

In order to pull tumor cells towards the microelectrodes on the floor of the separation chamber by positive DEP while simultaneously repelling PBMNs high into the eluate flow stream by negative DEP, as required by the continuous-flow DEP-FFF cell isolation strategy, the cell suspending medium conductivity must be much lower than the cell cytoplasmic conductivity[100]. After collection, my specimens were in physiological medium containing approximately 150 mM NaCl and having a conductivity of 1.4 S.m^{-1}. This suspending medium conductivity was approximately the same as that of the cell cytoplasms, and needed to be lowered to a target value of about 60 mS.m^{-1} before the cells could be subjected to DEP separation. This reduction in conductivity was accomplished by using diffusion to deplete the ions in the specimen as it moved through the Cell Settling and Ion Diffusion Zone shown in Figure 5.1 (c). The length of the Ion Diffusion Zone was chosen in accordance with the chamber height H and flow rate Q_{in} to insure that ions had sufficient time to diffuse throughout the chamber height before the sample entered the DEP zone. The required mixing length L_{mix} for a diffusible species to approach equilibrium has been analyzed for the H-filter microfluidic configuration[101] and, by analogy for my π configuration device, may be written as

$$L_{mix} \approx H(Q_{in} + q_{in})/(WD), \tag{5.4}$$

where W is the width of the chamber in the direction perpendicular to the plane of Figure 1 and D is the diffusion coefficient of the diffusing species.

My cell specimens contained between 20 x 10^6 and 40 x 10^6 PBMNs (along with trace levels of tumor cells) collected from whole blood by centrifugation over Histopaque 1077 (Cat 10771-100mL, Sigma-Aldrich, St Louis, USA) and were suspended in 1 mL RPMI medium that had been adjusted to a density of 1036 $kg.m^{-3}$ by adding iodixanol (Optiprep^{TM} Density Medium D1556, Sigma-Aldrich, St Louis) to a concentration of 11%[95]. I used the same eluate recipe as in earlier DEP-FFF studies[24, 95] and the work in Chapters 2-4. This was composed of an aqueous solution of 9.5% sucrose (S7903, Sigma-Aldich, St Louis, MO), 0.1 mg mL^{-1} dextrose (S73418-1, Fisher, Fair Lawn, NJ), 0.1% pluronic F68 (P1300, Sigma-Aldich, St Louis, MO), 0.1% bovine serum albumin (A7906, Sigma-Aldich, St Louis, MO), 1 mM phosphate buffer pH 7.0, 0.1 mM CaAcetate, 0.5 mM MgAcetate and 100 units mL^{-1} catalase (C30, SigmaAldich, St Louis, MO). This mixture was adjusted to a conductivity of 30 mS m^{-1} with KCl. As before, in this mixture Pluronic F-68 provided mechanical stabilization of cell membranes under flow conditions[102], catalase protected cells from reactive oxygen intermediates[103], and bovine serum albumin inhibited cell adhesion to tubing and chamber surfaces. The specimen and eluate densities were both 1036 $kg.m^{-3}$, as a result of their iodixanol and sucrose contents, respectively, and this parity of densities was chosen to avoid the possibility of convection mixing occurring when the specimen and eluate flow streams were combined in the continuous flow chamber.

After the specimen was injected into the chamber, the Na^+, K^+ and Cl^- ions that dominated its high conductivity diffused into the eluate. Sucrose counter diffused from the eluate to maintain the osmolarity of the cells at a physiological level so they were not osmotically stressed, which would have impacted cell size and membrane dielectric characteristics[24].

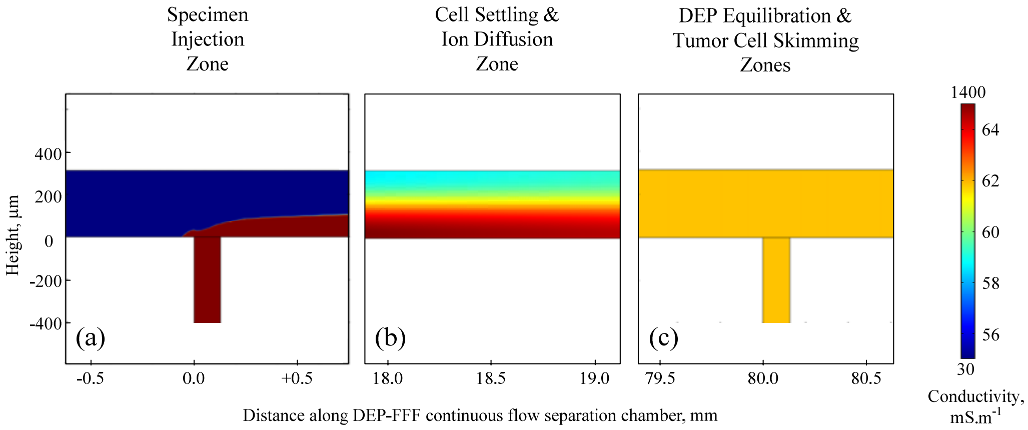

Figure 5.3 COMSOL-multiphysics simulations of the conductivity distribution in the flow stream (a) at the specimen injection zone, (b) at the midpoint of the cell settling and ion diffusion zone, and (c) at the cell skimming zone.

To investigate the diffusion process and select flow rates that were slow enough for them to approach equilibrium throughout the height of the DEP-FFF chamber, I simulated the diffusion of ions and sucrose in the continuous flow device using COMSOL Multiphysics software. The results for the conductivity distributions in key zones of the chamber are shown in Figure 5.3. In the specimen injection zone (Figure 5.3 (a)), a very large conductivity gradient exists where the specimen stream (1400 mS.m^{-1}) first joins the main eluate flow (30 mS.m^{-1}). At a distance 18 mm downstream from the specimen inlet, in the cell settling and ion diffusion zone (Figure 5.3 (b)), the ion conductivity is clearly spreading upwards through the chamber. By the time the flow reaches the DEP equilibration zone 40mm downstream from the specimen inlet and the tumor cell skimming zone 80mm downstream from the specimen inlet (Figure 5.3 (c)), ion diffusion is essentially complete and the conductivity is homogeneous throughout the chamber height at about 61.5 mS. m^{-1}. I showed, similarly, that sucrose diffusion is also completed before the specimen reaches the DEP equilibration zone.

To verify these simulation results, I measured the AC current drawn by the microelectrode array. This depends much more sensitively on the conductivity of the medium immediately adjacent to the microelectrode than on the conductivity higher in the chamber. I found that the microelectrode current was the same under continuous specimen injection conditions as when the chamber was filled with a homogeneous medium having a conductivity of 61.5 mS.m^{-1} (the equilibrium conductivity for the flow steams in the DEP-FFF chamber). This showed that diffusion was complete and the ion concentration had reached equilibrium. I also conducted an experiment in which fluid leaving the ion diffusion region was skimmed from the chamber floor up to different heights by altering the withdrawal flow rate. The conductivity of the withdrawn fluid was 61.5 mS.m^{-1} regardless of the skim height, again showing that diffusion was complete.

This method of reducing the conductivity during flow through the ion diffusion zone insured that all cells were subjected to exposure to low conductivity conditions for the same, relatively short, period of time regardless of when they entered the chamber during the 40 minute specimen processing time. Passage of cells through this zone took about 180 seconds. This afforded sufficient time for the cells to sediment to equilibrium positions close to the chamber floor so that they entered the DEP equilibration zone at identical heights and all were subjected to similar electric field conditions. Altogether, depending on their type cells spent between 220 and 600 seconds in the DEP-FFF chamber from injection to withdrawal, well below the 1000 seconds at which dielectric alterations due to exposure to low ionic strength media become apparent.

5.2.4 DEP-FFF microelectrode stage

The frequency and magnitude of the electrical signal applied to the microelectrodes in the DEP equilibration zone (Figure 5.1 (d)) were chosen so that the tumor cells were pulled towards the chamber floor while the PBMNs were repelled high above it. In Chapter 3, the crossover frequencies of all cell types derived from solid tumors in the widely representative NCI-60 panel of cancers were shown to lie far below those of all the subpopulations of peripheral blood cells. By choosing a DEP signal frequency that was between the crossover frequencies of tumor cells and the PBMNs, it was possible to impose differential DEP forces to drive cell separation and allow the tumor cells to be isolated by skimming them from the chamber floor. At the target equilibrium eluate conductivity of 60 $mS.m^{-1}$ used for my continuous flow DEP-FFF tumor cell isolation experiments, the crossover frequencies f_o of all solid tumor cell types were well below 100 kHz while those of all the blood cell subpopulations were above 200 kHz. A DEP signal frequency of 130 kHz was chosen, therefore, for my tumor cell isolation experiments. (Recall that the crossover frequency is proportional to the cell medium suspension conductivity (Equation 1.11), so that the f_o values measured by batch mode DEP-FFF at 30 $mS.m^{-1}$ in the prior chapters expected to be half the corresponding f_o values at the 60 $mS.m^{-1}$ target conductivity value used for my continuous flow DEP-FFF isolations).

The DEP force imposed on the cells depends on the square of the applied voltage V (Equation 1.1), suggesting it might be advantageous to use a high DEP voltage to increase the height differential between tumor and PBMNs leaving the DEP equilibration zone[93]. However, the electric field that gives rise to the DEP force also induces a transmembrane potential difference in the cells that can stress them and cause them to become leaky towards ions and/or electroporated. This could alter their DEP properties and confound their separation characteristics. The magnitude of the induced transmembrane potential difference depends upon the electric field strength, the cell diameter and the applied electric field frequency[103]. Because of their larger diameter and closer proximity to the microelectrodes during continuous DEP-FFF isolation, tumor cells are more prone than PBMNs to damage by high voltage in DEP-FFF cell isolation experiments. However, I found that I could use an applied voltage of 4V p-p in the experiments to provide strong DEP forces without evidence of diminished tumor cell isolation efficiency. Catalase was included in my eluate buffer as in my previous work[24, 95] to protect the cells from a low concentration of reactive oxygen intermediates that may be produced by electrochemical processes at the microelectrodes[103].

To confirm the differential height distributions of tumor cells and PBMNs under conditions chosen for continuous flow DEP-FFF, I ran a batch-mode DEP-FFF experiment and recorded the time-dependent elution profile of a mixture of PBMNs from healthy donors and MDA-MB-231 human breast cancer cells. As in Chapter 2, the cell elution times were mapped to the cell equilibrium height distribution in the chamber, which is shown in Figure 5.4. It may be seen that the MDA-MB-231 cells traveled through the DEP-FFF chamber between 5 and 13 μm above the chamber floor while the PBMNs were transported at between 14 and >40 μm height.

In Figure 5.4, the batch mode DEP-FFF chamber had a microelectrode array area of 7500 mm^2 and the power output capacity of the signal generator limited the maximum DEP voltage that could be applied to it to 2.8 V p-p. In my continuous flow DEP-FFF design, however, I shortened the microelectrode array to only one third the length of the batch mode chamber. This shorter array drew only 1/3 of the DEP current and permitted me to use a higher DEP operating voltage of 4 V p-p. Under these conditions, the levitation height for PBMNs was > 27 µm. Accordingly, I chose a skimming height of h_s=26 µm by setting the withdrawal rate to q_{out}=20 µL.min^{-1} for continuous flow DEP-FFF cell isolation experiments (as in Figure 5.2(a)). In this case, the specimen injection and outlet withdrawal rates were the same.

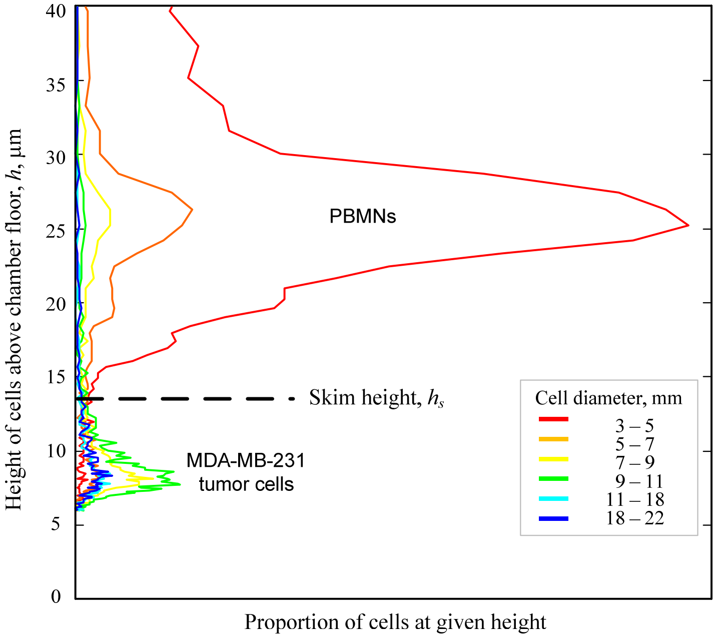

Figure 5.4 Height distributions of MDA-MB-231 human breast cancer cells and PBMNs in batch mode DEP-FFF separation. The height distribution was mapped from the cell elution times assuming that the transit velocities of the cells reflected their heights in the Poiseuille hydrodynamic flow profile inside the DEP-FFF chamber.

5.3 TESTS AND CLINICAL RESULTS

The final design of my continuous flow DEP-FFF device used for cell spiking tests and CTC isolation employed a chamber 160 mm long with a width of 25 mm, a height of 314 μm, and an inlet to outlet slot spacing of 90 mm. The chamber floor was lined by a microelectrode array based on the design detailed earlier[104] in which parallel gold-on-copper microelectrodes of 50 μm width and spacing were patterned on a kaptan substrate. However, only the last 45 mm of the microelectrode array leading up to the outlet slot was energized. The DEP and flow conditions were as described in the optimized simulations in the earlier figures with eluate flow rate= 2000 $\mu L.min^{-1}$, specimen injection flow rate=20 $\mu L.min^{-1}$ and CTC skimming flow rate= 20 $\mu L.min^{-1}$. A continuous sinusoidal DEP signal of 130 kHz at 4 V_{p-p} was employed, and the conductivity of the emerging eluate was 64 $mS.m^{-1}$.

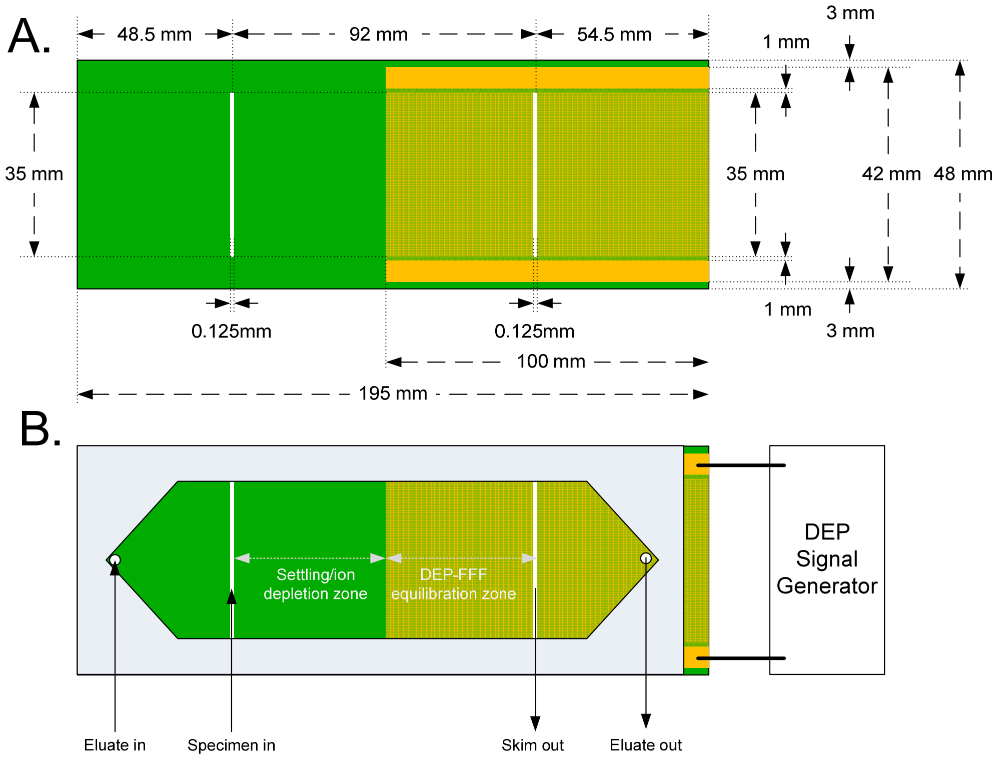

Figure 5.5 (A) Chamber floor of the final continuous flow DEP-FFF design showing the laser cut inlet and outlet slots for injecting the specimen and skimming off the cancer cells and the DEP microelectrode array with dimensions. (B) The continuous flow DEP-FFF isolator with the chamber top in place.

I ran tests of the continuous flow DEP-FFF isolator design using MDA-MB-435, MDA-MB-231 and other cultured tumor cells spiked into PBMNs from healthy donors to compare with my earlier batch-mode DEP-FFF experiments[95]. During these tests, the chamber was mounted on the stage of a Mitotoyo long working distance microscope so that the injection and skimming behavior of the cells could be observed. Recovery rates of 70% to 80% were found for the cancer cells. Unfortunately, the laser cut slots were imperfect and it was apparent that the injection and skimming flows were not consistent over the entire widths of the slots. These imperfections seemed to arise because the slot edges were slightly irregular. In addition, the electrode substrate of 35 µm thick Kapton, which was glued down with double sided adhesive tape to form a carpet on the floor of the chamber was not perfectly flat. These two issues clearly perturbed the flow patterns in the chamber and resulted in variations of injection and skimming heights across the slots. This could clearly be observed to lower the efficiency of the DEP-FFF recovery of the cancer cells spiked into PBMNs because these cancer cells could be seen to consistently "jump the gap" in some parts of the withdrawal slot. It is not clear by how much this lowered the collection efficiency of the continuous DEP-FFF but it seems reasonable to speculate that a chamber with improved physical characteristics might approach the 90% efficiency level reported earlier for cancer cell recovery from PBMNs by batch mode DEP-FFF. These chamber problems are being addressed by having a new microelectrode electrode with precision laser-cut slots fabricated commercially on 150 µm thick substrate that should lie flat in the chamber.

Even with these shortcomings, my measurements confirmed that tumor cell isolation efficiencies of 70- 80% were achieved consistently and independently of the cell spiking density. To illustrate this, MDA-MB-435 cells were prelabeled with fluorescent dye (CellTracker Green CMFDA, Life Technologies, Grand Island, New York) and spiked into PBMNs from 10 mL blood specimens at concentrations ranging from 50 to 600 per mL. The output port of the DEP-FFF chamber was connected to a modified flow cytometer[98] so that labeled tumor cells could be gated and counted by their fluorescence (Ex 488 nm, Em 517 nm) as they emerged and discriminated from contaminating blood cells. Figure 5.6 shows the cytometric scatter plots obtained at three different spiking concentrations. Even with the imperfections in the DEP-FFF chamber floor already noted, the average collection efficiency was found to be 75% and independent of spiking density. Given that the concentration of cells in these isolation experiments is well below that at which cell-cell interactions would be expected to affect separation behavior in continuous flow DEP-FFF, this independence of performance on spiking density was not surprising.

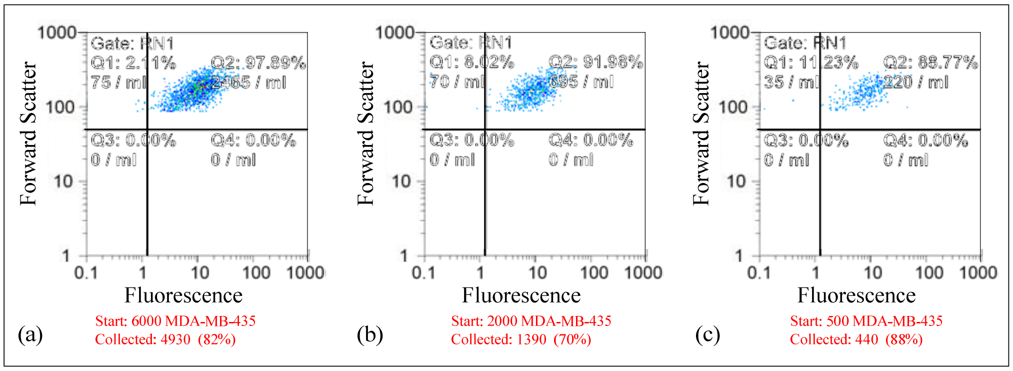

Start: 6000 MDA-MB-435
Collected: 4930 (82%)

Start: 2000 MDA-MB-435
Collected: 1390 (70%)

Start: 500 MDA-MB-435
Collected: 440 (88%)

Figure 5.6 Flow cytometric (FACS) scattergrams showing the recovery of tumor cells from PBMNs spiked with (a) 6000, (b) 2000 and (c) 500 MDA-MB-435 cultured cells prelabeled with CellTracker Green fluorescent dye.

Despite these encouraging results using spiked samples, I was made aware by Dr. Apostolia Tsimberidou, who provided me with clinical specimens (see later), that the dielectric properties of the blood of cancer patients might be modified by their disease and treatment regimen, compared with the blood of healthy donors. For example, leukocytosis, thrombocytosis and increased acute phase protein levels in the blood are typically part of a chronic systemic inflammatory response to late stage malignancy[105]. These factors have the potential to lead to anomalous blood cell subpopulations that might contaminate CTCs during DEP-FFF isolation. Therefore, I conducted a preliminary trial using twenty clinical specimens from late stage cancer patients to establish whether CTCs could be isolated from blood under realistic clinical conditions. Peripheral blood specimens were obtained as part of the Initiative for Molecular Profiling in Advanced Cancer Therapy (IMPACT) Trial at The University of Texas M.D. Anderson Cancer Center with informed patient consent and the approval of Institutional Biosafety Committee. Specimens of at least 7 mL volume were collected from patients in 10 mL BD purple cap (EDTA) vacutainers and processed within 3 hours. The PBMNs, putatively containing CTCs, were separated from the patient specimens over Histopaque 1077 and subjected to continuous DEP-FFF also using same settings as for the spiked PBMN specimens. In this case, the isolate from the withdrawal slot was collected in a 1 mL syringe for each specimen over the approximately 40 minute processing period.

The FACS approach was not feasible for analyzing CTCs isolated from clinical specimens because the 10 mL blood specimens may have contained as few as ten, and very rarely more than hundreds of, CTCs. Downstream immunostaining of the collected cells followed by subsequent FACS analysis would not have allowed such small cell populations accurately. Therefore, a Cytopro^{TM} instrument (Wescor Model 7620, Logan, Utah) was used to mount the cells from the clinical blood isolates onto two microscope slides. One slide was immunostained for cytokeratin using FITC-conjugated CK3-6H5 antibodies (Miltenyi Biotec, Bergisch Gladbach, Germany) combined with nuclear staining by DAPI (D1306 Molecular Probes, Eugene, Oregon). An example of a slide stained this way is shown in Figure 5.7, where putative CTCs show green fluorescence due to the presence of cytokeratin and both CTC and PBMN nuclei exhibit blue fluorescence. The slide is suggested to show putative CTCs, since most blood cells do not express cytokeratin.

Although it is common practice in the literature to assume that the cells which express cytokeratin that are isolated from the peripheral blood of cancer patients are CTCs, irrefutable validation of their tumor origin requires that they are demonstrated to carry the same genetic lesions that are characteristic of the patient's primary tumor. Fortunately, the primary tumors of all patients enrolled in the IMPACT trial (the human specimens used in this experiment were collected under IRB approved protocols and provided to me without patient information or identities. IRB approval protocol number: LAB07-0817, full Title: Blood, Bone Marrow and Tissue Collection for Patients with Advanced Malignancies seen in the Clinical Center for Targeted Therapies, study Chair: Apostolia M. Tsimberidou, M.D. University of Texas M.D Anderson Cancer Center) are subjected to screening for somatic mutations. In order to verify the presence of CTCs in my isolates, definitively, the unstained slides were therefore given for molecular analysis to Dr. Katherine Stemke Hale of the Kleberg Center for Molecular Pathways at M.D. Anderson. DNA was extracted from the slides using PicoPure (cat 11815-00, Applied Biosystems) then further cleaned with a QIAamp DNA Micro Kit (cat 56304, Qiagen).

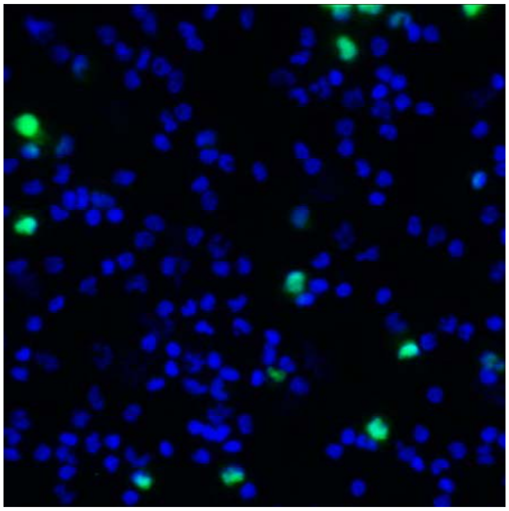

Figure 5.7 Circulating tumor cells collected by continuous flow DEP-FFF from the peripheral blood of a patient with colon cancer. The green fluorescence reveals staining of cytokeratin in the tumor cells by FITC-conjugated CK3-6H5 antibodies. PBMNs show only blue fluorescence due to DAPI staining of their nuclei.

The DNA was preamplified using the following primers:

Forward: ATGACTGAATATAAACTTGTGGTAGTTGGA
Reverse: GAATTAGCTGTATCGTCAAGGCACT
Vic Reporter: CTTGCCTACGCCACCAG
FAM Reporter: CTTGCCTACGTCACCAG

The Taqman Pre-Amp Master Mix (Cat 4391128) was employed according to the protocol specified by Fluidigm. Sample from my slides, together with a positive and a negative control, were tested using a Fluidigm 48.48 Genotyping Array (cat BMK-M-48.48GT, Fluidigm) according to Fluidigm's protocol. For the colon cancer specimen shown in Figure 5.7, the somatic mutation in the primary tumor was KRAS G13D. MDA-MB-231 was used as a positive control for this because it possesses the same mutation. The slide specimen exhibited a positive result with a signal intensity that indicated approximately 10% of the cells on the slide had the KRAS G13D mutation, mirroring the proportion of cells that stained positively for cytokeratin in Figure 5.7. This not only verified that sufficient CTCs were present on the slide to identify the cancer-causing gene but also shows that the continuous flow DEP-FFF method coupled with molecular analysis may be suitable for clinical screening purposes.

CHAPTER 6 CONCLUSIONS AND FUTURE PERSPECTIVES

This dissertation describes the work I undertook to test the hypothesis that DEP-FFF principles could be adapted to a continuous-flow regime that would allow 10 mL clinical specimens to be processed in less than 60 minutes and thereby provide a universal and reliable detection method for CTCs that was independent of cancer type and surface markers. A number of steps were needed to accomplish this involving both biophysical and engineering challenges. The biophysical aspects involved establishing whether cell dielectric properties, which earlier work had found to reflect the state of cell transformation, would enable the isolation of cancer cells from the subpopulations of peripheral blood cells not just in special cases but generally for all cancers. To achieve this, it was important not only to examine a wide variety of tumor cell types and compare their properties to those of blood cells but also to attempt to understand the biological basis for any observed differences.

Prior work in the characterization of cell dielectric properties had relied on single cell dielectric crossover and electrorotation techniques. In these methods, the dielectric properties are examined one cell at a time, taking several minutes per cell. Although the dielectric properties of a number of cell lines have been reported using these methods, they are so tedious that most publications reported measurements on only 10 to 20 individual cells of each type. The resulting data provided estimates of the statistical distributions of the different cell types but there was insufficient data to be able to infer whether cell subpopulations were present. I considered this data insufficient and the tedious approached inadequate to undertake a robust study of cell dielectric properties in the context of designing a reliable cell isolator for CTCs. Therefore, in Chapter 2, I developed a profiling technique that allowed cell density, deformability and DEP crossover frequency to be inferred from DEP-FFF elution profiles. These new profiling techniques allowed me to undertake measurements on the entire NCI-60 panel of cells types as well as on many other cell lines that were available to me. Data was obtained for an unprecedented number of cells types with unprecedented detail. Thus, I showed in Chapter 3 that all of the NCI-60 cell types had DEP crossover frequencies that allowed them to be discriminated from blood cells. Furthermore, the statistical distributions of the DEP crossover frequencies of all of the cell types that had been derived from solid tumors in the NCI-60 panel were widely separated from those of the cell types in peripheral blood, showing that DEP-FFF should be able to isolate the cancer cells from blood with high efficiency. Leukemia–derived cell types also had significantly different DEP crossover frequencies from the blood subpopulations but the statistical distributions were not widely separated, showing that DEP-FFF is suited for concentrating leukemia cells from blood but not for isolating them into pure fractions. The discovery that all of the solid tumor types in the NCI-60 panel, spanning the clinical diversity of 9 organ types, had such different DEP properties from blood cells lent support to the concept that DEP-FFF isolation might be very broadly applicable to different cancer types. Furthermore, the result that the DEP-FFF isolation was "blind" to differences in cell surface receptors and ligands confirmed the advantages of DEP-FFF over antibody-based methods which have the prerequisite that target cells possess specific antigens. My results, therefore, confirmed that DEP-FFF is an antigen-independent cell isolation methodology. Nevertheless, to demonstrate that DEP should be applicable to all cancers, I felt it was important to understand the biological basis for the DEP crossover frequency differences and to show that these were general for cancer.

The diversity of cell types in the NCI-60 panel allowed me to examine correlations between cell characteristics and DEP properties in Chapter 4. Given that prior work had established that DEP crossover frequencies depended on cell membrane morphology, I focused on factors that could lead to differences in membrane morphology when cells were released from their growth sites into suspension. Although previous work had shown that DEP properties and cell membrane morphologies were linked, it had not sought to understand the reasons for the differences in membrane morphology of cells in suspension. By observing that cells growing in juxtaposition had a morphology adapted to cell-cell contact and adhesion, I realized that cells in tissue have surface area to volume characteristics that are quite different from those in free suspension. By proposing that cell membrane area and volume were conserved when cells detached from their growth site, I was able to derive formal relationships between the morphology of a cell prior to detachment, its membrane morphology after detachment, and its DEP crossover frequency properties in suspension. I showed that a morphological parameter for the growing cells correlated well with cell DEP crossover results in suspension. It seems to be reasonable to conclude from these results that CTCs released into suspension from any type of solid tumor should have characteristics that allow them to be captured from blood by DEP-FFF. Nevertheless, this morphology argument should apply to all cells that are released from solid tissue into the blood circulation, whether they are cancerous or not. Thus, cells collected from peripheral blood by DEP-FFF cannot necessarily be assumed to be cancer cells. Nevertheless, this is no different from other CTC collection methods. For example, while it is often assumed in the literature that EpCam$^+$/Cytokeratin$^+$/CD45$^-$ cells detected by the CellSearch method are CTCs, this may not be true. It is quite likely that normal cells are shed into the peripheral blood as the result of non-cancerous pathologies, even if these are rare. It follows that some type of verification is always required as an adjunct to cell isolation to verify that putatative CTCs are of tumor origin.

In Chapter 4, the membrane area of cells was also shown to bear a fractal relationship to cell radius. This demonstrates that conventional wisdom that cell size is limited by cell membrane area according to a square-law radius relationship is incorrect. Evidently cell structure-function relationships are more complex than that and the cell molecular apparatus includes the capacity to increase cell membrane area to meet transport needs. Interestingly, after being released from their growth sites and maintained in suspension out of contact with adherent surfaces, the conserved cell volume and membrane area began to adapt by a process of cytoplasmic shedding. This process did not indicate that programmed cell death through anoikis or apoptosis had been initiated, however, because the shedding cells could still be returned to normal adherent culture and grown. Rather, the cytoplasmic shedding appears to be part of a cell remodeling process that involves non muscle myosin (NMM) through active physiological processes. The presence of pleomorphism in the CTC populations captured by a number of isolation methods including CellSearch and high throughput flow cytometry as well as in ovarian cells that I isolated from ascetic fluid suggests that a similar process of cell shedding likely occurs after tumor cells have been released from their primary tumors into the peripheral blood. The shedding process may help explain how CTCs, which are normally thought of as being large, are able to pass through, and create metastases within, fine capillaries in organs, including the brain and the lungs, and in the periphery of the body.

Even though cancer cells shed membrane and cytoplasm over a period of hours when placed in suspension, I showed that the total membrane capacitance of these cells remained significantly higher than that of blood cells, even when the shedding was so extreme that the radius of the cancer cells had fallen to within the range of blood cell radii. This finding is significant because it shows that DEP-FFF can be used to isolate CTCs of all sizes. This distinguishes the method from other antibody-independent CTC isolation techniques including size-based filtering and hydrodynamic inertial filtering for which cell size and consistent flexibility are fundamental parameters underlying the respective isolation phenomena.

It is frequently argued that the behavior of cells grown in culture may not reflect the properties and behavior of cells *in vivo*. This argument seems especially valid when comparing the behavior of cells that have been immortalized and grown in a monolayer culture with normal, mortal cells that are growing within a living organ. In my work, however, most of the cultured cells I used were not immortalized by treatment with virus or other agents and owed their growth capabilities in culture to the oncogenes that led them to be cancers in the patients from whom they were donated when the cell lines were first established. Furthermore, my studies were aimed at understanding the behavior of the tumor cells after they were released from growth sites and placed in suspension, often with blood or PBMNs. These conditions seem to a great extent to mirror the origin of CTCs in peripheral blood. Therefore, while there is still the need for caution and the recognition that my cell models are not the same as clinical specimens, there seems to be a reasonably high likelihood that the behaviors I observed for 60 independent cultured specimens from different origins mimic, at least broadly, the behaviors of real CTCs.

Having understood the parameter requirements for efficiently isolating the wide range of cancer cell types in the NCI-60 panel and discovered the surprising result that a single set of DEP-FFF isolation parameters would be applicable to the isolation of CTCs from any type of solid tumor, I designed and built a continuous-flow DEP-FFF isolator. Chapter 5 describes the technical principles involved in this effort and shows my final working design, which had to solve several engineering challenges. First, the cells in the specimen needed to be maintained in their physiological medium until just prior to DEP-FFF processing at which time their suspending medium conductivity needed to be greatly lowered while their osmolarity was maintained. In addition, the cells needed to be close to the chamber floor by the time they encountered the DEP-FFF microelectrode array. These problems were solved by developing a π-shaped chamber through which a carrier eluate was flowed. Cells were injected through a slot in the chamber floor into a thin lamina that flowed beneath the eluate. Cells in this thin lamina had very little distance to settle to the chamber floor and their conductivity and osmolarity was adjusted by passive diffusion of ions and sucrose across the interface of the specimen lamina and the eluate flow through a process we termed membraneless dialysis. Once the conductivity had been lowered, the CTCs and blood cells were spatially separated by dielectrophoresis. The DEP frequency was chosen so that cancer cells were pulled gently to the microelectrode array on the chamber floor by positive DEP (much less force than was needed to trap them) and the CTCs were repelled 25 μm or more above the chamber floor by strong negative DEP. Cancer cells were then skimmed off by a low flow through an exit slot. Using this design, I demonstrate the isolation of tumor cell spiked into normal peripheral blood with an efficiency of 70-80%. The slot and electrode design showed physical irregularities that clearly impacted the isolation efficiency and it is likely that an efficiency around 90% is achievable because would be consistent with the efficiency observed in small batches of cells by batch-mode DEP-FFF.

I applied the continuous flow DEP-FFF to several clinical specimens and showed that CTCs could be isolated from all of them. In two examples where the CTCs exhibited somatic mutations for which the Kleberg Center for Molecular Pathways was able to conduct analysis of my isolates, the mutations were detected at levels that were consistent with the proportion of cytokeratin-positive cells that visible through immunolabeling. These data showed that my continuous-flow DEP-FFF isolator worked for clinical specimens.

Several areas for further development are clear. First, head-to-head comparison between DEP-FFF and other CTC isolation methods is needed. It appears that with improved electrodes and slots we might achieve 90% isolation efficiency of CTCs. The published CellSearch efficiency data has statistical complications because the authors of the studies insist that the correct way to test a CTC isolation method by spiking experiments is to place 1 CTC into 10 mL blood and then to demonstrate that one can recover that single cell. This approach has no statistical validity. By adding many CTCs to blood, we show that our recovery rate by batch mode DEP-FFF is ~90%. At one conference my approach was criticized by a Johnson and Johnson representative as being inferior to the CellSearch method which could successfully recover a single cell seeded into 10 mL blood. My recovery efficiency suggests that if I did multiple experiments each with 1 cancer cell seeded into blood then I would, on average, recover that single cell on nine out of ten occasions. But as long as clinicians can be swayed by such obfuscation by vendors, there will be a serious problem in comparing technologies in the CTC field.

Another important issue that I did not have time to address was the purity of the CTC specimens I collected. With the DEP-FFF settings I used, several thousand blood cells were captured in the outlet slot together with the cancer cells. These contaminating cells had morphological characteristics that suggested they were approaching the end of their life in the peripheral blood and were dying. If blood cells suffer erosion of their membrane barrier function, as is expected towards the end of their lifetimes, then they would no longer fulfill the criteria for DEP attraction or repulsion delineated in Chapter

1. Instead, they would flow over the DEP-FFF microelectrode without experiencing any significant DEP forces at all. With the chamber configuration I used for continuous flow DEP-FFF, these cells would simply drop down the outlet slot used to skim off the cancer cells and therefore they would end up contaminating the target cells, as I observed. This problem was especially significant in a few of the late-stage patient specimens I examined. As mentioned in Chapter 5, Dr. Tsimberidou warned me that the dielectric properties of blood cells might be modified in late stage cancer patients. Although I found that the majority of the PBMNs in cancer patients behaved in the same way as those from normal blood donors, the PBMNs were highly reactive, tended to be adherent, and the captured cell fractions from these cancer specimens were found to be contaminated with many thousands of blood cells. This suggested that those specimens contained a higher proportion of damaged PBMNs that fell down the outlet slot along with captured CTCs. This apparently serious problem should be easy to solve, however, because very large dielectric differences can be anticipated between captured cancer cells and damaged blood cells. Specifically, this problem should be easily addressable by incorporation of an additional DEP stage at the outlet that would remove the contaminating, damaged blood cells from the target CTCs, leaving the CTCs in a much higher state of purity.

Another aspect worthy of future work are molecular studies of isolated cells. CTCs carry genetic information about the primary tumor and, in addition, possess (as yet unidentified) molecular signatures that are indicative of their metastatic potential. One such genetic trait may be the ability to maintain viability during shedding, as discussed in Chapter 4. Other potentially dangerous traits include their degree of stem characteristics, which is considered to be indicative of the flexibility the CTC will show in adapting to a new site and growing vigorously. In my studies, putative CTCs were pooled from slides for genetic analysis and these tests verified the applicability of DEP-FFF isolation as a front end for molecular analysis. Newer molecular analysis instruments are becoming available that can analyze the molecular profile of single cells on slide. This shows that it should soon be possible to investigate the heterogeneity of molecular profiles of CTCs and this should give additional insights into the danger posed by specific CTCs. These results would be applicable to prognosis and potentially to diagnosis and targeted therapy matching.

During my studies, the DEP-FFF methods were licensed by The University of Texas M.D. Anderson Cancer Center to ApoCell, Inc., and considerable efforts were made to transfer all knowledge to the company to enable the development of a commercial version of the continuous-flow DEP-FFF isolator. These efforts were successful and ApoCell is now commercializing the technology with 10 prototypes. ApoCell sponsored aspects of the research in the lab to aid in this commercialization effort and promised to make my lab a test center for the commercial version. However, once the commercial version was developed, ApoCell refused to follow through with a second phase sponsored research agreement and placed commercial instruments in another lab at MD Anderson and at other cancer centers around the US without telling us. Furthermore, ApoCell reproduced several of the experiments that I conducted in this work and for which I had shared proof of concepts and data. Apocell [106]then published a paper including these findings without telling us or including me or my advisor as authors. M.D. Anderson counsel declined to take action in any of these matters. Fortunately, I have since published three comprehensive articles that go far beyond the work ApoCell could publish to establish that these studies were from our laboratory. Sadly, several lines of studies that ApoCell had suggested and then decided not to support had to be stopped and Mr Tom Anderson, who assisted in the fabrication of all my devices, lost his position

Despite these setbacks, I was able to achieve every aim of my research and largely demonstrate my hypothesis. Its final proof will lay ahead as ApoCell and others attempt to use the concepts introduced here in clinical applications. If the methods become clinically applicable and impact metastatic cancer in the future then I will feel fulfilled in all my efforts.

Appendix A Cell throughput consideration

Jones showed that cells begin to experience dipole-dipole interactions that can affect their DEP behavior when they are less than about 5 diameters apart[44]. To ensure that the DEP-FFF properties are controlled by the intrinsic properties of the cells and are not impacted by such interactions, the cell concentration, "loading concentration", therefore needs to be low enough to achieve adequate separation. In batch mode, the front end of a DEP-FFF chamber of height H is filled with a particle concentration N m^{-3}. After settling into a 2-D layer on the floor of the DEP-FFF chamber, the mean cell spacing will be

$$S = (HN)^{-\frac{1}{2}} \tag{A.1}$$

In order for S to be at least 5 cells diameters, the maximum concentration in the cell mixture must be

$$N_{\max} = \left(25 d_c^2 H\right)^{-1} \tag{A.2}$$

where d_c=cell diameter.

If the cells are of 10 μm diameter then $N \sim 10^6$ cells per mL. further, if the DEP-FFF chamber has a volume of 5 mL and the chamber is filled to 10% of its total length, then a maximum of 5 x 10^5 cells can be processed per batch to satisfy the spacing requirement. If the turnaround time is 15 minutes per batch then this sets the maximum throughput rate at around 2 x 10^6 cells per hour. This is not a problem for analytical applications but it is about 20 times slower than is needed for isolating CTCs from 10 mL clinical specimens.

The same cell spacing criterion applies in continuous flow DEP-FFF but, in this case, the cell suspension is injected only up to a height h, so that the maximum concentration can be

$$N_{\max} = \left(25 d_c^2 h\right)^{-1} \tag{A.3}$$

For a cell injection rate of 25µL.min^{-1}, an eluate flow rate of 1000µL.min^{-1}, and a chamber height H of 580µm, Eqn 5.2 (Chapter 5) shows that the height of the chamber filled with cells h = 53 µm. To achieve a particle spacing of at least 5 diameters, the maximum concentration is $N \sim 7.6 \times 10^6$ cells of 10µm diameter per mL. At the given injection rate, this corresponds to a throughput of 7.6x10^6 cells per minute, or 4.5 x 10^8 cells per hour. This allowed me to process sufficiently 10 mL clinical blood specimens, which contained ~ 4 x 10^7 total PBMNs, in 40 minutes.

Appendix B Analysis of parameter sensitivity

In designing the DEP-FFF instruments for cell analysis and CTC isolation, it is important to specify the accuracy with which the system parameters must be controlled in order to achieve a desired accuracy in cell parameters or efficiency of cell isolation. To achieve this, a sensitivity analysis is required to show how performance parameters depend on system parameters. In this section, the sensitivities are calculated for each operational parameter using the method of differential calculus. The equations for DEP-FFF system operations have been derived in Chapters 1, 2 and 5. For characterizing cells, the cell properties in batch-mode DEP-FFF affect the heights at which they are transported through the chamber, effectively mapping cell physical properties to elution time profiles.

The flow velocity at height h in a chamber of height H and width W for a flow rate Q is given by

$$v(h) = 6v_0 \frac{h}{H}\left(1-\frac{h}{H}\right), \tag{B.1}$$

where $v_0 = \frac{Q}{HW}$. (B.2)

If h is small that approximates to

$$v(h) = 6\frac{Qh}{H^2W}. \tag{B.3}$$

The time taken for a particle at height h to be eluted from a chamber of length L will be

$$T(h) = \frac{L}{v(h)} = \frac{H^2 WL}{6hQ}\,. \tag{B.4}$$

Sensitivity of T versus small changes in H

By differentiation of (A.4), we obtain the expression

$$\partial T = \frac{2HWL}{6hQ}\partial H \tag{B.5}$$

Showing that

$$\frac{\partial T}{T} = 2\frac{\partial H}{H}\,. \tag{B.6}$$

This shows that a 1% change in chamber height will lead to a 2% change in elution time.

Sensitivity of T versus small changes in h

From (B.5)

$$\partial T = -\frac{2HWL}{6h^2 Q}\partial h \tag{B.7}$$

so that

$$\frac{\partial T}{T} = -\frac{\partial h}{h} \tag{B.8}$$

This shows that a 1% change in particle height will lead to a 1% change in elution time.

Sensitivity of T versus small changes in W

From (A.5)

$$\partial T = \frac{H^2 L}{6hQ}\partial W \tag{B.9}$$

so that

$$\frac{\partial T}{T} = \frac{\partial W}{W} \tag{B.10}$$

This shows that a 1% change in chamber width will lead to a 1% change in elution time.

Sensitivity of T versus small changes in applied voltage V

At low frequencies, cells are levitated and the hydrodynamic lift force can be ignored\

$$F_{DEP} + F_{SED} = 0 \tag{B.11}$$

This can be expressed as

$$\pi R^3 \Delta\rho g = 2\pi\varepsilon R^3 \operatorname{Re}(f_{CM})P(f)q(h)V^2 \qquad \text{(B.12)}$$

where

$$q(h) = \exp\left(-{h}/{h_0}\right). \qquad \text{(B.13)}$$

Combining (A.12) and (A.13), we obtain

$$\frac{\Delta\rho g}{2\varepsilon \operatorname{Re}(f_{CM})P(f)V^2} = \exp\left(-{h}/{h_0}\right) \quad . \qquad \text{(B.14)}$$

Taking natural logarithms and differentiating gives us

$$\partial h = 2h_0 \frac{\partial V}{V} \quad . \qquad \text{(B.15)}$$

Substituting (A.7), we obtain

$$\frac{\partial T}{T} = -2\frac{h_0}{h}\frac{\partial V}{V} \qquad \text{(B.16)}$$

For the electrodes used in my studies, the characteristic height $h_0 \approx 5\mu m$.

This sensitivity equation shows that the sensitivity of elution time to changes in voltage depends very sensitively on the height of the cells in the chamber, and becomes very high as the height approaches zero. In practice, the lowest attainable height is the cell radius. Although the applied voltage from the signal generator is easy to control to high accuracy, it is important to note that the effective voltage in DEP-FFF experiments depends on voltage drops in the circuit and upon electrode polarization, which can change with the condition of the electrode metal during use. Careful monitoring of V and the electrode condition is therefore required when the cells under study travel through the DEP-FFF chamber at small heights.

At larger heights, $h >> h_0$, the sensitivity of the elution time to small changes in voltage is much smaller.

Bibliography

1. Geiger, J.E., C.M. Hickey, and N.S. Magoski, *Ca2+ entry through a non-selective cation channel in Aplysia bag cell neurons.* Neuroscience, 2009. **162**(4): p. 1023-38.
2. Cristofanilli, M., et al., *Circulating tumor cells: a novel prognostic factor for newly diagnosed metastatic breast cancer.* J Clin Oncol, 2005. **23**(7): p. 1420-30.
3. Paterlini-Brechot, P. and N.L. Benali, *Circulating tumor cells (CTC) detection: clinical impact and future directions.* Cancer Lett, 2007. **253**(2): p. 180-204.
4. Pantel, K., R.H. Brakenhoff, and B. Brandt, *Detection, clinical relevance and specific biological properties of disseminating tumour cells.* Nat Rev Cancer, 2008. **8**(5): p. 329-40.
5. Miller, M.C., G.V. Doyle, and L.W. Terstappen, *Significance of Circulating Tumor Cells Detected by the CellSearch System in Patients with Metastatic Breast Colorectal and Prostate Cancer.* J Oncol, 2010. **617421**(10): p. 9.
6. Raimondi, C., et al., *Epithelial-mesenchymal transition and stemness features in circulating tumor cells from breast cancer patients.* Breast Cancer Res Treat, 2011. **130**(2): p. 449-455.
7. Bonnomet, A., et al., *Epithelial-to-mesenchymal transitions and circulating tumor cells.* J Mammary Gland Biol Neoplasia. **15**(2): p. 261-73.
8. Riethdorf, S. and K. Pantel, *Disseminated tumor cells in bone marrow and circulating tumor cells in blood of breast cancer patients: current state of detection and characterization.* Pathobiology, 2008. **75**(2): p. 140-8.
9. Zheng, S. and W. Liu, *Functional gradient ascent for Probit regression.* Pattern Recognition, 2012. **45**(12): p. 4428-4437.
10. Vona, G., et al., *Isolation by size of epithelial tumor cells : a new method for the immunomorphological and molecular characterization of circulatingtumor cells.* Am J Pathol, 2000. **156**(1): p. 57-63.
11. Pohl, H.A., *Dielectrophoresis: the behavior of neutral matter in nonuniform electric fields*. 1978: Cambridge University Press. Cambridge.
12. Becker, F.F., et al., *Separation of human breast cancer cells from blood by differential dielectric affinity.* Proceedings of the National Academy of Sciences of the United States of America, 1995. **92**(3): p. 860-4.
13. Becker, F.F., Huang, H., Pethig, R., Vykoukal, J., Gascoyne, P.R.C., *The removal of human leukaemia cells from blood using interdigitated electrodes.* Journal of Physics D: Applied Physics, 1994. **27**.
14. Moon, H.S., et al., *Continuous separation of breast cancer cells from blood samples using multi-orifice flow fractionation (MOFF) and dielectrophoresis (DEP).* Lab Chip, 2011. **11**(6): p. 1118-25.

15. Wang, L., et al., *Dual frequency dielectrophoresis with interdigitated sidewall electrodes for microfluidic flow-through separation of beads and cells.* Electrophoresis, 2009. **30**(5): p. 782-91.
16. Jones, T.B., *Electromechanics of Particles*. 2005: Cambridge.
17. Wang, X.B., et al., *Separation of polystyrene microbeads using dielectrophoretic/gravitational field-flow-fractionation.* Biophys J, 1998. **74**(5): p. 2689-701.
18. Wang, X.B., et al., *Cell separation by dielectrophoretic field-flow-fractionation.* Anal Chem, 2000. **72**(4): p. 832-9.
19. Gascoyne, P.R., et al., *Isolation of rare cells from cell mixtures by dielectrophoresis.* Electrophoresis, 2009. **30**(8): p. 1388-98.
20. Gascoyne, P.R., et al., *Correlations between the dielectric properties and exterior morphology of cells revealed by dielectrophoretic field-flow fractionation.* Electrophoresis, 2013. **34**(7): p. 1042-50.
21. Reinhold, W.C., et al., *Detailed DNA methylation profiles of the E-cadherin promoter in the NCI-60 cancer cells.* Mol Cancer Ther, 2007. **6**(2): p. 391-403.
22. Shim, S., et al., *Dielectrophoresis has broad applicability to marker-free isolation of tumor cells from blood by microfluidic systems.* Biomicrofluidics, 2013. **7**: p. 011808.
23. Shim, S., et al., *Antibody-independent isolation of circulating tumor cells by continuous-flow dielectrophoresis.* Biomicrofluidics, 2013. **7**: p. 011807.
24. Shim, S., et al., *Dynamic physical properties of dissociated tumor cells revealed by dielectrophoretic field-flow fractionation.* Integrative Biology, 2011. **3**(8): p. 850-862.
25. Gascoyne, P.R., *Dielectrophoretic-field flow fractionation analysis of dielectric, density, and deformability characteristics of cells and particles.* Anal Chem, 2009. **81**(21): p. 8878-85.
26. Reddig, P.J. and R.L. Juliano, *Clinging to life: cell to matrix adhesion and cell survival.* Cancer Metastasis Rev, 2005. **24**(3): p. 425-39.
27. Pohl, H.A. and J.S. Crane, *Dielectrophoretic force.* J Theor Biol, 1972. **37**(1): p. 1-13.
28. Gascoyne, P., et al., *Dielectrophoretic detection of changes in erythrocyte membranes following malarial infection.* Biochim Biophys Acta, 1997. **1323**(2): p. 240-52.
29. Gascoyne, P.R., et al., *Dielectrophoretic Separation of Cancer Cells from Blood.* IEEE Trans Ind Appl, 1997. **33**(3): p. 670-678.
30. Xiao-Bo, W., et al., *Dielectrophoretic manipulation of particles.* Industry Applications, IEEE Transactions on, 1997. **33**(3): p. 660-669.
31. Wang, X.B., et al., *A unified theory of dielectrophoresis and travelling wave dielectrophoresis.* Journal of Physics D: Applied Physics, 1994. **27**(7): p. 1571.
32. Gascoyne, P.R., et al., *Membrane changes accompanying the induced differentiation of Friend murine erythroleukemia cells studied by dielectrophoresis.* Biochim Biophys Acta, 1993. **1149**(1): p. 119-26.

33. Huang, Y., et al., *Membrane dielectric responses of human T-lymphocytes following mitogenic stimulation.* Biochimica et Biophysica Acta, 1999. **1417**(1): p. 51-62.
34. Wang, X., F.F. Becker, and P.R.C. Gascoyne, *The fractal dimension of cell membrane correlates with its capacitance: A new fractal single-shell model.* Chaos: An Interdisciplinary Journal of Nonlinear Science, 2010. **20**(4): p. 043133.
35. Wang, X.B., et al., *Changes in Friend murine erythroleukaemia cell membranes during induced differentiation determined by electrorotation.* Biochimica et Biophysica Acta, 1994. **1193**(2): p. 330-44.
36. Wang, X.-B., et al., *Selective dielectrophoretic confinement of bioparticles in potential energy wells.* Journal of Physics D: Applied Physics, 1993. **26**(8): p. 1278.
37. Markx, G.H., et al., *Dielectrophoretic characterization and separation of micro-organisms.* Microbiology, 1994. **140**(3): p. 585-591.
38. Becker, F.F., et al., *The removal of human leukaemia cells from blood using interdigitated microelectrodes.* Journal of Physics D: Applied Physics, 1994. **27**(12): p. 2659-2662.
39. Markx, G.H. and R. Pethig, *Dielectrophoretic separation of cells: Continuous separation.* Biotechnology and bioengineering, 1995. **45**(4): p. 337-43.
40. Jones, T.B. and G.A. Kallio, *Dielectrophoretic levitation of spheres and shells.* Journal of Electrostatics, 1979. **6**(3): p. 18.
41. Chan, K.L., et al., *Electrorotation of liposomes: verification of dielectric multi-shell model for cells.* Biochim Biophys Acta, 1997. **15**(2): p. 182-96.
42. Green, N.G. and H. Morgan, *Dielectrophoretic separation of nano-particles.* Journal of Physics D: Applied Physics, 1997. **30**(11): p. L41.
43. Wang, X.-B., et al., *Theoretical and experimental investigations of the interdependence of the dielectric, dielectrophoretic and electrorotational behaviour of colloidal particles.* Journal of Physics D: Applied Physics, 1993. **26**(2): p. 312.
44. Jones, T.B., *Basic theory of dielectrophoresis and electrorotation.* IEEE Eng Med Biol Mag, 2003. **22**(6): p. 33-42.
45. Pethig, R. and G.H. Markx, *Applications of dielectrophoresis in biotechnology.* Trends in biotechnology, 1997. **15**(10): p. 426-32.
46. Pethig, R., et al., *Dielectrophoresis: A Review of Applications for Stem Cell Research.* Journal of Biomedicine and Biotechnology, 2010.
47. Piacentini, N., et al., *Separation of platelets from other blood cells in continuous-flow by dielectrophoresis field-flow-fractionation.* Biomicrofluidics, 2011. **5**(3): p. 34122-341228.
48. Borgatti, M., et al., *Separation of white blood cells from erythrocytes on a dielectrophoresis (DEP) based 'Lab-on-a-chip' device.* Int J Mol Med, 2005. **15**(6): p. 913-20.

49. Oeinck, M., et al., *Biomechanical Characterization of Pancreatic Tumor Cells by Dielectrophoresis Force Generation in a Microfluidic System.* Pancreas, 2009. **38**(8): p. 1034-1034.
50. Thomas, R.S., et al., *Trapping single human osteoblast-like cells from a heterogeneous population using a dielectrophoretic microfluidic device.* Biomicrofluidics, 2010. **4**(2): p. 3406951.
51. Salmanzadeh, A., et al., *Isolation of prostate tumor initiating cells (TICs) through their dielectrophoretic signature.* Lab on a Chip, 2012. **12**(1): p. 182-189.
52. Broche, L.M., et al., *Early detection of oral cancer - Is dielectrophoresis the answer?* Oral Oncology, 2007. **43**(2): p. 199-203.
53. Mulhall, H.J., et al., *Cancer, pre-cancer and normal oral cells distinguished by dielectrophoresis.* Analytical and bioanalytical chemistry, 2011. **401**(8): p. 2455-2463.
54. Sabuncu, A.C., et al., *Dielectrophoretic separation of mouse melanoma clones.* Biomicrofluidics, 2010. **4**(2): p. 021101.
55. Yang, F., et al., *Dielectrophoretic separation of colorectal cancer cells.* Biomicrofluidics, 2010. **4**(1): p. 13204.
56. Moon, H.S., et al., *Continuous separation of breast cancer cells from blood samples using multi-orifice flow fractionation (MOFF) and dielectrophoresis (DEP).* Lab on a Chip, 2011. **11**(6): p. 1118-1125.
57. Pratt, E.D., et al., *Rare cell capture in microfluidic devices.* Chemical Engineering Science, 2011. **66**(7): p. 1508-1522.
58. Gascoyne, P.R.C., et al. *Dielectrophoretic separation of cancer cells from blood.* in *Industry Applications Conference, 1995. Thirtieth IAS Annual Meeting, IAS '95., Conference Record of the 1995 IEEE*. 1995.
59. Rousselet, J., G.H. Markx, and R. Pethig, *Separation of erythrocytes and latex beads by dielectrophoretic levitation and hyperlayer field-flow fractionation.* Colloids and Surfaces A: Physicochemical and Engineering Aspects, 1998. **140**(1–3): p. 209-216.
60. Markx, G.H., J. Rousselet, and R. Pethig, *DEP-FFF: Field-Flow Fractionation Using Non-Uniform Electric Fields.* Journal of Liquid Chromatography & Related Technologies, 1997. **20**(16-17): p. 2857-2872.
61. Huang, Y., et al., *Introducing dielectrophoresis as a new force field for field-flow fractionation.* Biophys J, 1997. **73**(2): p. 1118-29.
62. Yang, J., et al., *Cell separation on microfabricated electrodes using dielectrophoretic/gravitational field-flow fractionation.* Anal Chem, 1999. **71**(5): p. 911-8.
63. Huang, Y., et al., *The removal of human breast cancer cells from hematopoietic CD34+ stem cells by dielectrophoretic field-flow-fractionation.* J Hematother Stem Cell Res, 1999. **8**(5): p. 481-90.
64. Gascoyne, P., et al., *Microsample preparation by dielectrophoresis: isolation of malaria.* Lab Chip, 2002. **2**(2): p. 70-5.

65. Vykoukal, D.M., P.R.C. Gascoyne, and J. Vykoukal, *Dielectric characterization of complete mononuclear and polymorphonuclear blood cell subpopulations for label-free discrimination.* Integrative Biology:Quantitative Biosciences from Nano to Macro, 2009. **1**(7): p. 477-84.
66. Yang, J., et al., *Dielectric properties of human leukocyte subpopulations determined by electrorotation as a cell separation criterion.* Biophysical Journal, 1999. **76**(6): p. 3307-14.
67. Huang, Y., et al., *Membrane changes associated with the temperature-sensitive P85gag-mos-dependent transformation of rat kidney cells as determined by dielectrophoresis and electrorotation.* Biochim Biophys Acta, 1996. **1282**(1): p. 76-84.
68. Chianea, T., N.E. Assidjo, and P.J. Cardot, *Sedimentation field-flow-fractionation: emergence of a new cell separation methodology.* Talanta, 2000. **51**(5): p. 835-47.
69. Mirtaheri, P., S. Grimnes, and O.G. Martinsen, *Electrode polarization impedance in weak NaCl aqueous solutions.* IEEE Trans Biomed Eng, 2005. **52**(12): p. 2093-9.
70. Schwan, H.P., *Linear and nonlinear electrode polarization and biological materials.* Ann Biomed Eng, 1992. **20**(3): p. 269-88.
71. Schwan, H.P., *Altenating current electrode polarization.* Biophysik, 1966. **3**(2): p. 181-201.
72. Abkarian, M. and A. Viallat, *Dynamics of vesicles in a wall-bounded shear flow.* Biophysical Journal, 2005. **89**(2): p. 1055-66.
73. Stephen Williams, P., T. Koch, and J. Calvin Giddings, *Characterization of near-wall hydrodynamic lift forces using sedimentation field-flow fractionation.* Chemical Engineering Communications, 1992. **111**(1): p. 121-147.
74. Tong, X. and K.D. Caldwell, *Separation and characterization of red blood cells with different membrane deformability using steric field-flow fractionation.* Journal of chromatography B, Biomedical applications, 1995. **674**(1): p. 39-47.
75. Cardot, P., et al., *Hyphenation of sedimentation field flow fractionation with flow cytometry.* J Chromatogr B Analyt Technol Biomed Life Sci, 2002. **768**(2): p. 285-95.
76. Vykoukal, J., et al., *Enrichment of putative stem cells from adipose tissue using dielectrophoretic field-flow fractionation.* Lab Chip, 2008. **8**(8): p. 1386-93.
77. Grinstein, S. and J.K. Foskett, *Ionic mechanisms of cell volume regulation in leukocytes.* Annu Rev Physiol, 1990. **52**: p. 399-414.
78. Massaldi, H.A., G.V. Richieri, and H.C. Mel, *Alternative interpretation for the osmotic response of human erythrocytes.* J Cell Physiol, 1986. **127**(3): p. 448-50.
79. Mader, M.A., et al., *Dynamics of viscous vesicles in shear flow.* The European physical journal E, Soft matter, 2006. **19**(4): p. 389-97.
80. Abkarian, M., et al., *Cellular-scale hydrodynamics.* Biomed Mater, 2008. **3**(3): p. 1748-6041.

81. Boyum, A., et al., *Separation of leucocytes: improved cell purity by fine adjustments of gradient medium density and osmolality.* Scand J Immunol, 1991. **34**(6): p. 697-712.
82. Rosenberg, R., et al., *Comparison of two density gradient centrifugation systems for the enrichment of disseminated tumor cells in blood.* Cytometry, 2002. **49**(4): p. 150-8.
83. Mego, M., S.A. Mani, and M. Cristofanilli, *Molecular mechanisms of metastasis in breast cancer—clinical applications.* Nature reviews Clinical oncology, 2010. **7**(12): p. 693-701.
84. Mego, M., et al. *Circulating Tumor Cells (CTCs) and Epithelial Mesenchymal Transition (EMT) in Breast Cancer: Describing the Heterogeneity of Microscopic Disease*. in *Cancer Research*. 2009. AMER ASSOC CANCER RESEARCH 615 CHESTNUT ST, 17TH FLOOR, PHILADELPHIA, PA 19106-4404 USA.
85. Wang, X., F.F. Becker, and P.R. Gascoyne, *The fractal dimension of cell membrane correlates with its capacitance: a new fractal single-shell model.* Chaos, 2011. **20**(4): p. 043133.
86. Pethig, R. and D.B. Kell, *The passive electrical properties of biological systems: their significance in physiology, biophysics and biotechnology.* Phys Med Biol, 1987. **32**(8): p. 933-70.
87. Gascoyne, P.R.C., *"Isolation and Characterization of Cells by Dielectrophoretic Field-Flow Fractionation" in Field-Flow Fractionation in Biopolymer Analysis*. Field-Flow Fractionation in Biopolymer Analysis, ed. K.D. Caldwell and S.K.R. Williams. 2012: Springer-Verlag.
88. Tinajero, J.P., et al., *Fractal analysis of lung alveoli during the acute phase vs. repair phase of an adenoviral infection in canines.* Research communications in molecular pathology and pharmacology, 1997. **95**(3): p. 275-85.
89. Allard, W.J., et al., *Tumor cells circulate in the peripheral blood of all major carcinomas but not in healthy subjects or patients with nonmalignant diseases.* Clin Cancer Res, 2004. **10**(20): p. 6897-904.
90. Marrinucci, D., et al., *Cytomorphology of circulating colorectal tumor cells: a small case series.* Journal of oncology, 2010. **2010**.
91. Muralidharan-Chari, V., et al., *Microvesicles: mediators of extracellular communication during cancer progression.* J Cell Sci, 2010. **123**(Pt 10): p. 1603-11.
92. Xiao, L., M. Eto, and M.G. Kazanietz, *ROCK mediates phorbol ester-induced apoptosis in prostate cancer cells via p21Cip1 up-regulation and JNK.* J Biol Chem, 2009. **284**(43): p. 29365-75.
93. Shim, S., et al., *Dielectrophoresis has Broad Applicability to Marker-Free Isolation of Tumor Cells from Blood by Microfluidic Systems.* Biomicrofluidics, 2013. **7**(1): p. Submitted.
94. Wang, X.B., et al., *Separation of polystyrene microbeads using dielectrophoretic/gravitational field-flow-fractionation.* Biophysical Journal, 1998. **74**(5): p. 2689-701.

95. Gascoyne, P.R.C., et al., *Isolation of rare cells from cell mixtures by dielectrophoresis.* Electrophoresis, 2009. **30**(8): p. 1388-98.
96. Huang, Y., et al., *Introducing dielectrophoresis as a new force field for field-flow fractionation.* Biophysical Journal, 1997. **73**(2): p. 1118-29.
97. Markx, G.H., R. Pethig, and J. Rousselet, *The dielectrophoretic levitation of latex beads, with reference to field-flow fractionation.* Journal of Physics D: Applied Physics, 1997. **30**: p. 2470-2477.
98. Huang, Y., et al., *The removal of human breast cancer cells from hematopoietic CD34+ stem cells by dielectrophoretic field-flow-fractionation.* Journal of Hematotherapy & Stem Cell Research, 1999. **8**(5): p. 481-90.
99. Brody, J.P., et al., *Biotechnology at low Reynolds numbers.* Biophysical Journal, 1996. **71**(6): p. 3430-41.
100. Gascoyne, P.R.C. and J. Vykoukal, *Particle separation by dielectrophoresis.* Electrophoresis, 2002. **23**(13): p. 1973-83.
101. Bruus, H., *Theoretical microfluidics*. 2008, Oxford ; New York ; Auckland [etc.]: Oxford University Press. XVI-346 p.
102. Wu, J., et al., *Protective effects of polymer additives on animal cells exposed to rapidly falling liquid films.* Biotechnology progress, 1995. **11**(2): p. 127-32.
103. Wang, X., J. Yang, and P.R. Gascoyne, *Role of peroxide in AC electrical field exposure effects on friend murine erythroleukemia cells during dielectrophoretic manipulations.* Biochimica et Biophysica Acta, 1999. **1426**(1): p. 53-68.
104. Vykoukal, J., et al., *Enrichment of putative stem cells from adipose tissue using dielectrophoretic field-flow fractionation.* Lab on a Chip, 2008. **8**(8): p. 1386-93.
105. Alexandrakis, M.G., et al., *Serum proinflammatory cytokines and its relationship to clinical parameters in lung cancer patients with reactive thrombocytosis.* Respiratory medicine, 2002. **96**(8): p. 553-8.
106. Gupta, V., et al., *ApoStream, a new dielectrophoretic device for antibody independent isolation and recovery of viable cancer cells from blood.* Biomicrofluidics, 2012. **6**: p. 024133.